3D reservoir characterization of paleokarst reservoirs on Loppa High through seismic modelling

By

Muhammad Usman Khurshid

Master of Earth Science

Department of Earth Science

University of Bergen

September 2023

Abstract

The slow dissolution of carbonate rocks produces geological landscape features called karst. As meteoric water percolates into the subsurface through permeable pathways, the encompassing rock can start to dissolve in a process called karstification. Given sufficient time, dissolution of soluble rocks may result in the expansion of the initial pore space and the formation of solutional enlarged fractures, vuggy pore networks, and karst caverns. The newly formed pore space may be partly or completely infilled by a range of sediment and breccias, resulting in heterogeneous facies distribution.

One of the most common oil and gas producing reservoirs in the world are hosted in paleokarst. Paleokarst reservoirs occur at depths ranging from less than 200 m to 8000 m and typically comprise significant hydrocarbon volumes. However, they typically have low recovery factor potentially due to difficulties in resolving and delineating this reservoir type from seismic data, eventually resulting in over-/underestimation of STOOIP. High seismic velocities in carbonate rocks, heterogeneous facies distributions, and the relatively small scale of many paleokarst features often result in paleokarst reservoirs being inherently difficult to resolve and delineate from seismic data.

Seismic modelling can help in understanding the signatures unique for various paleokarsts in the seismic data. Synthetic seismic data can be generated with the help of subsurface reservoir models and estimating an elastic property from well data or deriving an empirical relation for different properties using well data. The seismic response of the carbonates can vary depending upon the pore geometry and volume fraction of different pore infill (i.e., solids, fluids, and gas). An efficient way of modelling can be achieved using Point Spread Functions. The convolution of Point Spread Function with the 2D or 3D reflectivity model can generate more realistic results than the standard 1D Convolution method.

In this study, a new seismic modelling workflow for paleokarst reservoirs will be carried out. A pre-built reservoir model of Loppa High, Southwestern Barents Sea was used as input for seismic modelling. The model comprises the stratigraphic and structural framework of the Loppa High, as well as an analogue of a paleokarst system. The Agios Georgios cave system in Northern Greece was used as analogue for simulating anticipated collapse and infill processes and rendering the post-collapse morphology and facies distribution. was repositioned into the Loppa High area between Orn and Falk formations to model and analyze the seismic response of cave system on seismic data.

Acknowldgments

I would like to thank first and foremost my university supervisor Professor Isabelle Lecomte for her time, guidance, and support in completing this thesis and helping me overall during my master studies. Especially the help and guidance she provided during the Arctic Seismic Exploration course, which was a totally new environment for me. I would also like to thank a lot my co-supervisors Dr. Jan Tveranger and Dr. Bjarte Lønøy from NORCE (Norwegian Research Center AS) for their help with the data and the fruitful discussions we had in the NORCE office. A big thanks to Bjarte for bearing with me for countless changes in models and being there whenever needed.

 I would also like to thank Mr. Israel Polonio and Mr. Niels Rameil from Lundin Norway for having project update meetings. Special thanks to Lundin Norway for funding this master thesis and providing the chance to show my skills in summer project. Also, thanks to Lundin Norway for provided the seismic and well data used in this study. I would also like to thank NORSAR Innovation AS for providing the academic license of SeisRoX software for seismic modelling and Schlumberger for providing academic license for Petrel. Special thanks to the IT department and Leo Zijerveld for setting up Remote desktop setup and providing the support for the software used during the master studies. The completion of this thesis was made possible by the help of all these people.

I would like to thank my course mate and dear friend Waleed Khalid for moral and emotional support and pushing me through during time of need. I would also like to thank my parents for believing in me.

Dedication

I would dedicate my thesis to Allah (SWT) with whose blessings I have completed this thesis. I would also like to dedicate it to my beautiful children Mantasha & Muhammad and my wife Sundas because without their support it would never have happened.

Table of Content

List of Figures

List of Tables

Notations

AI - *Acoustic Impedance*

R(0) - *Normal Incident Reflection Coefficient*

AOI - *Area of Interest*

PT - *Permian Triassic*

Vp - *Compressional Wave Velocity*

Vs - *Shear Wave Velocity*

PIMP - *P Wave Impedance*

ρ - *Density*

λ - *Wavelength*

FT - *Fourier Transform*

I$_{SR}$ - *Illumination Vector*

p$_R$ - *Slowness Vector for Scattered Field*

p$_S$ - *Slowness Vector for Incident Field*

PSF - *Point Spread Function*

PSDM - *Pre-Stack Depth Migration*

PSTM - *Pre-Stack Time Migration*

K$_{SR}$ - *Wavenumber Scatter*

ϕ - *Porosity*

V$_m$ - *Matrix Velocity*

V$_f$ - *Pore Fluid Velocity*

ρ$_m$ - *Matrix Density*

ρ$_f$ - *Pore Fluid Density*

Chapter 1

1. Introduction

1.1. Motivation

It is estimated that ~20% of the Earth´s ice-free continental surface is occupied by karst landscapes (Ford and Williams, 2013). The largest hydrocarbon fields around the world are produced from carbonates (e.g., Middle East, Europe, America, and South-East Asia), many of which are karstified. Karstified carbonate rocks also hold a large amount of ground water but can also be excellent sited for industrial minerals like uranium, aluminum, nickel, vanadium, and phosphates (Mazzullo and Chilingarian, 1996). The discovery of Gotha, Alta, and Neiden on the Loppa High in the Norwegian Barents Sea are likely the paleokarst reservoirs on Norwegian Continental Shelf (NCS) expected to comprise sufficient resource estimates for production.

Carbonate rocks are often soluble and start to dissolve in contact with meteoric water. A surface or subsurface feature developed on or within the soluble rocks, such as limestone, marble and gypsum is termed as karst and the process of dissolution which generates karst is known as karstification (Ford and Williams, 1989). The general term for preserved ancient karts is paleokarst and most commonly these features get filled with stratified sediments (Simms, 2014). The caves, sinkholes, and karst towers (Figure 1.1-1) are the dominant karst features (Ford and Williams, 1989). The carbonate paleokarst reservoirs are adjacent to the paleo-weathering unconformities, with complex spatial distribution and interconnected relationships (Tian et al.,2019). Mostly caves get subjected to high overburden due to burial depth and the cave ceiling collapses resulting in cave channel filled with sediments or collapse material. The infill can be allochthonous and autochthonous sediments, breakdown material from walls/roofs, precipitates from various processes (fluvial, aeolian, gravitational etc.). The caves or sinkholes can still have cavities which are usually encountered while drilling as bit drop (Zeng et al, 2011a). These reservoirs can hold a significantly larger volume of hydrocarbons than conventional clastic reservoirs. High seismic velocity in carbonate rocks, compared to siliciclastic rocks (Janson and Fomel, 2011), typically result in relatively low horizontal and vertical seismic resolution.

Carbonates are often very complex because of the different depositional settings and the later stage changes due to dissolution and diagenesis. The effect of dissolution and diagenesis also lead to generation of pore types with different shape and size. Compared with siliciclastic rocks, which mainly have one pore type, carbonate rocks have a variety of different pore types (Xu and Payne, 2009) & (Lonoy, 2006). The process of karstification can result in solutional widened cracks, caverns, and vuggy porosity. These secondary pore types add to other primary pore types present in the host rock and may result in a complex distribution of a wide range of pore types. Elastic-wave velocity, which is the controlling factor in seismic data, will be highly affected by how large the pores are and the type of fluid present inside the pore. This is the main challenge in the characterization of carbonates.
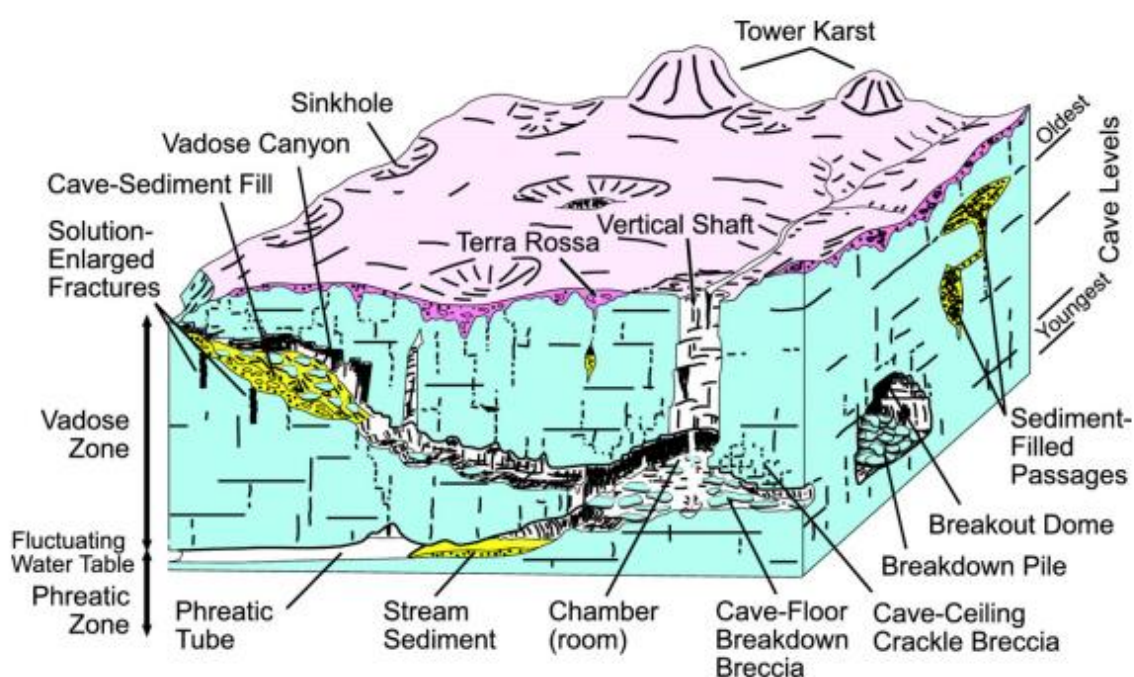
Figure 1.1-1 Karst features that can occur in carbonate Rocks (Zeng et al., 2011a)

The validation of seismic interpretation in paleokarst reservoirs area can be done by comparison with modeled seismic data. To create realistic models of known karst features and then use these models to generate synthetic seismic data. These characteristics of modelled data can then be used to analyze real seismic data to identify similar features. The variation of multiple petrophysical properties like fluid type, water saturation and porosity can be introduced to study the parameter which has the most effect on the seismic behavior.

1.2.   Aim of Study

Significant lateral and vertical variations in paleokarst reservoirs often lead to less reliance on well data; therefore, the mapping of these complex structures is typically based on seismic data. The aim of this thesis is to develop a workflow for seismic modelling of paleokarst reservoirs using geocellular reservoir models from Loppa High as input. The seismic modelling results can be benchmarked against the reservoir model and assist seismic interpreters in potentially identifying seismic signature indicative of paleokarst features. In turn, these signatures could potentially be resolved from real seismic data. In this study, a reservoir model of the Loppa High, that comprise a paleokarst analogue of the Agios Georgios cave system in northern Greece, will be used. Generally, rock physics models are used to define the elastic properties of rock. However, for carbonate rocks, the rock physics models for carbonates are not well defined and erroneous values can be generated. A new approach of estimating velocities and density based on porosity and pore type is used here to generate the input elastic models. The variation of overburden and water saturation will be introduced in the different models to see the change in seismic response. A 3D Point -Spread Function convolution modelling will be used to simulate the seismic.

Chapter 2

2. Geological Settings, Carbonates and Karsts

2.1. Geological Settings

The area of interest lies in the Barents Sea. It is located North of the Norwegian Sea, West of Kara Sea and East of Greenland Sea. The Barents Sea is further divided into tectonic provinces. The stratigraphic succession in the region shows consistent sedimentary packages from Carboniferous to Quaternary. The tectonic activity in Jurassic and afterwards generated most of the structural configuration in the region with uplift playing the most important role. (Nyland et al. 1992). It includes multiple basins, structural highs and fault complexes. Some of the major tectonic provinces of the Barents Sea include Hammerfest Basin, Finnmark Platform, Loppa High, Bjarmeland Platform, Nordkapp Basin, Ringvassøy-Loppa and Bjørnøyrenna fault complexes, the Bjørnøya Basin, the Barents Sea western margin and Stappen High/Bjørnøya (Larssen et al. 2005) (Figure 2.1-).

The area of study is part of the Loppa high which is a structural high in the South-Western part of Barents Sea is Loppa high situated between 71°50'N, 20°E and 71°55'N, 22°40'E and 72°55'N, 24°10'E and 73°20'N, 23°E (Gabrielsen et al. 1990). Loppa high is bounded by Asterias Fault complex in the South, monocline towards Hammerfest Basin and the Bjarmeland Platform in East and South-East, Ringvassøy-Loppa and Bjørnøyrenna Fault Complex to the West and Svalis Dome & Maud Basin in the North-East (Gabrielsen et al. 1990).

The initiation process of Loppa High started with the Caledonian Orogenic event which lasted from Late Cambrian to Early Devonian. The predominant configuration of the basement blocks was controlled by orogeny. The area was subjected to multiple episodes of uplifting and subsidence followed by tilting and erosion (Larssen et al. 2005). The development of Loppa High started with the rifting episode in the mid Carboniferous. Large basins such as Bjørnøya Basin, Tromsø, and Hammerfest basins were created during this period, which also affected the structural high like Loppa High, Stappen High and Veslemøy High (Smelror et al., 2009). Rifting topography was followed by uplifting and tilting of the flank during the late Permian to early Triassic. The low-lying areas were filled with the eroded sediments of Upper Paleozoic and Lower Triassic.
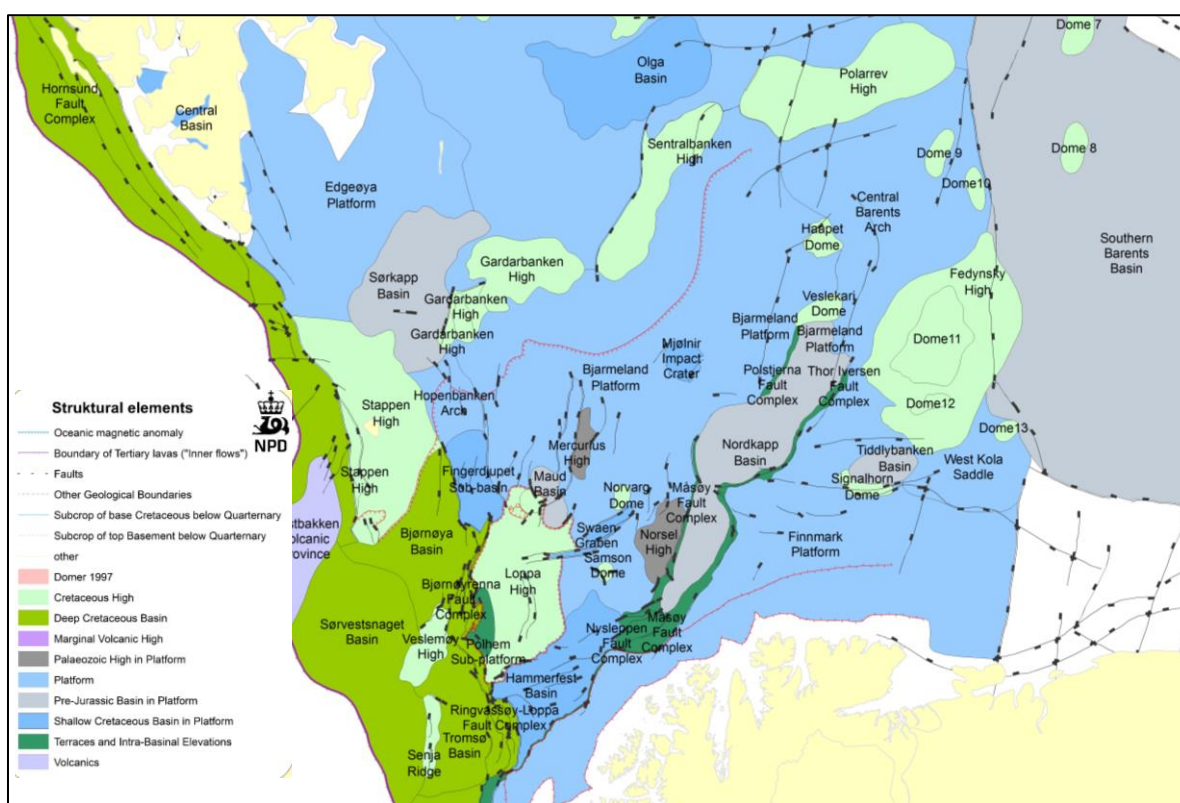
Figure 2.1-1 Structural Elements of the Barents Sea (modified from NPD,2022)

The angular unconformity at the crest of the structure can be identified in the seismic profiles (Figure 2.1-2) which truncates the Upper Paleozoic and Basement strata, overlain by younger sediments of Triassic and Jurassic (Gudlaugsson et al. 1998). The shallow water carbonates were deposited at the Loppa High from mid-Carboniferous until the Late Permian (Stemmerik et al., 1999). Two distinct units of carbonates are identified at the Loppa High which are the Gipsdalen Group of Pennsylvania age and Bjarmeland group of early Permian age (Figure 2.1-3). The environment of deposition for the Gipsdalen group is marine carbonate-ramp. The base of this group is characterized by transgressive clastic, siliciclastic sediments and carbonates, whereas stacked build-ups of warm water carbonates are present at the top (Carrillat et al., 2005). The presence of evaporites in the area indicates that the deposition took place in arid to semi-arid conditions. The presence of stacked shelf deposits which are often truncated by sub-aerial exposure, suggests that high amplitude and high frequency relative sea level fluctuations were the controlling factor of sedimentation (Stemmerik and Worsley, 1989; Stemmerik et al., 1998; Worsley et al., 2001).
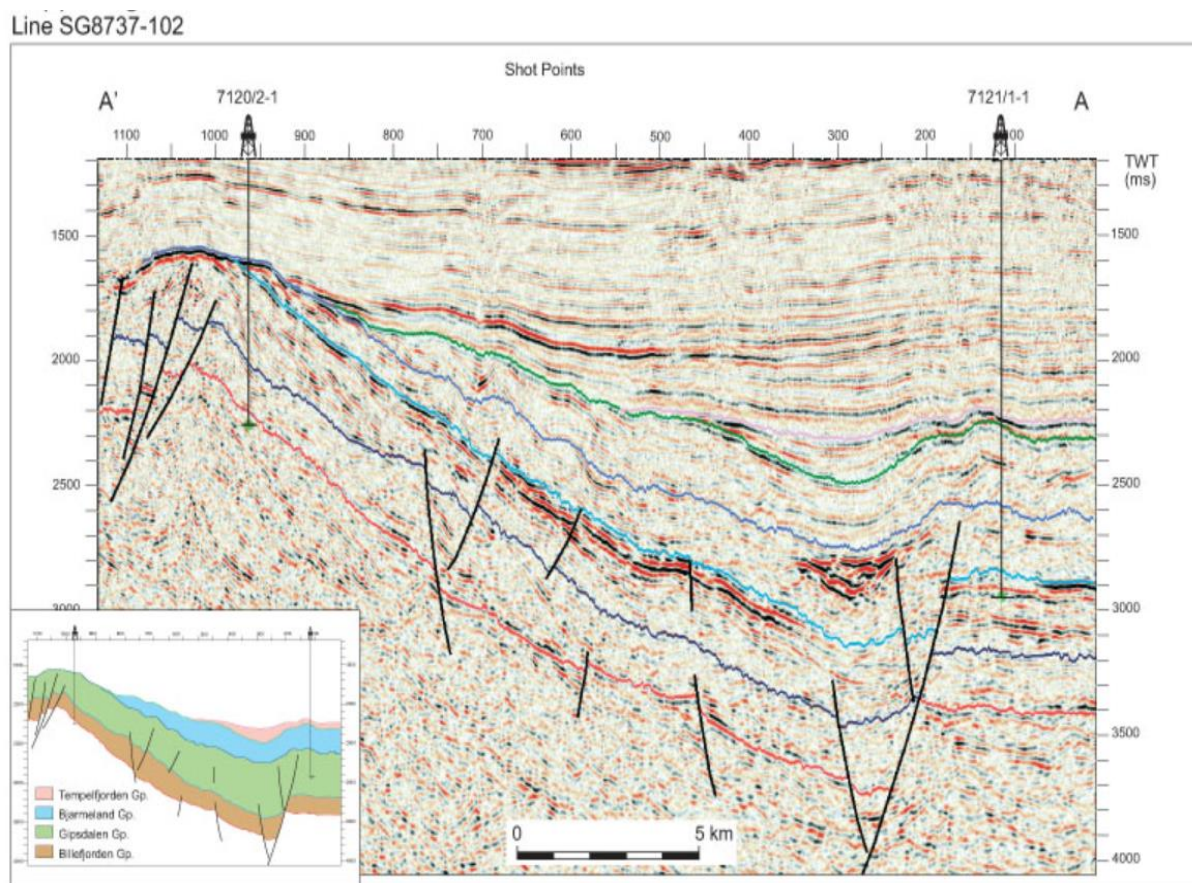
Figure 2.1-2 Seismic line SG8737-102 Loppa High from its crest eastwards towards the Bjarmeland Platform (Larssen et al., 2002)

The deposition of the Bjarmeland group took place in steepened open marine carbonate ramp environment during the early Permian (late Sakmarian to the Artinskian) (Larssen et al., 2002). The carbonate of this group is characterized by cool temperate water condition, dominated by bryozoan build-ups (Blendinger et al., 1997). The mapped horizons of the Falk and Ørn formation dip towards east and are truncated by angular unconformity in the west. A significant column of 350-m to 500-m strata was eroded due to sub-aerial exposure at the crestal location and later the process of karstification changed the carbonate units (Stemmerik et al., 1999; Elvebakk et al., 2003)

6
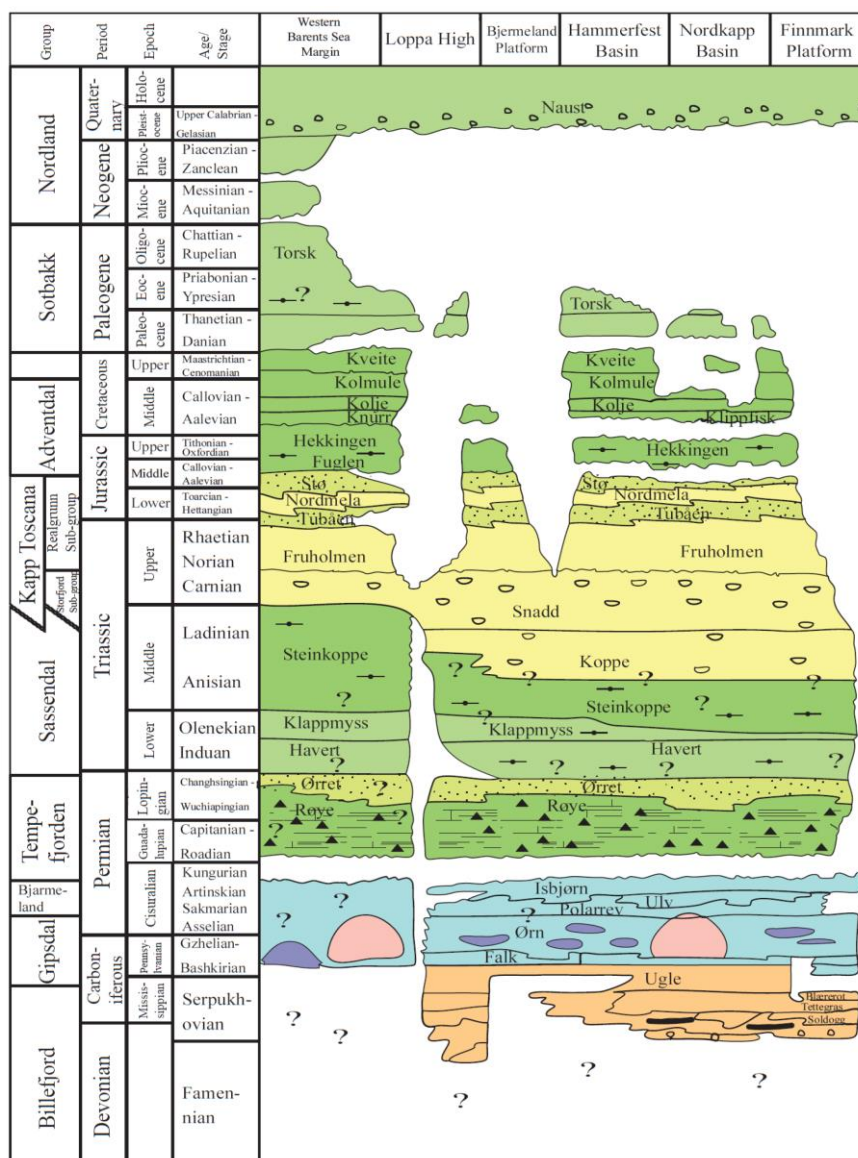
Figure 2.1-3 Lithostratigraphic Chart of the Barents Sea (Courtesy of NPD)

2.2. Carbonate Rocks

The most common sedimentary rock types on earth are either clastic or carbonate rocks. Carbonate rocks are a type of rock that are primarily composed of carbonate minerals, such as calcite (CaCO3) and dolomite (CaMg(CO3)2) which are most common and widely spread on Earth (Figure 2.2-). Some of the more rare minerals which can only be found as small deposits or lenses include magnesite (MgCO3), ankerite (Fe, Ca(CO3) 2), Siderite (FeCO3), strontianite (SrCO3) and others. These rocks form through a variety of processes, including biogenic, chemical, and evaporation. Carbonate rocks are commonly found in marine environments and are often associated with shallow, warm seas but can also be found in lacustrine environments. Examples of carbonate rocks include limestone (primarily composed

of calcite) and dolostone (primarily composed of dolomite). They are widely used in construction, agriculture, and chemical industry.

Figure 2.2-1. Limestone with Shell Fragments (Fossen, 2008)

2.2.1. Depositional Settings

Carbonates can form through a variety of processes, including biogenic, chemical, and evaporation. Carbonate rocks are commonly found in marine environments and are often associated with shallow, warm seas. Carbonate rocks such as limestone and chalk can form in these settings through the accumulation of shells and other biogenic debris. These rocks are commonly found in shallow marine environments, such as shelves and platforms, and are often associated with coral reefs and other biogenic structures (Dunham, 1962). The highest production of carbonates take place in clear tropical waters, where organisms have an abundant population (Moore, 2001)

Carbonate rocks can also form through the precipitation of minerals from evaporating bodies of water, such as lagoons or playas. These rocks are commonly found in tropical arid environments and are often associated with ancient marine and lacustrine basins (Froelich & Murray, 1978). Cold waters can also produce carbonates, where mollusks, bryozoan, foraminifers and barnacles support the carbonate production, but also through the settling of pelagic particles. The depth where the rate of dissolution of CaCO3 equals the supply of CaCO3 which is between 3500-5500 m is known as CCD (Boggs, 2006), above this depth carbonate can be preserved whereas below it is dissolved (Coe, 2003)

Different depositional environments will lead to different depositional facies of carbonates. The position and process of formation of carbonate will also influence the porosity, and permeability of the rock and will also dictate the potential of a reservoir (Wilson, 1975).

2.2.2. Diagenesis

The post-depositional changes in any rock due to the depth of burial and other chemical changes like dissolution and cementation are known as diagenesis. It is a common understanding that diagenesis decreases the porosity in clastic reservoirs, but it is not necessarily the case in carbonates. Deep burial of carbonates decreases the porosity by the process of compaction and cementation whereas enhances the porosity, through dissolution, either by increasing the pore size of existing pores or by generation of new pores. Such changes are associated with the depth of burial, temperature, or hydrologic history of the basin (Mazzullo and Harris, 1991).

2.2.3. Porosity

A carbonate rock can be made up of different shapes and sizes of grains, which depends upon the locality of the deposited grains. This amalgamation of different grains can generate different types of pores within a carbonate rock. The diagenetic changes will further modify the pore types. In carbonates, porosity can be characterized as primary or secondary. The porosity which forms at the time of deposition is termed as primary porosity whereas the porosity which develops after the deposition period is known as secondary porosity (Moore-2001). The preservation of primary pores depends upon the prevailing conditions. The majority of pores in carbonate rocks are secondary in nature (Choquette and Pray, 1970).

A particularly descriptive scheme of different pore types in carbonates was provided by Choquette and Pray (1970) (Figure 2.2.3-1). This was further enhanced by Lønøy (2006) by developing the classification based on pore size instead of grain size. The major types of porosity are:

Interparticle or intercrystalline porosity

The pore spaces that lie between particles are called interparticle porosity whereas the pores between the crystals are termed intercrystalline porosity. This type of porosity is usually associated with secondary porosity.

Intraparticle and intracrystalline porosity

The porosity within grains and crystals is referred to as intraparticle and intracrystalline porosity. These forms of porosity are exclusive to carbonate rocks and are not present in siliciclastic rocks (Moore, 2001). The presence of this type of porosity can either result from primary porosity, which occurs due to small open chambers within the carbonate material, or from the breakdown of organic material in carbonate skeletons (Lønøy, 2006).

Moldic porosity

The formation of moldic porosity is a result of the selective dissolving and recrystallizing of carbonate components and is considered a secondary form of porosity (Lønøy, 2006).

Vuggy porosity

Vuggy pores are characterized by their large size and the fact that they do not conform to the fabric of the rock. They are created by expanding fabric-selective pores, which lack connectivity, through dissolution, such as in the case of moldic pores (Lønøy, 2006).

Channel porosity

The dissolution along the fracture generates channel porosity and is of secondary origin.

Cavernous porosity

The enhancement of channels or vuggy pores to significantly bigger size is termed as cavernous porosity.

Framework and fenestral porosity

The framework porosity is a primary type of porosity, formed through the accumulation of frame-building organisms such as corals, coralline algae, or sponges in reef environments (Moore, 2001). On the other hand, fenestral porosity is characterized by its larger openings compared to inter-grain openings and is a secondary form of porosity. This type of porosity is created by the breakdown of sediment-covered algal mats.

Fracture Porosity

The brittle nature of carbonates makes them fracture due to excessive overburden. The fractures increase the porosity and are of secondary nature.
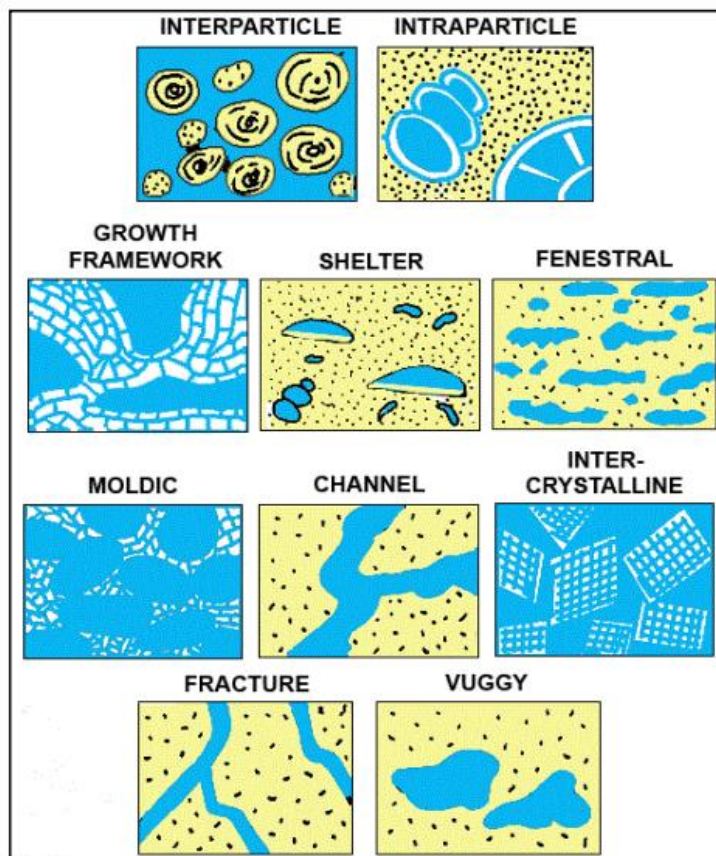
Figure 2.2.3-1 Classification of porosity types in carbonate rocks (Choquette and Pray, 1970)

2.3. Karst and paleokarsts

Karst is defined as '*a special type of landscape feature containing caves and extensive underground water systems that are formed in soluble rocks*' (Ford and William, 2013), whereas paleokarsts are the karsts features that are no longer undergoing active karstification (Lockus-1999). Karst represents a landscape consisting of complex geological features and specific hydrogeological characteristics which are generally formed in carbonate rocks and are highly heterogeneous (Figure 2.3-1). The development of karst starts with the dissolution of carbonate rocks either by meteoric water, mixing of fresh- and salt water (i.e., along the freshwater lens) or by ascending hypogenic waters from deep seated source.
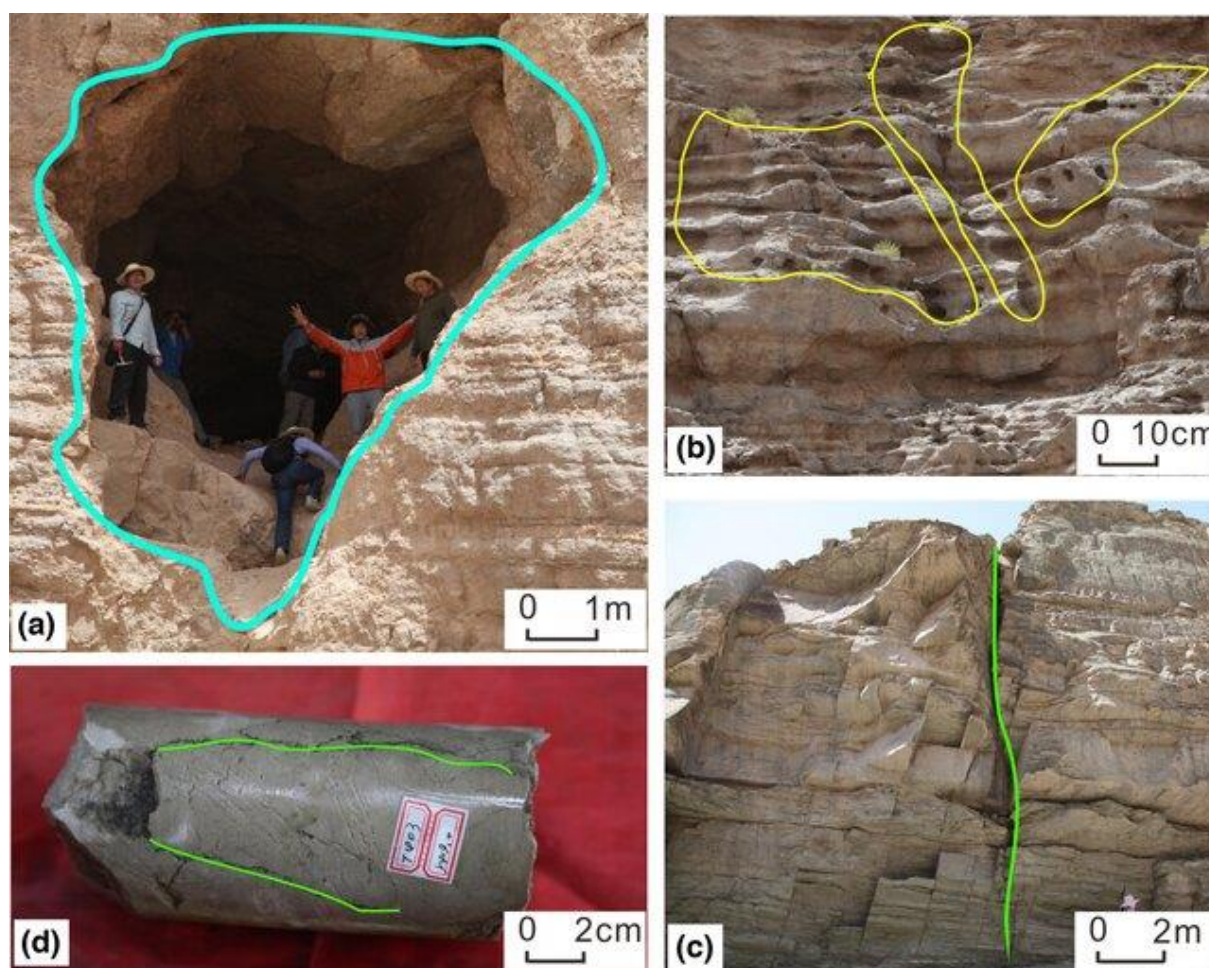
Figure 2.3-1 Different paleokarst types of reservoirs in Tahe Oilfield. a). A large karst cave on the outcrop of Tabei, height >10 m. b) Small-scale dissolved, height in cm's, c) Large-scale fracture with length >20 & width > 15mm, d- Small fractures on the core are 8 to 16 mm (Lyu et al.-2023)

Karsts can be divided into two main types: epigene and hypogene Karts (Lockus-1999). Epigene karsts are generated by the dissolution of the carbonate rock by surface water (meteoric water) which is enriched with CO2. Epigene karsts are formed in coastal marine environments and produce flank margin caves (Mylroie and Carew, 1990) whereas hypogene karsts are generated by the dissolution of carbonates by chemically enriched subsurface water.

Epigene karsts can be classified into different zones based on the water saturation in the caves and faults. The upper part of the epigene profile is called vadose zone and it consists majorly of the drained or partially saturated conduits, caves, and fissures. The deeper part is known as phreatic, and it contains fully saturated conduits. Vadose zone can further be divided into upper and lower vadose zone (Lonoy et al., 2020). The upper vadose zone consists of the roots and soil system and is also termed as epikarst (Figure 2.3-2). Generally, meteoric water is active and abundant in this zone which leads to either dissolution or precipitation. The

epikarst can exist just below the soil forming vertical to sub-vertical shafts that can be filled with silt, clay, or sand. (Esteban and Klappa, 1983). The water movement in the lower vadose zone is through already formed vertical to sub-vertical shafts. Horizontal passages can also be present in this part which would be remains of older phreatic tubes. Dissolution is generally low, and conduits have high sedimentation or collapse material. The sediments fill in both upper and lower vadose show red color indicating oxidizing conditions (Esteban and Klappa, 1983).
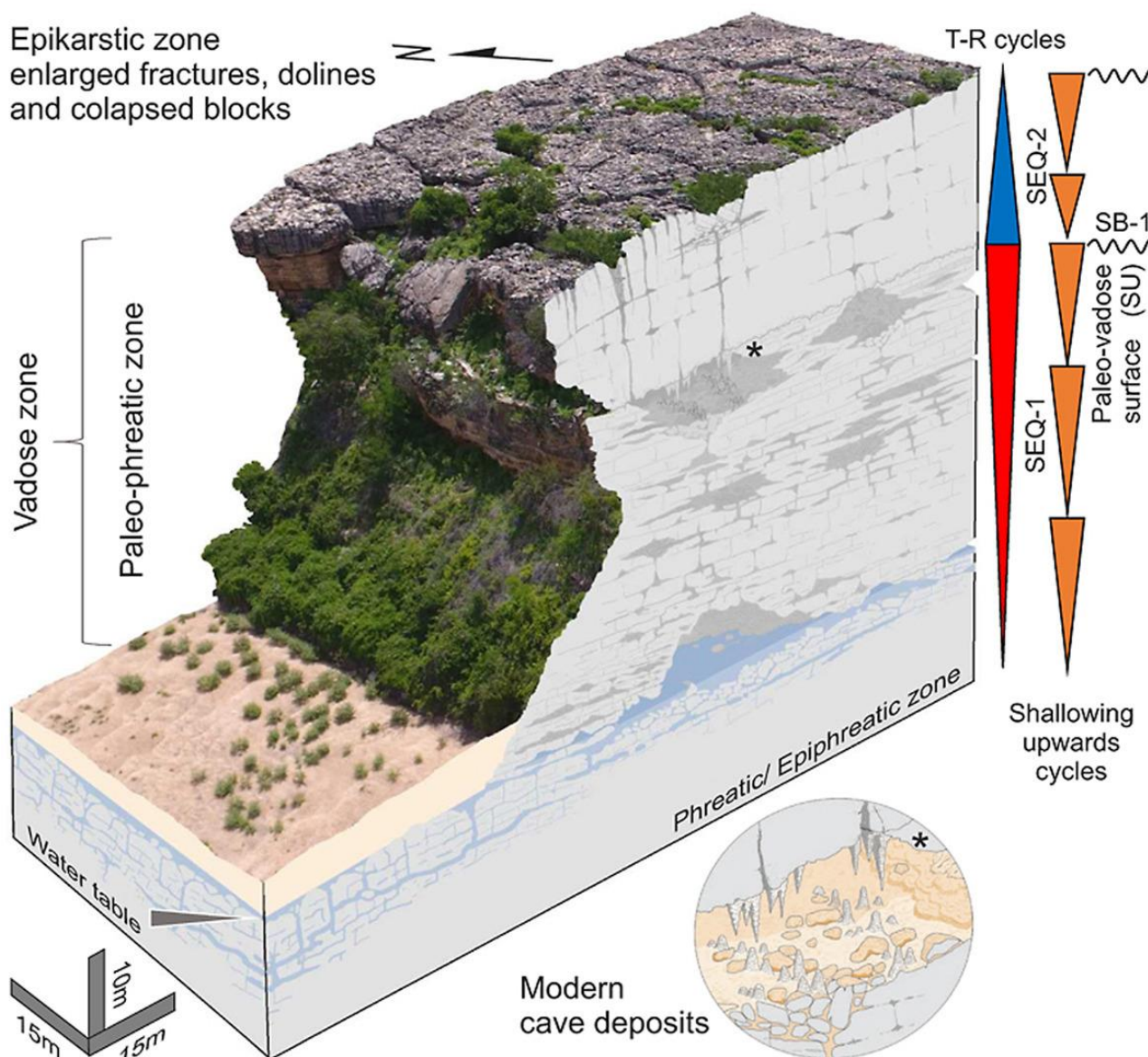
Figure 2.3-2 The profile of epigene karst cave system (Fabio et. al.-2022)

The phreatic zone is defined dominantly by the horizontal to sub-horizontal cave passages (Figure 2.3-2). The dissolution takes place at the water table or below which leads to the generation of cavern porosity. The mixing of marine and fresh-water, hot or cold water, and

pressure differential causes the dissolution process (Esteban and Klappa, 1983). The phreatic tubes can form up to several hundred of meters below the surface and at or below water table which is based on density, dip of the strata and fracture orientation (Lockus, 1999).

The permeability of the karst rocks is enhanced either by the enlargement of ambient pore networks or by water seeping through the faults and fractures expanding these and creating cavities and caves networks. Once the aperture expands above a certain threshold (typically > 5-11 mm diameter) the flow goes from laminar to turbulent, resulting in a rapid expansion of the conduits. Once the conduit diameter surpasses the grain size of unconsolidated clastic sediments, various processes (e.g., fluvial, aeolian, glacial, etc) can transport the sediments (Lockus, 1999).

2.3.1. Cave Collapse and Controlling Factors

Karst systems form over thousands of years by the slow dissolution or solubility by aggressive fluids. The cave systems can have lengths of several kilometers and diameters up to hundreds of meters. The development of the cave is based on many controlling factors which influence the shape and size of the cave. The most common features of karsts are dolines (sinkholes), karst towers, breccia pipes, karrens, and disappearing streams. Some of the major controlling factors in the development of caves are water table position and thickness, climate, duration of exposure, and tectonic settings. Precipitation plays a critical role in the intensity of dissolution. If the precipitation rate is higher than the evaporation rate then it is significantly increased dissolution (Mylroie and Carew, 1995; Ford and Williams, 2013). The position of the water table decides the area where karstification will take place and the size of the area which will be subjected to karstification. The change in sea level will affect the water table configuration and when and where the exposure will take place changing the shape of the cave (Mylroie and Carew, 1995). The exposure duration affects the porosity and permeability of the cave.

The paleokarsts are subjected to increase overburden and stress with time as the depth of burial increases. This leads to diagenetic changes in the karst system as the caves start to collapse. The collapse depth is dependent on the mechanical strength of the rock and the thickness of the overlying stratigraphic column (Ford and William 2013; Lockus 1999). With increasing burial depth, a stress dome is generated above the cave, leading to maximum stress. After a critical point, the cave walls and ceiling will collapse due to mechanical rupturing. If

two caves intersect due to continuous dissolution, it will further lead to caves collapse. This also increases the porosity and permeability of the reservoir (Ford and William 2013; Lockus 1999). The breakdown material of the ceiling will accumulate inside the cave. The cave collapse will continue until the whole cave is filled with sediments (Figure 2.3.1-1). If there is a continuous process of sediment removal from the cave due to the subsurface stream, then a breccia pipe will be generated (Ford and William 2013). If the cave is exposed to floodwater, the rise and fall of sea level will affect the cave system as the cave will then be drained and filled with water several times, which will flex the ceiling leading to higher dissolution and sediment collapse (White and White, 1969).
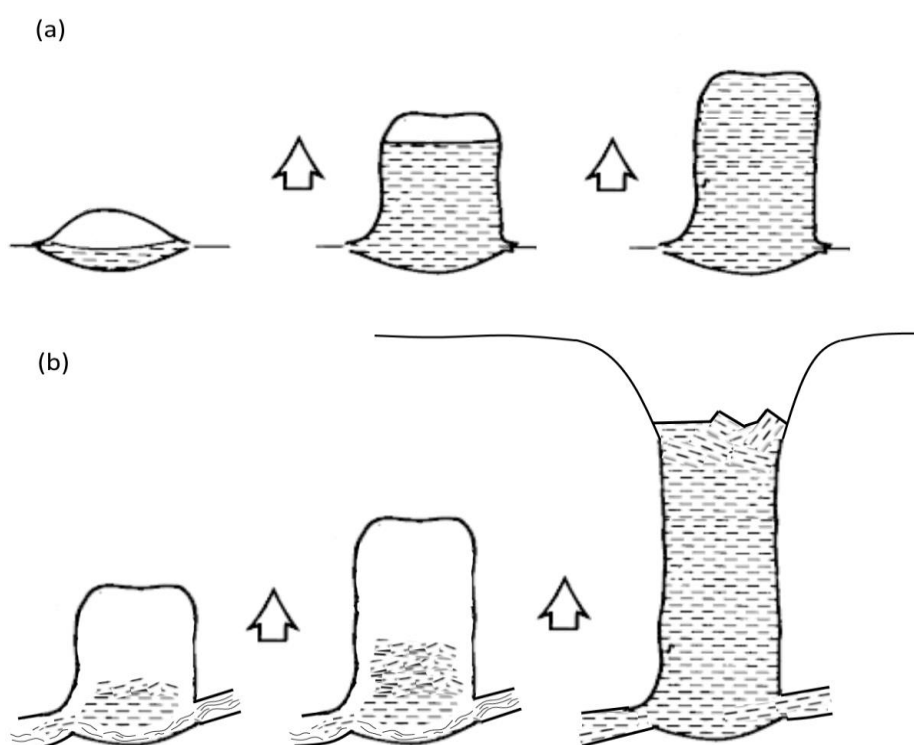
Figure 2.3.1-1 Idealized model for cave development a) No removal of sediments b) Removal of sediments by stream leading to the cave collapse up to surface (James and Choquette 1988)

The breakdown material inside the cave can consist of different facies. Some of the most common are chaotically distributed and oriented breccias of multiple sizes, cave ceiling and cave wall crackle breccias, and a combination of chaotic and crackle breccias called mosaic breccias (Lockus-1999). The sediments carried by the flowing water outside of the cave system can be part of the facies existing inside the paleokarst cave (White and White, 1969). It is difficult to identify a complete sequence inside a paleo cave because the sediments can deposit inside the cave at multiple stages and can have different facies (Lockus, 1999).

As the paleokarst gets buried at higher depths, the mechanical compaction takes effect and further degradation of the facies takes place. More collapse material accumulates inside the cave and the existing breccias are re-brecciated leading to closely packed facies (Lockus,1999). Due to close packing coarse inter breccia porosity decreases and fine inter breccia pores and fracture appears with increasing mechanical compaction (Figure 2.3.1-2). Porosity will also decrease if the pressure solution among grain contact takes place at very high depths (Lockus, 1999).
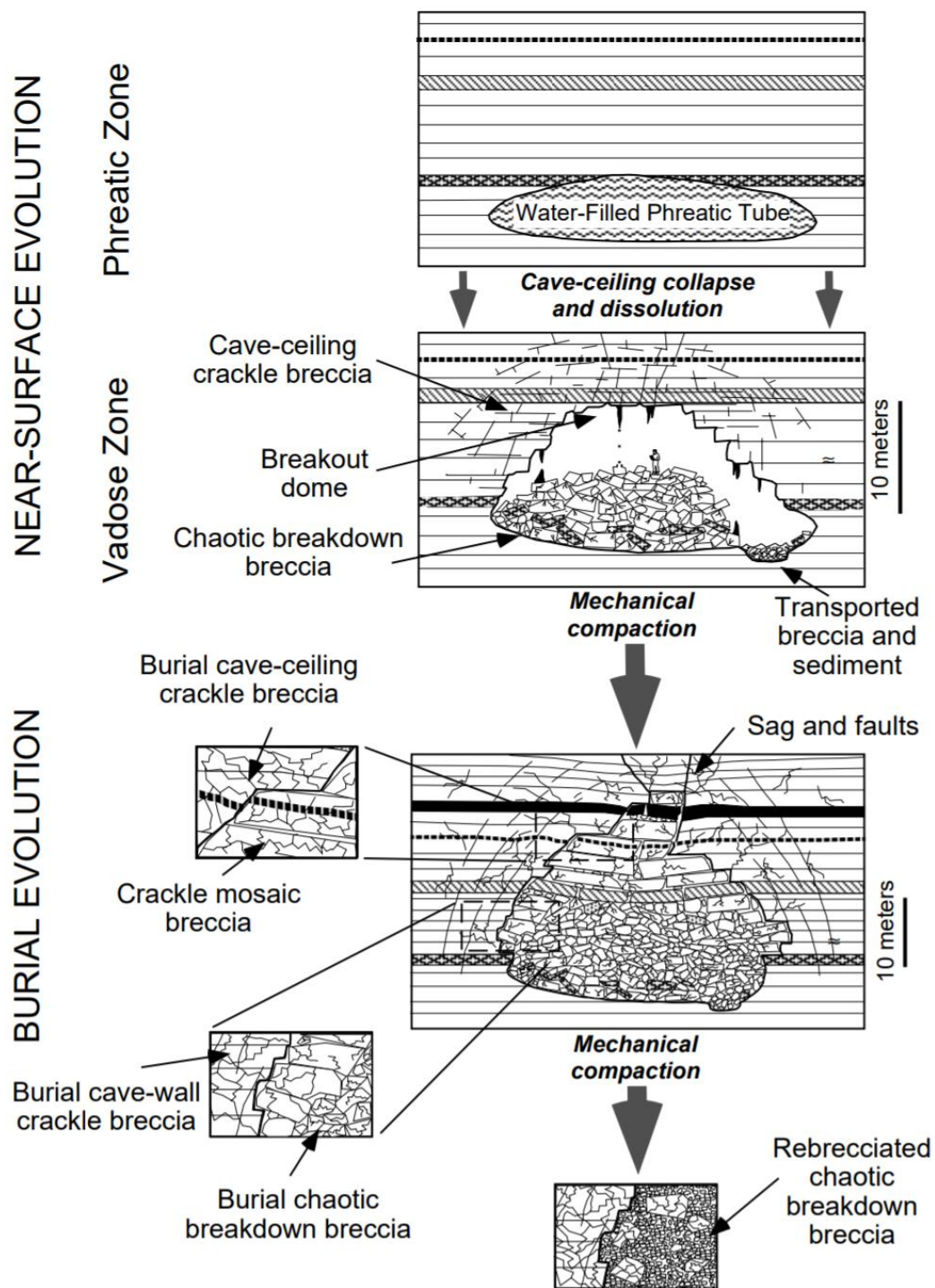
Figure 2.3.1-2 An example of development of phreatic tube from near surface where collapse takes place at higher depths where re-brecciation take place due to mechanical compaction leading to decreased porosity (Lockus,1999).

2.3.2. Paleokarst Reservoirs

Paleokarst reservoirs are one of the most common reservoirs in carbonates and can hold large amounts of hydrocarbon volumes. The presence of paleokarst reservoir has been seen all around the world e.g., Thamama Field in the Middle East (Melville et al., 2004), the Yates Field in West Texas (White and White, 1995), the Casablanca Field in Spain (Lomando et al., 1993), the Kashagan Field in Kazakhstan (Kaiser and Pulsipher, 2007); the Kirkuk Field in Iraq (Trice, 2005), the Tarim basin in China (Zeng et al., 2011a) and Loppa high in the Barents Sea (Sayago et al., 2012). Although the existence of these reservoirs is widely common, characterizing them is very difficult because of their heterogeneous nature.

The varying condition of the deposition of the carbonates along with the chance of the cave being filled with sediments or not, make facies prediction and forecast of production behavior of the reservoir difficult. Some of the common problems linked with these reservoirs are unpredictable water breakthrough, irregular sweep and heterogeneous reservoir pressure (Agar and Hampson, 2014). Another major problem linked with paleo karst reservoirs is the determination of the original oil or gas in-place volumes. The volume calculation is highly dependent on the cave geometry, morphology, and recovery factor (Montaron et al., 2014). The mean recovery factor for oil-saturated horizontal caves is considered to be 48% and it is very sensitive to the slope of the karst cave. The change in the karst slope can increase or decrease the recovery factor by huge margin (Montaron et al., 2014). Due to these reasons, paleokarst reservoirs are considered to be high-risk plays.

The detection of paleokarst features during drilling can help in identifying and quantifying the system. Commonly, paleokarsts are detected while drilling as bit drops. The bit drop can range from a few meters to tens of meters (Loucks, 1999). Therefore, the key to the successful development of such reservoirs is by better understanding of local pore type to regional facies, which will lead to better interpretation and forecasting of the reservoir behavior (Sayago et al., 2012).

Chapter 3

3. Geophysical Understanding for Seismic Modelling

Paleokarst reservoirs are very complex and imaging properly these features on seismic data is very challenging. The changes in the karst shape and cave geometry can change the behaviours of the seismic data. The pore size and shape can have significant differences over very small distances and usually, there is no consistent relationship between porosity and permeability (Ringrose and Bentley,2015). Along with this, the resolution of seismic data is also a critical factor as in carbonates, one has often the highest possible frequency of seismic e.g., up to 40-60 Hz. But the velocity is high too and this decreases the resolution of seismic data.

The carbonate rocks exhibit very high seismic velocities due to their brittle nature for example Zheng et al., (2011b) note limestone host rock velocities of 6000 m/s. The velocities are also very sensitive to the pore shape, size, and pore saturation (Xu and Payne, 2009). Due to high velocities, the extrinsic attenuation increases, and high frequencies cannot penetrate to higher depths, and this leads to poor resolution of the seismic data. Acoustic impedance is the product of seismic velocity and density; contrasts (rapid variations) in acoustic impedance yield reflectivity, thus seismic reflections. If the contrast is high between two layers, seismic amplitudes will be higher and vice versa. However, the impedance contrast between two carbonate layers will often be small, hence weak reflectors yielding low amplitudes on seismic (Decker et al., 2015).

3.1. Key Features for Identification of Paleokarsts on Seismic Data

Paleokarst zones can be identified on seismic data by locating the paleo topographic highs and expression of subaerial exposure such as onlapping of sediments on structural highs and chaotic seismic events (Fontaine et al., 1987). The structural lows on paleo topographic map can be indicative of sinkholes and these can be diagnostic of karst towers and residual hills (Lockus, 1999)

Seismic mapping of an unconformity surface can reveal sinkholes, karst towers, and fluvio-karst features like channels, canyons, and valleys (Zheng et al., 2011b). Sinkholes can be identified on seismic data as circular features (Ahlborn et al., 2014). Breccia pipes can be seen as disruptive zones with chaotic reflection pattern vertically and a cylindrical or conical view in

the horizontal section (Cartwright et al., 2007; Sun et al., 2013). Isopach maps can also help in locating paleo cave systems and circular faults (Lockus, 1999; Zheng et al., 2011b). The presence of bright spots and anomalous amplitudes can be linked with paleokarsts (Figure 3.1-1), whereas the relief map with vertical exaggeration can also help in locating different features (Figure 3.1-2). Minor faults and chaotic reflections pattern can divide the bright spots (Zheng et al., 2011b). Localized sag features can also be indicative of paleokarst reflections.
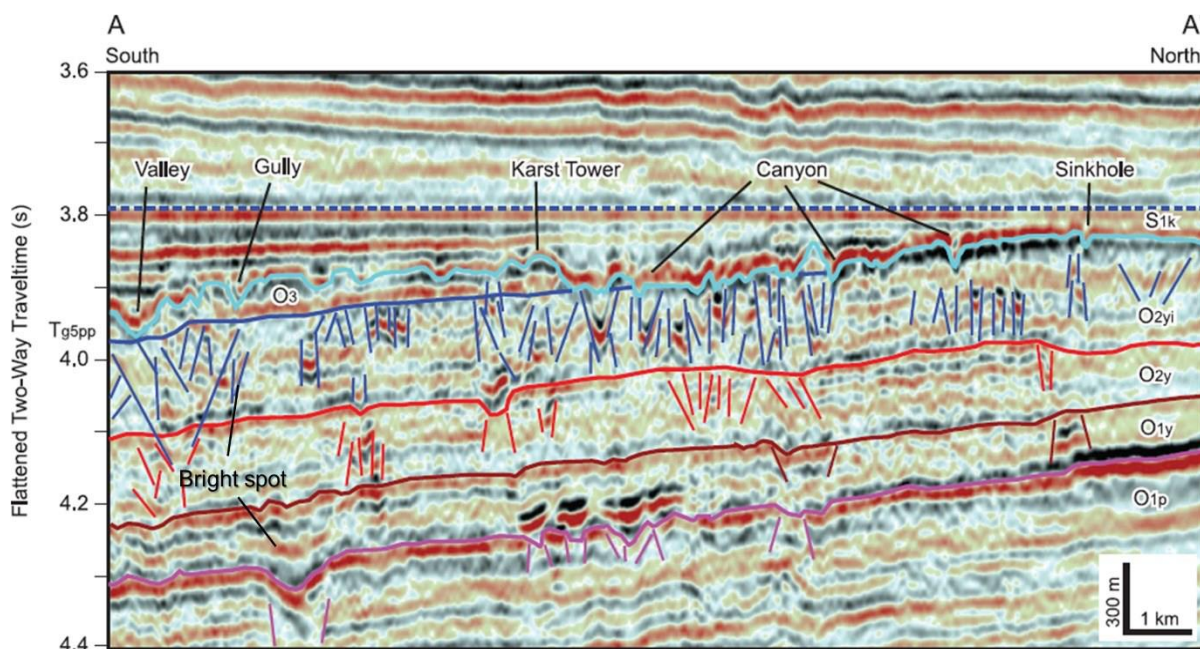
Figure 3.1-1 Seismic Section flattened on Silurian reflector to show the paleo-topography of the Ordovician unconformity in Tarim Basin, China (Zheng et. al,. 2011b)
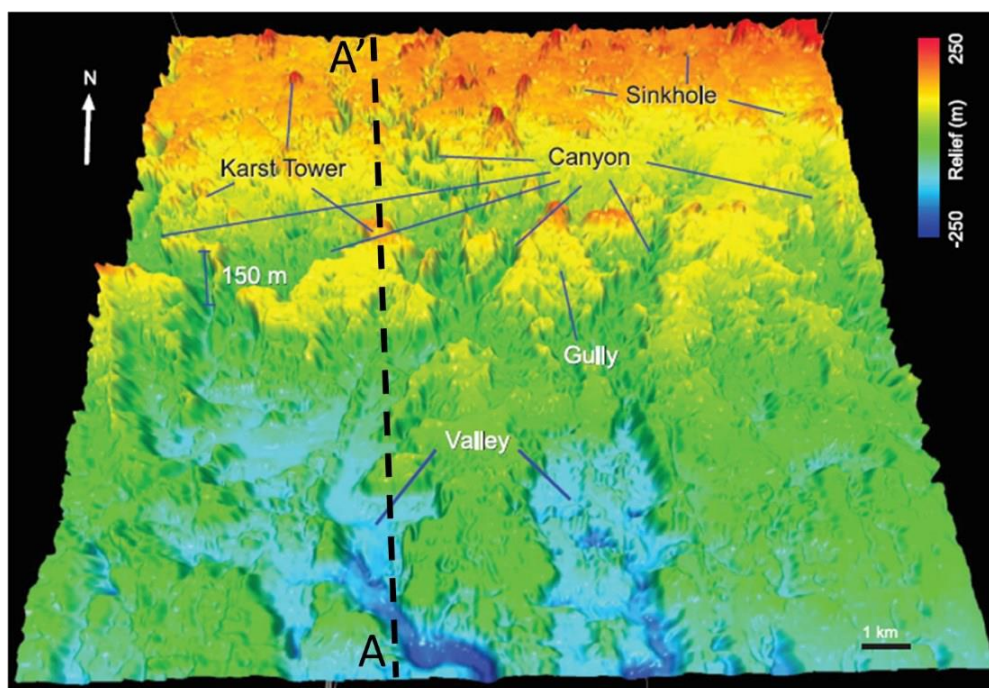
Figure 3.1-2 Relief map of Ordovician unconformity surfaces (Zheng et. al., 2011b)

20

3.2. Seismic Velocities

The 'sound' waves (elastic waves) generated by a seismic source propagates through the subsurface with a velocity known as seismic velocity. During the propagation, multiple waves are produced but the most important for seismic data are compressional (P-wave) and shear Wave (S-wave). P-waves corresponds to a particle movement along the direction of the wave propagation (compression and dilation), while S-waves have a particle movement perpendicular to that movement (Kearey et al., 2013) (Figure 3.2-1).

The compressional nature of P-waves allows it to pass through all materials, whereas shear waves only pass through solids because liquids do not stand any shear. The difference between these waves can be sometimes indicative of hydrocarbons. The velocity of P-waves and S-waves are given, respectively, by.

$$Vp = \sqrt{\frac{K+\frac{4}{3}\mu}{\rho}} \qquad (3.1)$$

$$Vs = \sqrt{\frac{\mu}{\rho}} \qquad (3.2)$$

where K is the bulk modulus, μ is the shear modulus and ρ is the density. These equations indicate that the P-waves will always be faster than S-waves, K and μ being positive values in rock material.
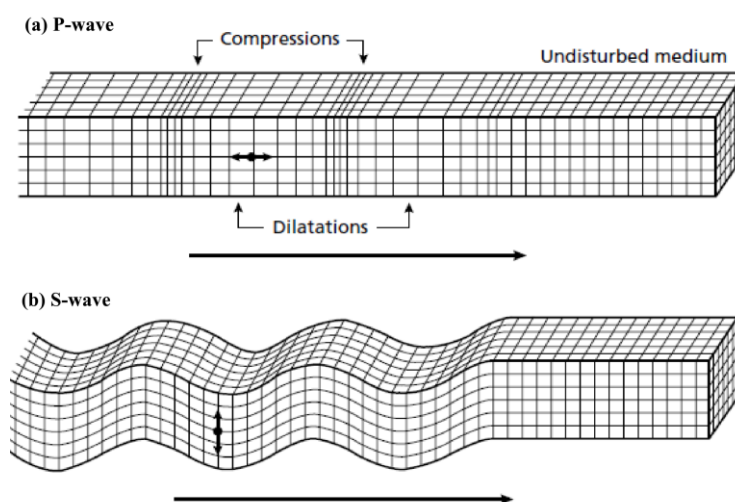
Figure 3.2-1 Particle movement in the elastic medium for a) compressional waves (P) b) shear waves (S) (Kearey et al., 2013)

3.3. Seismic Reflection

Seismic data result from reflection and diffraction of elastic waves within the subsurface. When an elastic wave (P- or S-wave) passes through two layers having different elastic-impedance properties, it splits into up-to four different waves, two as reflected waves and two as transmitted ones (Kearey et al., 2013). The reflected energy will propagate towards the surface and will be recorded at the surface geophones, whereas the transmitted (refracted) energy will further propagate downwards, until reaching a new impedance contrast where a similar splitting will take place (Figure 3.3-1). The partition of energy depends on the incident angle θ_1 and the contrast in impedance. This is expressed by a reflectivity coefficient function of the incident angle. For $\theta_1 = 0$, the normal incident reflectivity Ro is given by:

$$Ro = \frac{AI_2 - AI_1}{AI_1 + AI_2} \quad , \tag{3.3}$$

Where AI_1 is the acoustic impedance of layer 1 (incidence side) and AI_2 is the acoustic impedance of layer 2 (reflection side). The higher the impedance contrast, the higher the amplitude of the reflectivity and less energy will be transmitted or refracted (Kearey et al., 2013). The exact equations for non-zero incidence reflection coefficient are more complex, as driven by Zoeprittz (1919), but approximations exist such as below (Aki and Richards, 1980 Eq 3.4, and Shuey, 1985 Eq. 3.5).

$$R_{pp}(\theta) \approx \frac{1}{2}(1 - 4\rho^2 V_S^2)\left(\frac{\Delta\rho}{\rho}\right) + \frac{1}{2\,Cos^2(\theta)} \cdot \frac{\Delta V_P}{V_P} - 4V_S^2\,\rho^2\frac{\Delta V_S}{V_S} \quad , \tag{3.4}$$

where $\Delta\rho = \rho_{2} - \rho_{1}$, $\Delta V_P = V_{P2} - V_{P1}$, $\Delta V_S = V_{S2} - V_{S1}$, $\rho = (\rho_2 + \rho_1)/2$,

$V_P = (V_{P2} + V_{P1})/2$, $V_S = (V_{S2} + V_{S1})/2$, and $\theta = (\theta_2 + \theta_1)/2$.

$$Rpp(\theta1) \approx Rp + \left(A_o Rp + \frac{\Delta\sigma}{(1-\sigma)^2}\right)sin^2\theta1 + \frac{1}{2}\frac{\Delta Vp}{Vpa}(tan^2\theta1 - sin^2\theta1) \;, \tag{3.5}$$

where Rp is the normal incidence reflection coefficient (same as Ro) and A_o is given by;

$$A_o = B_o - 2\left(1 + B_o\left(\frac{1-2\sigma}{1-\sigma}\right)\right) \quad , \tag{3.6}$$

with $\qquad\qquad\qquad\qquad B_o = \dfrac{\frac{\Delta Vp}{Vpa}}{\frac{\Delta Vp}{\Delta Vpa} + \frac{\Delta\rho}{\Delta\rho a}} \tag{3.7}$
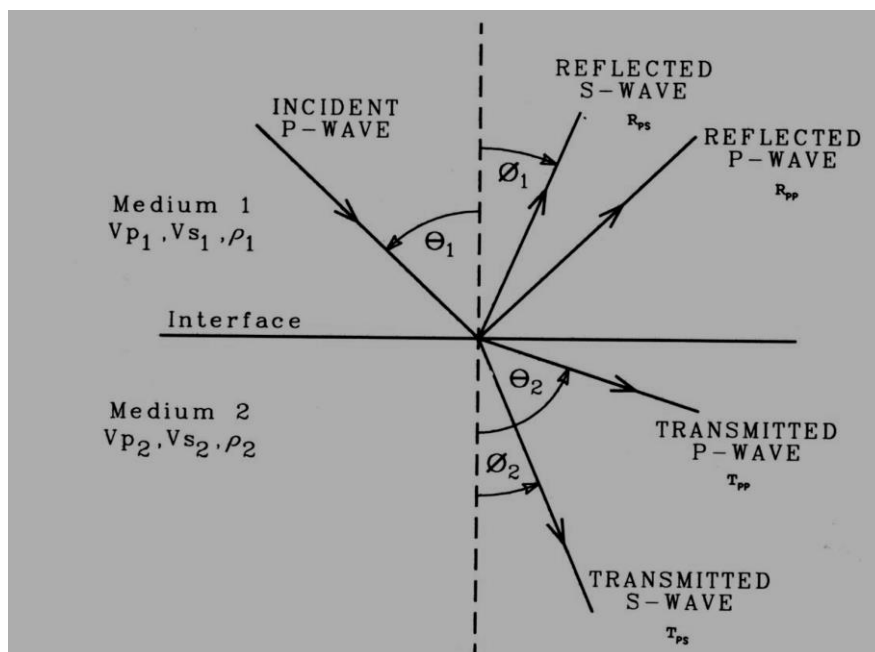
Figure 3.3-1 An incident P wave partitioned into reflected P and S wave and refracted P and S wave on an interface due to acoustic impedance contrast (Castagna and Backus, 1993)

3.4. Seismic Rays and Ray Paths

The elastic waves generated by a seismic source propagates, in homogeneous medium, as circular wavefronts. Seismic rays are a mathematical representation of the propagation direction of the waves and are perpendicular to the wavefronts in isotropic media (Kearey et al., 2013) (Figure 3.4-1).
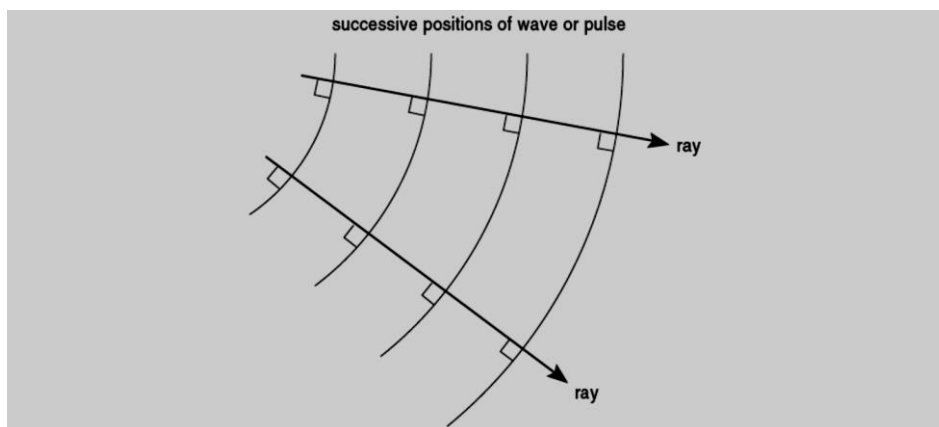
Figure 3.4-1Representation of wavefront and ray paths (Mussett et al., 2000)

The reflection and transmission (refraction) of rays at an interface, where a change of velocity occurs, are governed by Snell's law (Eq. 3.9):

23

$$\frac{\sin \theta_1}{V_{P1}} = \frac{\sin \theta_2}{V_{P2}} = \frac{\sin \emptyset_1}{V_{S1}} = \frac{\sin \emptyset_2}{V_{S2}} \qquad , \qquad (3.8)$$

where V_{P1} = P-wave velocity in medium 1, V_{P2} = P-wave velocity in medium 2; V_{S1} = S-wave velocity in medium 1, V_{S2} = S-wave velocity in medium 2, θ_1= incident P wave angle, θ_2 = transmitted P-wave angle, $\emptyset_1$ = reflected S-wave angle, and $\emptyset_2$ = transmitted S-wave angle.

3.5. Seismic Resolution

Seismic resolution is key factor in seismic because indicating the level of details at which elastic waves can image geological structures. It is dependent on the dominant wavelength (λ), which is given as λ =v/f where f is the dominant frequency, of the data. Generally, both the vertical and lateral resolution decreases with depth due to geometrical spreading, and attenuation, both intrinsic and scattering (Gelius and Johansen, 2012). The resolution can be determined by estimating the dominant frequency and velocity of the layer at a given point (Kearey et al., 2013). The vertical resolution of the seismic data is the limit where two vertical events can be imaged. Generally, the vertical resolution is approximated as the quarter of the wavelength (λ/4).

Lateral resolution is dependent on the Fresnel zone. The ray path gives a point on the interface from where it is reflected but the energy moves in wavefronts form. The area or zone from which the energy is reflected with constructive interference is called the Fresnel zone (Gelius and Johansen, 2012) (Figure 3.5-1). It can be represented in numerical form as

$$R_f = \sqrt{\frac{z\lambda}{2}} \quad \text{or} \quad R_f = \sqrt{\frac{zv}{2f_{dom}}} \qquad , \qquad (3.9)$$

where λ is the wavelength, z is the depth, and f_{dom} is the dominant frequency. After the process of seismic migration (cf. 3.7), however, the lateral resolution is reduced to about half a wavelength in standard 3D seismic. It should ideally be a quarter of a wavelength, as for the vertical resolution, but the limited aperture of seismic surveys (sources and receivers only located at the surface and over a limited extent) prevents that.
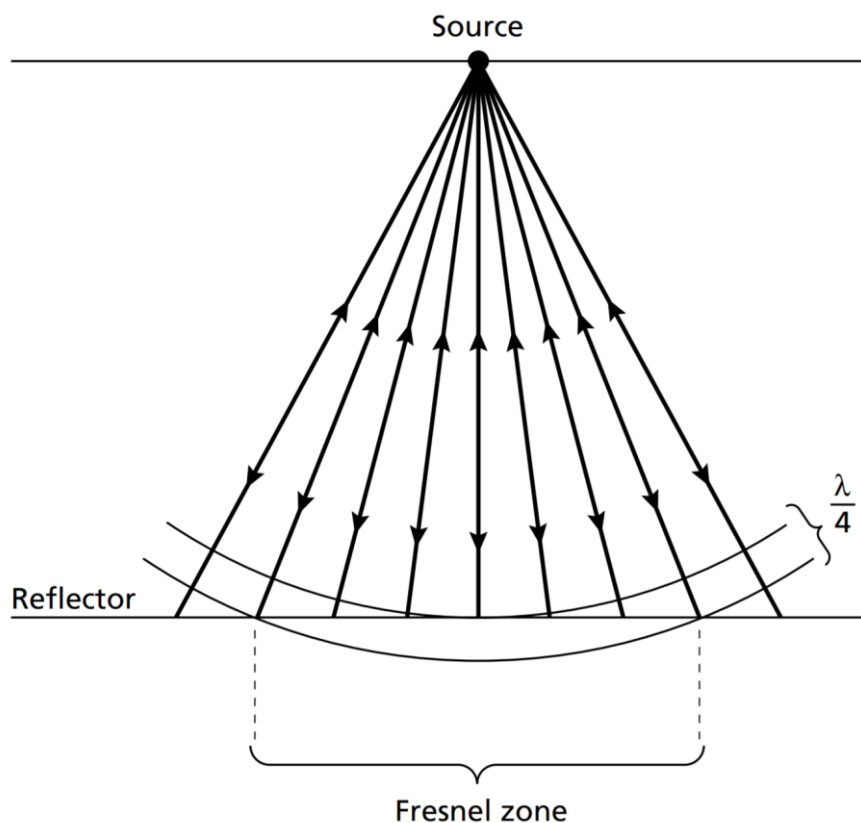
Figure 3.5-1 The reflected rays from an interface within the Fresnel zone (Kaerey et al., 2013)

Note that, in terms of detectability, i.e., whether or not a structure can be "seen" (detected) on seismic, even if not resolved (i.e., one cannot determine its exact form), the limit can reach down to λ/8 to λ/16 or even less, especially on horizontal slices and via seismic attributes, depending upon the frequency content of seismic data, size of structures and impedance contrast.

3.6. Convolution and Fourier Transform

A geological model consists of multiple layers in the subsurface and to relate these layers to seismic data, the mathematical operator of convolution plays a central role. In analogy to electronics, the input signal going through an electronic filter yields an output signal expressed as the convolution of the input signal with the filter. Similarly in seismic, the combined effect of the Earth's structures and the elastic waves can be modeled in 1D by convolving the reflectivity series of ta geological model (input signal; function of the elastic properties of subsurface layers) with a wavelet (the filter; function of the seismic source, propagation effects, etc) (Figure 3.6-1) (Kaerey et al.,2013);.

$$y(t) = g(t) * f(t) \qquad\qquad , \qquad\qquad (3.10)$$

25

where g(t) is the input signal (reflectivity series), f(t) is the filter response (wavelet) and y(t) is the resulting seismic trace.
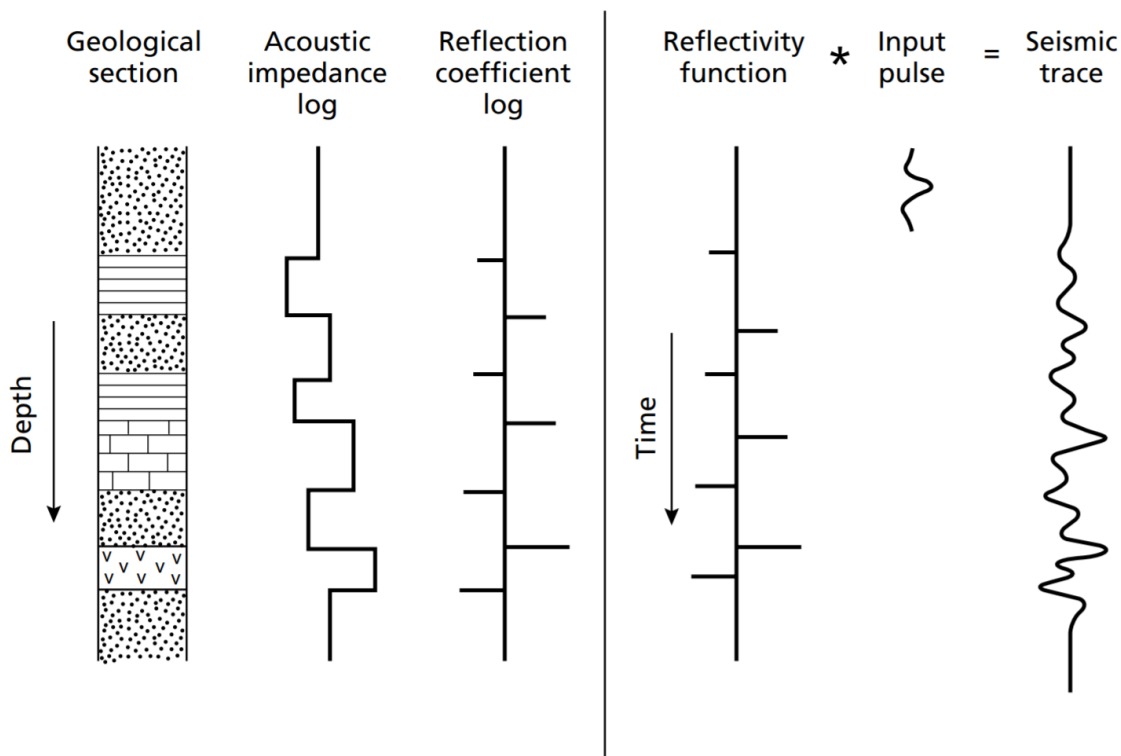
Figure 3.6-1Overview of geological model to seismic trace by convolution of reflectivity series with a wavelet (Kaerey et al., 2013)

The process of convolution takes place in the time domain. The choice of wavelet also affects the output of the synthetic trace. This type of convolution is called 1D convolution (Figure 3.6-2) and is a common industry practice (Lecomte et al., 2015). However, 1D convolution does, e.g., neither account for lateral variation of geological models, nor limited-illumination issues.
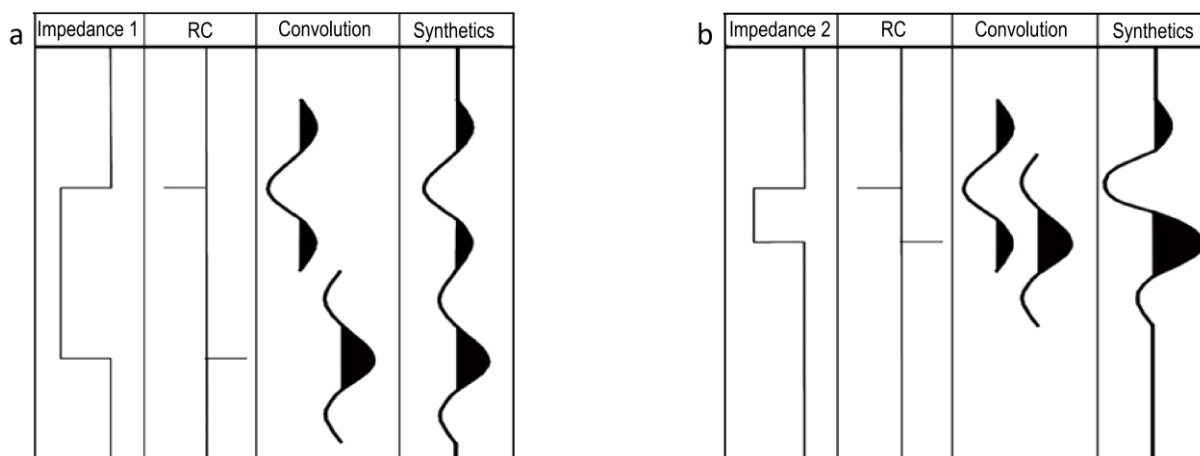
Figure 3.6-2 Examples of 1D convolution where convolved traces are added to generate synthetic trace. a) showing more bed thickness than b) (Huang et al., 2007)

Fourier Transform (FT) is a mathematical method to used convert the time domain data into the frequency domain. A time-domain signal is composed of sine and cosine waves of different frequencies f and having different amplitudes. After FT the same signal will be decomposed into its different frequencies yielding a amplitude spectrum and phase spectrum (Gelius and Johansen, 2012) (Figure 3.6-3). Convolution in the time domain is equivalent to multiplication in frequency as described by the function:

$$g(t) \ = \ FT(G(f)) \qquad , \qquad (3.11)$$

where g(t) is the signal in the time domain and G(f) is the signal in the frequency domain. G(f) can be further described as:

$$G(f) = A(f)e^{i\theta f} \qquad (3.12)$$

where A(f) represents the amplitude spectrum and $e^{i\theta f}$ represents the complex number for the phase spectrum. The time a wave takes to repeat itself or to reach its starting position in the time domain is known as the time period (T) and frequency f is the inverse of that time period (f =1/T). In the space domain, the distance a wave travels within a period T is the wavelength mentioned earlier (Gelius and Johansen, 2012). Similarly to FT in the time domain, which generates amplitude and phase spectrum for different frequencies, FT in the space domain can also be done and it will generate amplitude and phase spectrum for different wavenumbers (inverse of wavelength) which are also called spatial frequencies (Kaerey et al., 2013).

The illumination or resolution of any point in the subsurface is defined by the scattered wavenumber. The plane wavefront perpendicular to the scattering wavenumber can be achieved by performing an inverse FT in the space domain (Lecomte, 2008). The Point Spread Function (PSF) for an image point can be obtained by performing inverse FT from the wavenumber domain to the space domain on set of source receiver-pairs for a given point (Lecomte, 2008).
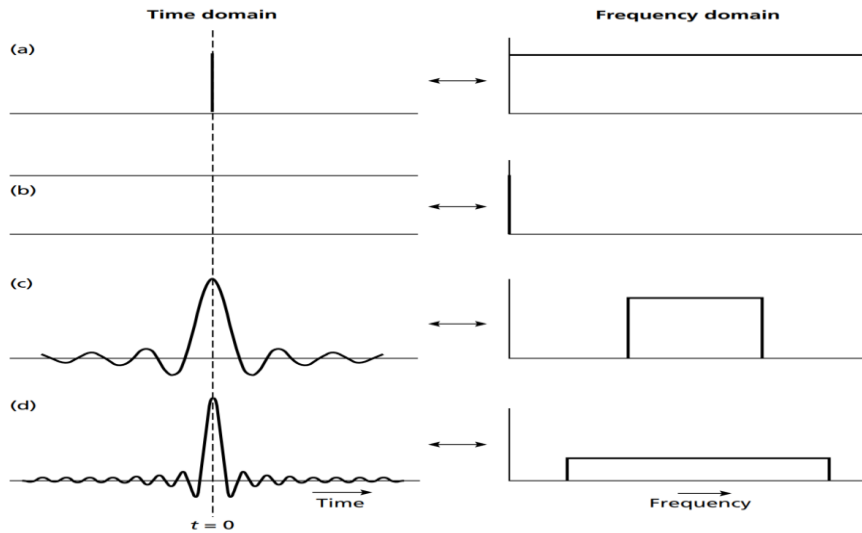
Figure 3.6-3 Fourier transform of different zero phase wavelets (Kaerey et. al., 2013)

3.7. Pre-Stack Depth Migration (PSDM)

As the name suggests, migration is the process of moving the recorded reflection point from recoded position from the source and receiver pair to the actual subsurface location (Herron, 2011). The location of reflection point can be placed at several different locations depending on the time signal was recorded at the receiver (Figure 3.7-1). By applying the migration, the event is geometrically corrected and placed at its actual subsurface location (Sheriff and Geldart, 1995). If the migration is applied on the time domain data before stacking it is known as Pre-Stack Time Migrated (PSTM) seismic data and if it is applied in depth domain before stacking is applied, then it will Pre-Stack Depth Migrated (PSDM) data.
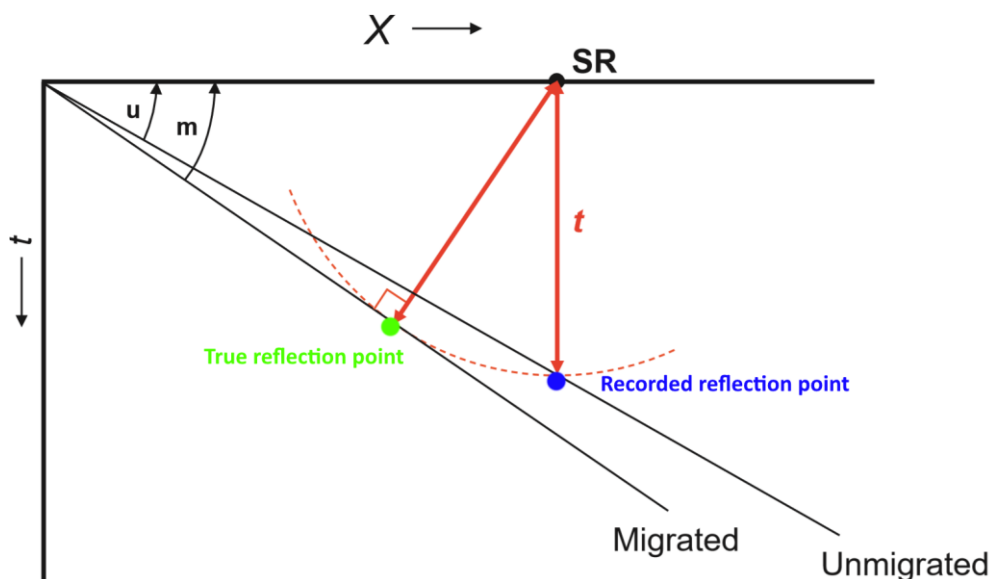
Figure 3.7-1 The case of reflection from dipping layer with angle u in subsurface where the recoded point with time t from source and reciever SR is blow the SR because of zero offset. Point is moved to actual position after migration having dipping angle of m (Herron, 2011)

PSDM is the migration that is applied on shot gather and before stacking of the seismic data and it is applied in the depth domain. The variation in velocity affects the outcome of the subsurface and can change the location of the image point significantly, therefore PSDM is best suited for these areas (Herron, 2011). The 2(3)D convolution modelling used in the present work simulates PSDM images, whereas the 1D modelling generates Post-stack Time Migrated image (Lecomte et al., 2015).

3.8. Illumination Vector and Point Spread Function (PSF)

A key element to explain the seismic modelling used in the present work is illumination vector I_{SR} (Lecomte, 2008). The ray paths are the same as the slowness vector which is perpendicular to the wavefront (Lecomte, 2008). The magnitude of the slowness vector is inverse to the velocity and is usually measured in microseconds per foot (Claerbout, 1985). The slowness vector can be used to define an illumination vector at any point in the subsurface (Lecomte, 2008). The illumination vector will define how many rays will hit the target point and whether it will be resolved or not. In a background velocity model, two local slowness vectors are needed to generate as I_{SR} for each source (S) and receiver (R) of a seismic survey; the slowness vector of the incident wave traveling from the source to the a reference point in the targeted area (p_S) and the slowness vector of the wave traveling from that reference point to the receiver (p_R) (Figure 3.8-1) (Lecomte, 2008).

$$I_{SR} = p_R - p_S \qquad , \qquad (3.13)$$

If the medium is isotropic and there is no wave conversion, both slowness vectors have the same length (because of same velocity v), but their direction/orientation are different, hence generating I_{SR} with different length and orientations (Lecomte, 2008) (Figure 3.8-1 b, c, and d). The length of the generated I_{SR} will affect the resolution of the seismic image. The angle between the incident and scattered wavefield is called the opening angle (θ_{SR}), which constraints that length. Longer I_{SR} results in better resolution than shorter ones; as θ_{SR} increases with increasing offset, the length of I_{SR} decreases with increasing opening angle (Figure 3.8-1 c and d). The best resolution can thus be achieved at zero offset when, i.e., $\theta_{SR} = 0$ corresponding to an I_{SR} length of 2/v, where V is the velocity of reference point.
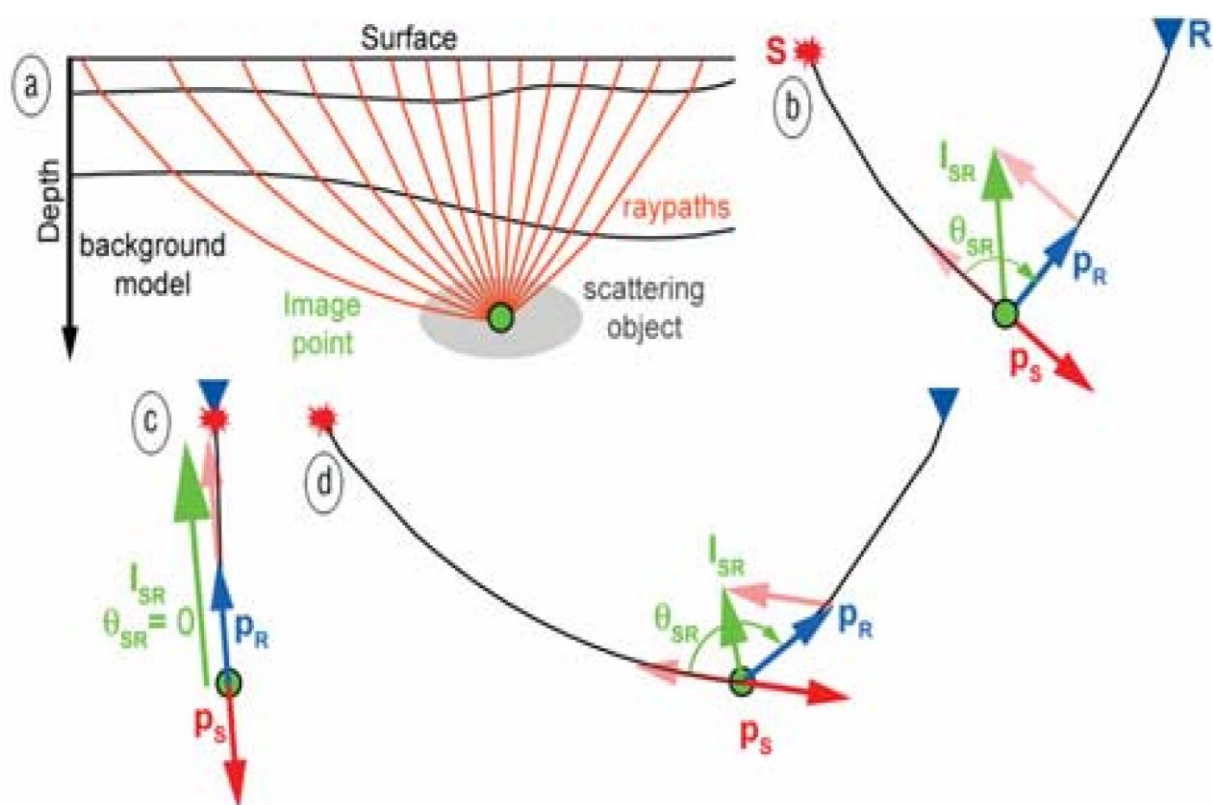
Figure 3.8-1Illustration of the illumination vector. a) Representation of the background velocity model with image point in the subsurface where ray paths are reaching the object passing through different layers. b) Illumination vector I_{SR} is shown for source and receiver with their respective slowness vector p_s and p_r and opening angle θ_s c) Illumination vector for zero offset case d) Illumination vector for higher offset case which cause the decrease in opening angle and resolution (Lecomte et. al., 2008)

After the generation/selection of I_{SR}, wavelet is assigned (Figure 3.8-2 a and b). and a so called, PSDM filter is generated in the wavenumber domain (Lecomte et al., 2008). Applying FT to the PSDM filter yields the Point Spread Function (PSF) in the space domain (Figure 3.8-2c). If the velocity model is not known for the subsurface location, a generic illumination-vector span is generated by assigning an average background velocity for the targeted area (where the seismic image is modelled) and selecting the steepest geological dip of illuminated reflectors (Figure 3.8-3a). Based on this information, a PSDM filter will be generated and a FT on that filter will give the PSF for the modelling (Lecomte et al., 2016).
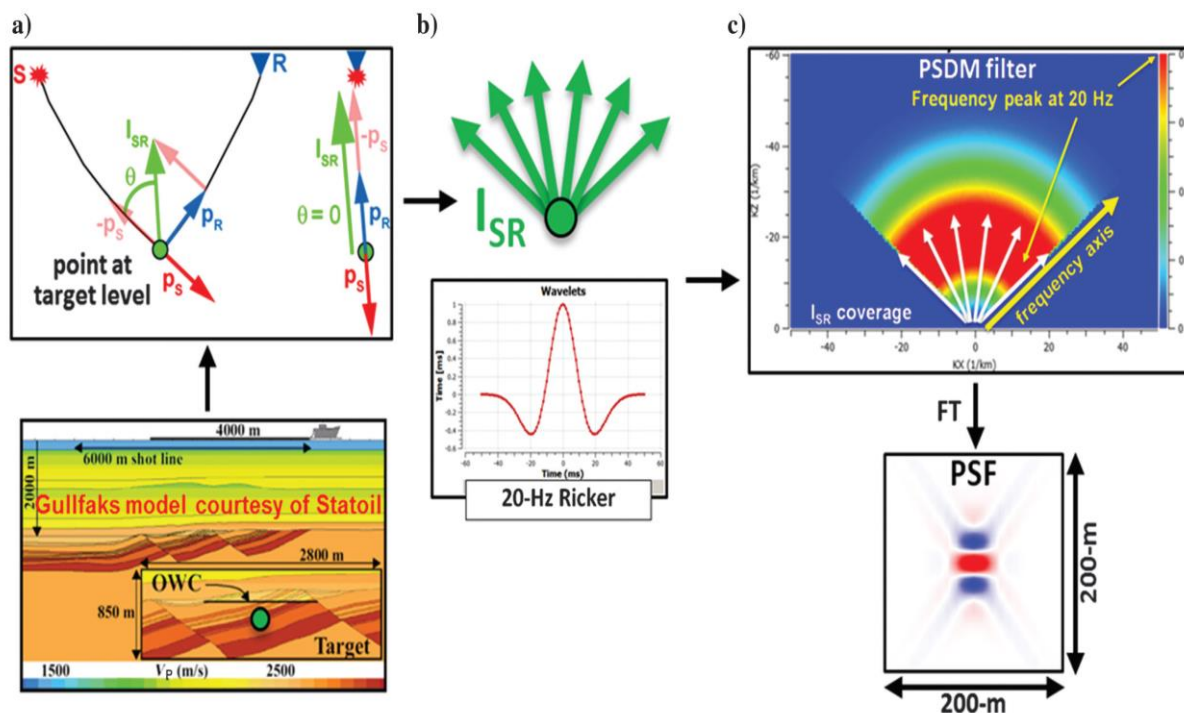
Figure 3.8-2 Description of how PSF is generated a) Illumination vector for a subsurface point in the Gulfaks field represented as green point b) All illumination points I_{SR} and the Ricker Wavelet of 20HZ to be multiplied c) the resultant PSDM filter in space domain having max frequency of 20 HZ as of wavelet d) the PSF generated after applying Fourier Transform (Lecomte et al., 2015)

The shape of the PSF depends on the PSDM filter. The maximum geological dip of illuminated reflectors will control the cross pattern of the PSF (Lecomte et al., 2015). A "perfect" PSF, in the sense of a perfect illumination, would then ideally look like a "thick dot" in the space domain, because all possible dips of the strata are illuminated (Figure 3.8-3b). The "dot" remains, however, thick (about a quarter of a wavelength in all directions) because constrained by both the frequency content of the waves and the velocity at the considered point. These two elements cannot be changed.
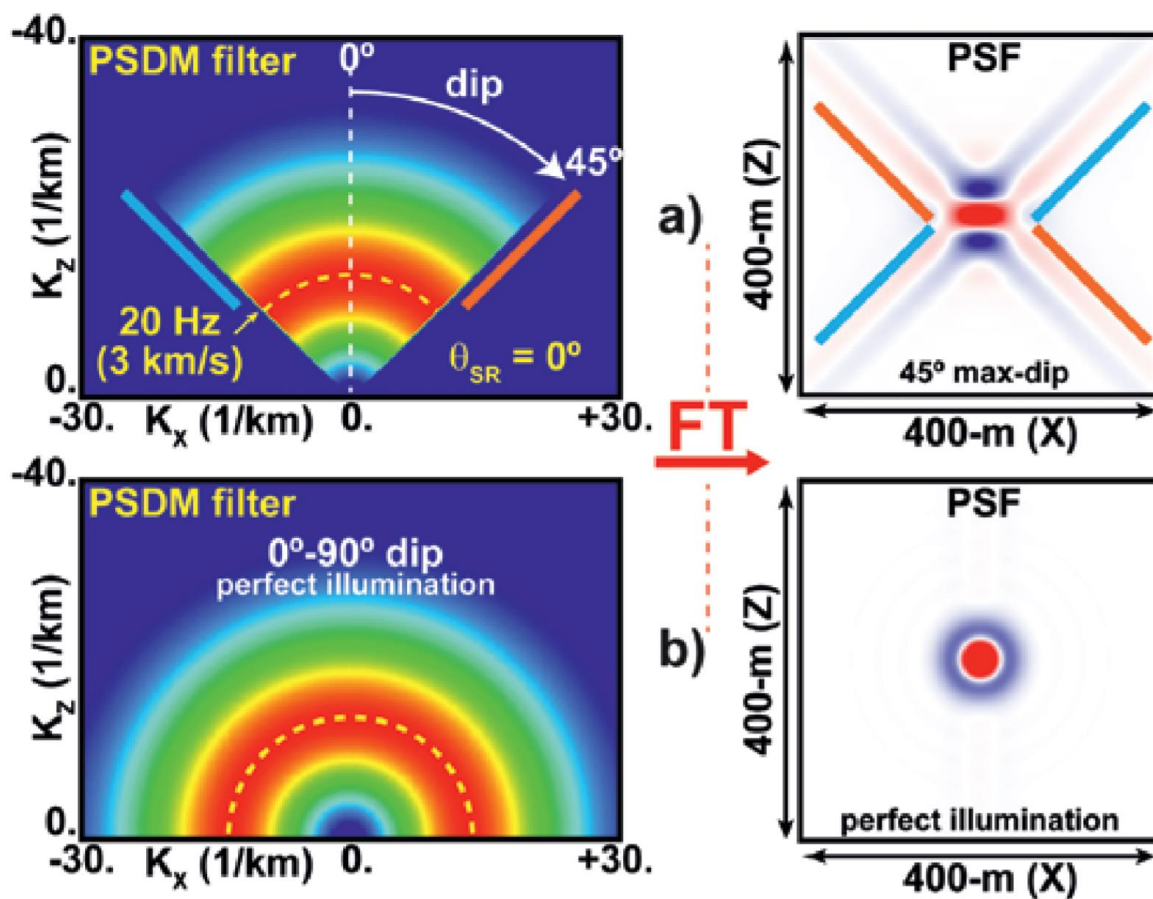
Figure 3.8-3 Illustration of PSF a) Left: PSDM filter with maximum frequency of 20 Hz having zero offset and background velocity of 3 Km/s. The maximum illumination dip is 45 degree. Right: Shows the PSF generated by applying the Fourier transform in the spatial domain. The cross pattrens show ther are perpendicular to each other. b) Same as 'a' where left shows PSDM filter but with perfect iilumination covering all the possible source and recivers span and right showing circular PSF (Lecomte et al., 2016)

Chapter 4

4. Seismic Modelling Methodology

An essential ingredient needed to simulate the seismic, besides geological structure itself, are the associated elastic properties (e.g., Vp, Vs, and density), making it possible to generate the reflectivity model. Such elastic parameters can either be calculated from the actual well logs recorded in the field, or they can be estimated by using petrophysical properties (i.e., porosity, mineral composition, fluid content, etc) through rock physics modelling (Johansen, 2018). The general method for seismic modelling of paleokarst reservoirs is through rock physics modelling. But rock physics modelling for carbonates, especially in the context of paleokarsts, is a very challenging topic (Johansen, 2018). An important issue is, e.g., porosity because it can reach critical porosity, at least for a certain portion of the reservoir, making it difficult to estimate accurate bulk and shear moduli for the rocks. Therefore, there is not yet a well-defined workflow for modelling elastic parameters of such reservoirs. In this study, a new approach is carried out to generate the paleokarst reservoirs models, this in relation to the Loppa High cases.

4.1. Seismic Data

Seismic data are the first and most important building blocks for input of proper geomodels into seismic modelling. A common approach generally uses Pre-Stack Time Migrated (PSTM) seismic volumes to infer the geological structure, especially the surrounding ones. Seismic interpretation is carried out to generate surfaces of the key horizons and then depth conversion is applied to build a geomodel in depth. However, in this study, the data provided by Lundin Norway were a Pre-Stack Depth Migrated (PSDM) seismic data volume, hence no need for depth conversion. The dominant frequency of these data lies between 25 and 30 Hz. The data quality is poor-to-fair in the study area with fair horizon continuity and poor-to-fair fault visibility in the area of interest (AOI).

4.2. Seismic Interpretation

The seismic interpretation used in the modelling workflow is based on the work done by Lundin Norway. A total of four horizons were provided which included the; Top Havert Formation, Top Permian-Triassic (PT) Unconformity, Top Falk Formation, and Top Ugle

Formation, The Top Orn formation is considered to be the PT unconformity top until the Orn formation pinches out and the PT unconformity is converted into the Falk formation. The formation above the PT unconformity is the Havert Formation (Figure 4.2-1). Overall, the thickness of layers increases in the south-east (SE) direction whereas it decreases in the north-west (NW) direction because of the uplifting and erosion on the PT unconformity (Figure 4.2-2).
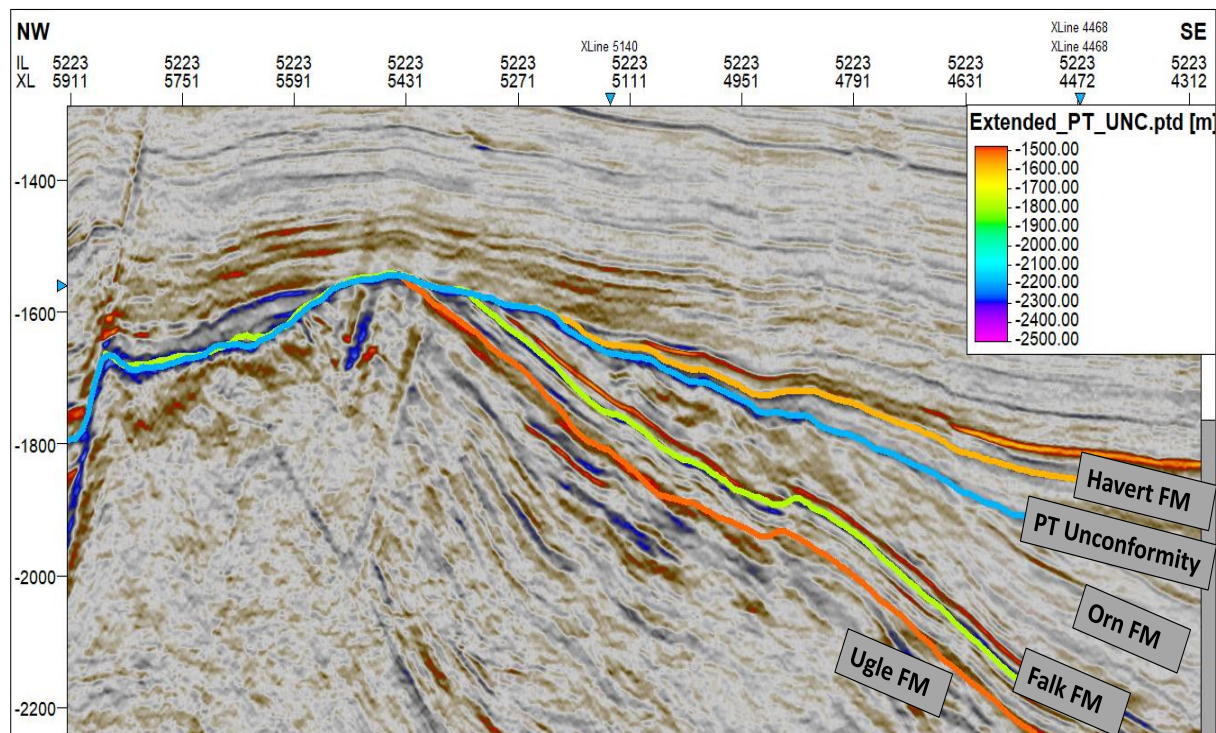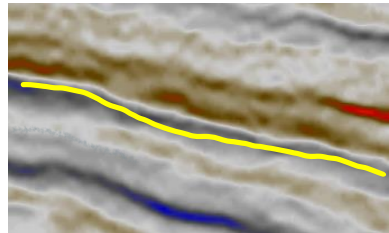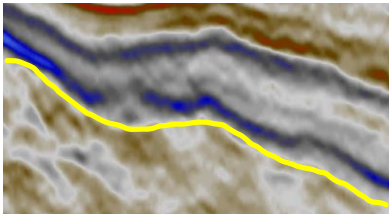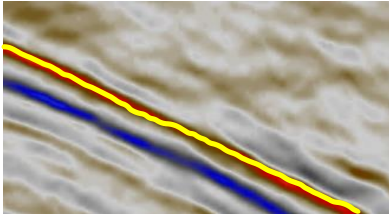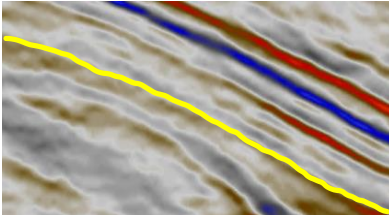
Figure 4.2-1 Seismic Inline 5223 from the PSDM seismic volume showing the interpreted horizons and structure geometry. Note the thickness increase in the SE direction in the section.

The Havert formation is onlapping on the PT unconformity whereas the formations below the unconformity are truncated in the NW direction. This shows that the crestal part of the formations was eroded, making it a pinch-out trapping mechanism. In the crestal part, the Triassic section lies above the basement.

Table 4.2-1 Reflection seismic signatures of the interpreted horizons with SEG normal polarity in the study area

Name	Seismic Phase	Reflection Properties	Seismic Signature
Havert Formation	Trough (negative amplitude)	Medium-to-high amplitudes, continuous to discontinuous reflector	
PT Unconformity	Peak (positive amplitudes)	High Amplitudes, continuous reflector	
Falk Formation	Peak (positive amplitudes)	High Amplitudes, continuous reflector	
Ugle Formation	Peak (positive amplitudes)	Medium-to-high amplitudes, continuous to discontinuous reflector	
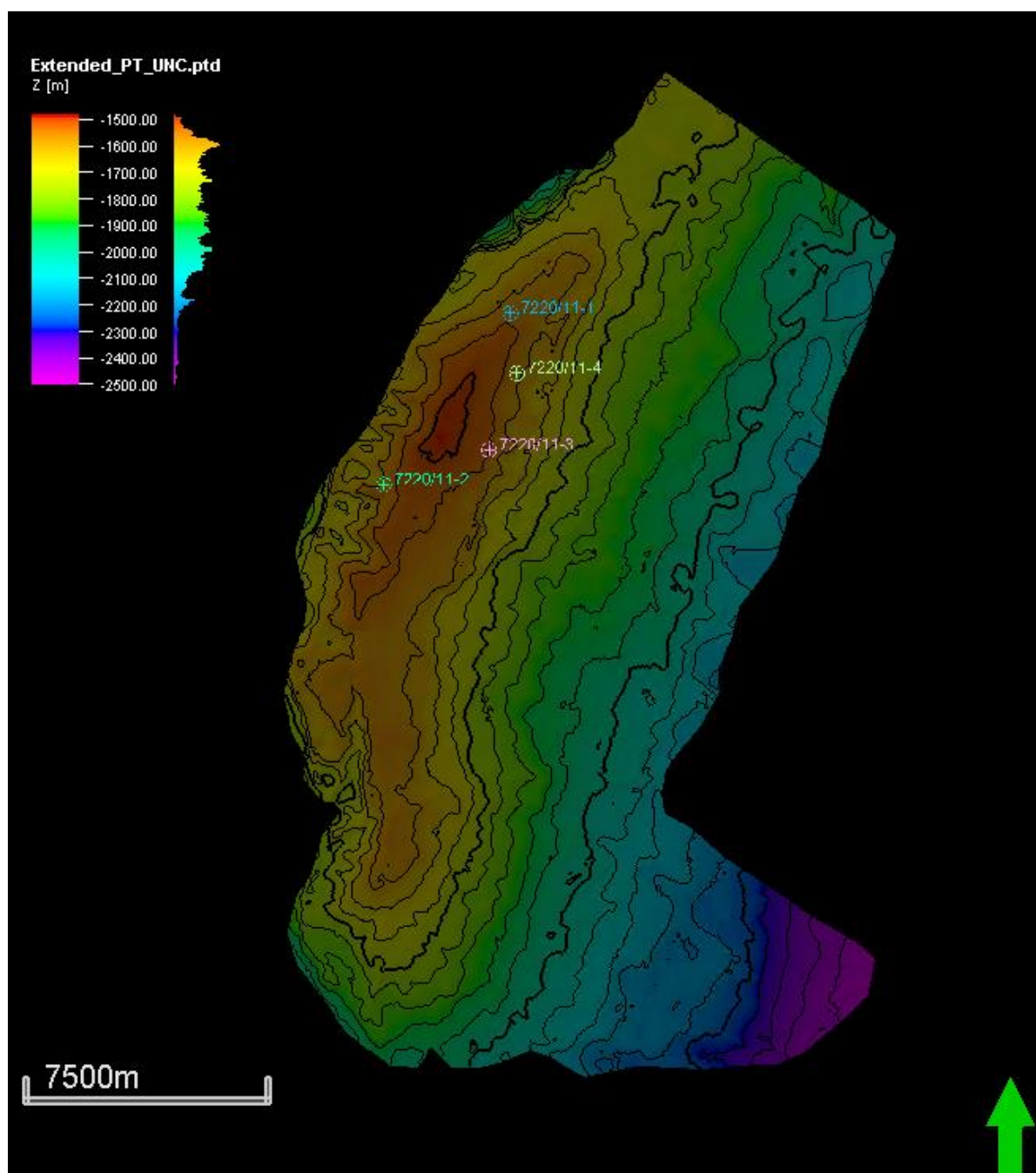
Figure 4.2-2 Depth map of the PT unconformity with well locations of Alta field

4.3. Generating Geological Models

The next step after the interpretation of the seismic data is to generate geological models. The geological model used in the study is based on the structural model of the Alta field discovered in the Barents Sea (www.npd.no) whereas the cave model used in the study is from the Agios Georgios cave in northern Greece (Lonoy et al., 2020) (Figure 4.3-1). The cave model was repositioned to the study area to represent the presence of paleokarst in geomodels. The cave model was positioned between the PT unconformity and Falk formation.

36

The Orn formation comes below the PT unconformity and above the Falk formation (Figure 4.3-2).

Paleokarst facies
14 ▢ Higly disturbed strata
13 ▢ Disturbed strata
12 ▢ Coarse chaotic breccia
11 ▢ Open cavern
10 ▢ Sediments + Fine chaotic breccia
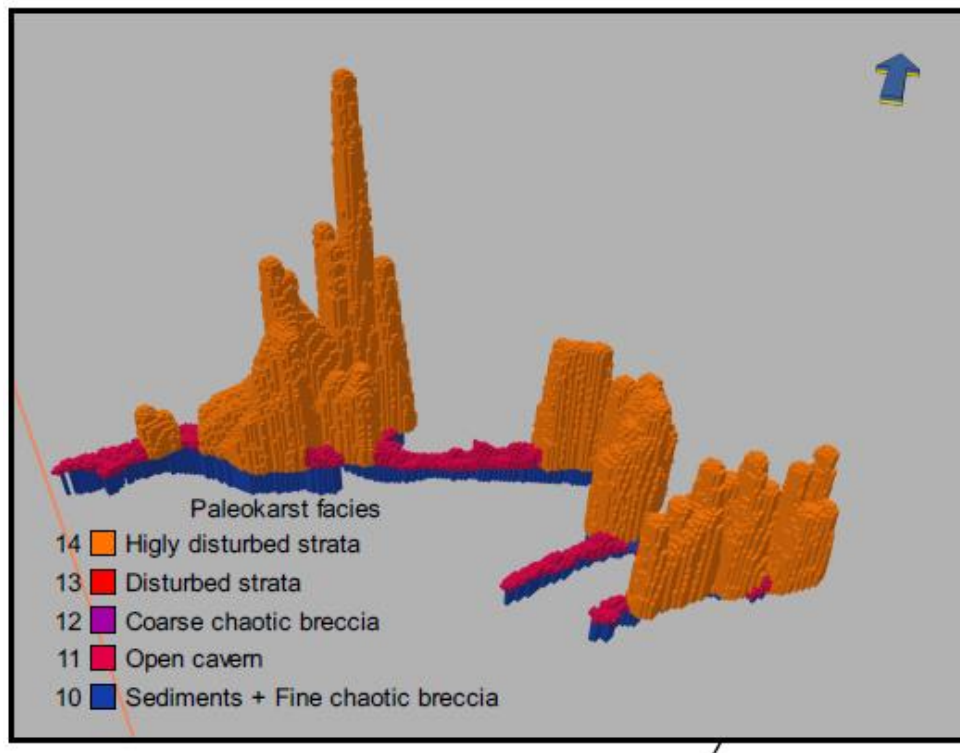
Figure 4.3-1 Cave model of Agios Georgios Cave system with associated Paleokarst facies

The cave model is approximately 300 m x 200 m in width and 200 m in height and is placed near the Alta-3 well (7220/11-3). The reason for placing the cave model near this well is that Alta-3 encountered a bit-drop during drilling, so modelling this area could give some insight to the real seismic data. The seismic model has the same lateral dimension as the cave model whereas vertically it spans from 1450m to 1650m.

To understand the effect of lithology and fluid saturation on paleokarst reservoirs, several models were generated. The elastic input data for the different models includes the actual data recorded in the wells and empirical calculations from the actual well data.
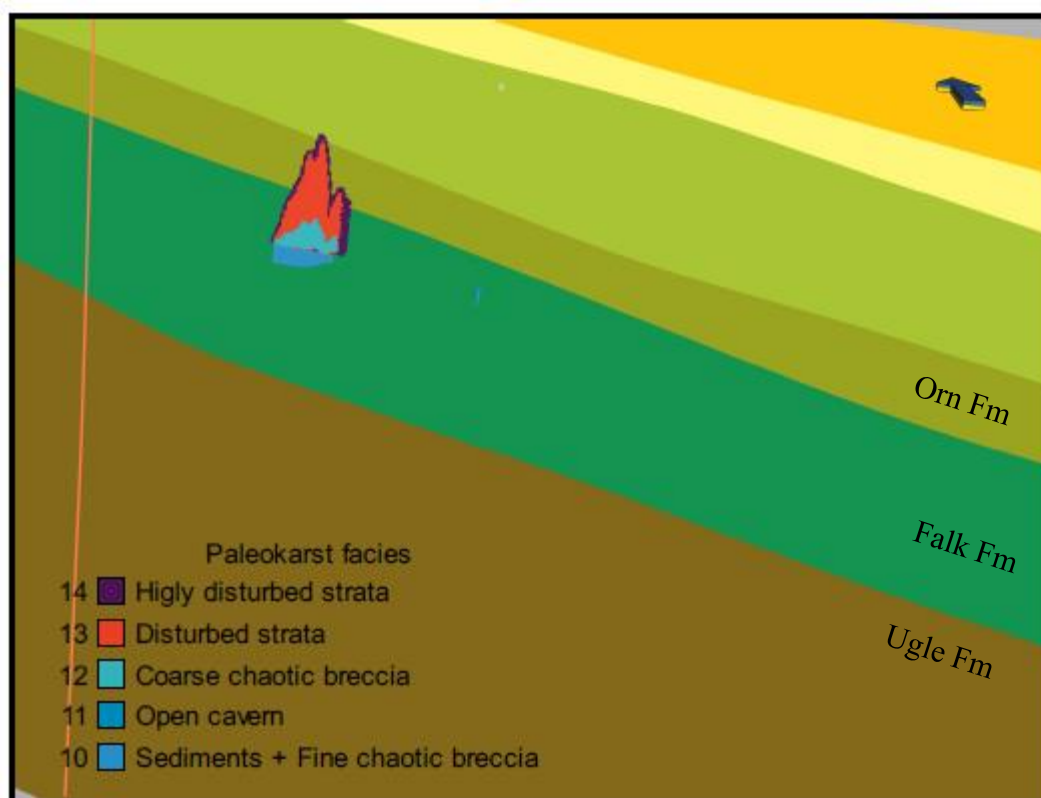
Figure 4.3-2 Representation of the cave in a cross section within the reservoir model with different lithological formations and paleokarst facies indicated.

4.4. Models

Paleokarst reservoirs are highly heterogeneous in nature and their properties can vary significantly laterally. There is no single model that can give a perfect match with the actual representation of the subsurface at considered location, due to the inherent limits in seismic images (cf, chapter 3). However, to attempt accounting for the changes in the host rock and the paleokarsts, four distinctive reservoir models were constructed (Table 4.4-1). The common feature between all the models is the same porosity model, which is populated based on well data (Figure 4.4-1). The cores analyses and thin sections of Alta wells gave an estimate of the actual porosity of the subsurface and are representative of both the host rock and the karsts.

Table 4.4-1 Table of the generated models for modelling

Model	Host Rock: Vp, Vs, Rho	Paleokarst Vp, Vs, Rho	Oil or Water Saturation	Comments
1	Log	N/A	N/A	Background Model
2	Cal	Cal	100 % So	All dolomite
3	Cal	Cal	100 % So	Permian: Dolomite Triassic: Shales
4	Cal	Cal	70% So 30% Sw	All dolomite

The porosity of host rocks ranges from 2% to 10 % whereas the porosity for the karsts ranges from 5% to more than 80% where there are open caverns (Figure 4.4-1). Other properties required for the seismic modelling were either populated purely from the well data or calculated via an empirical relationship established from porosity (cf. Chapter 5 Model 2)
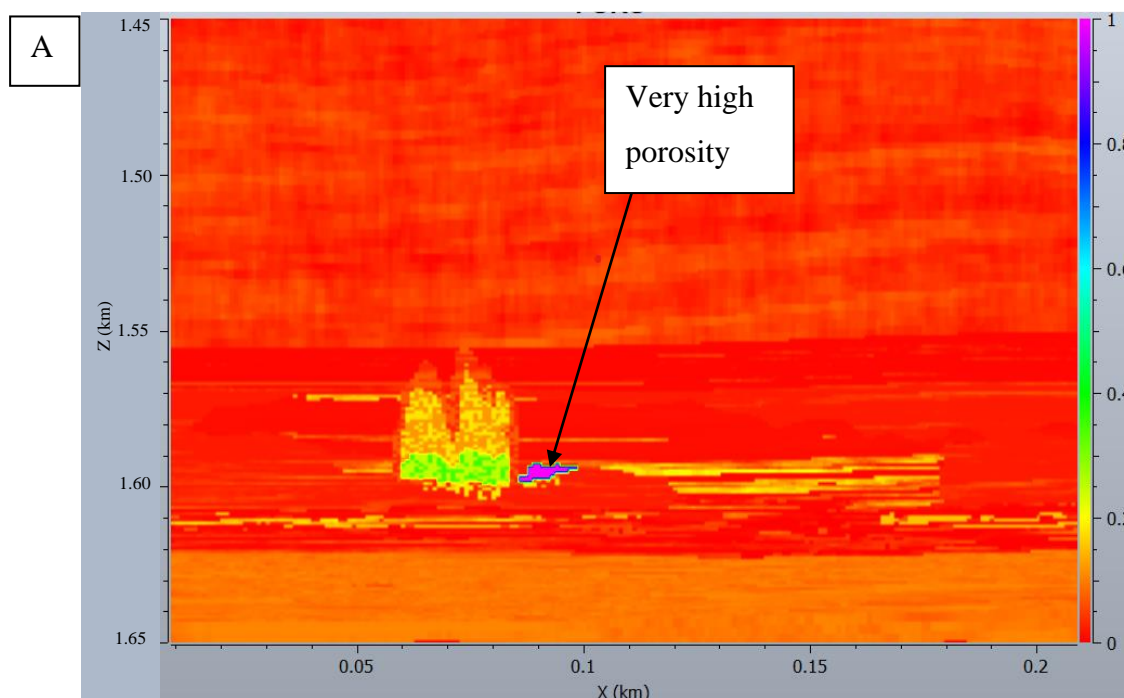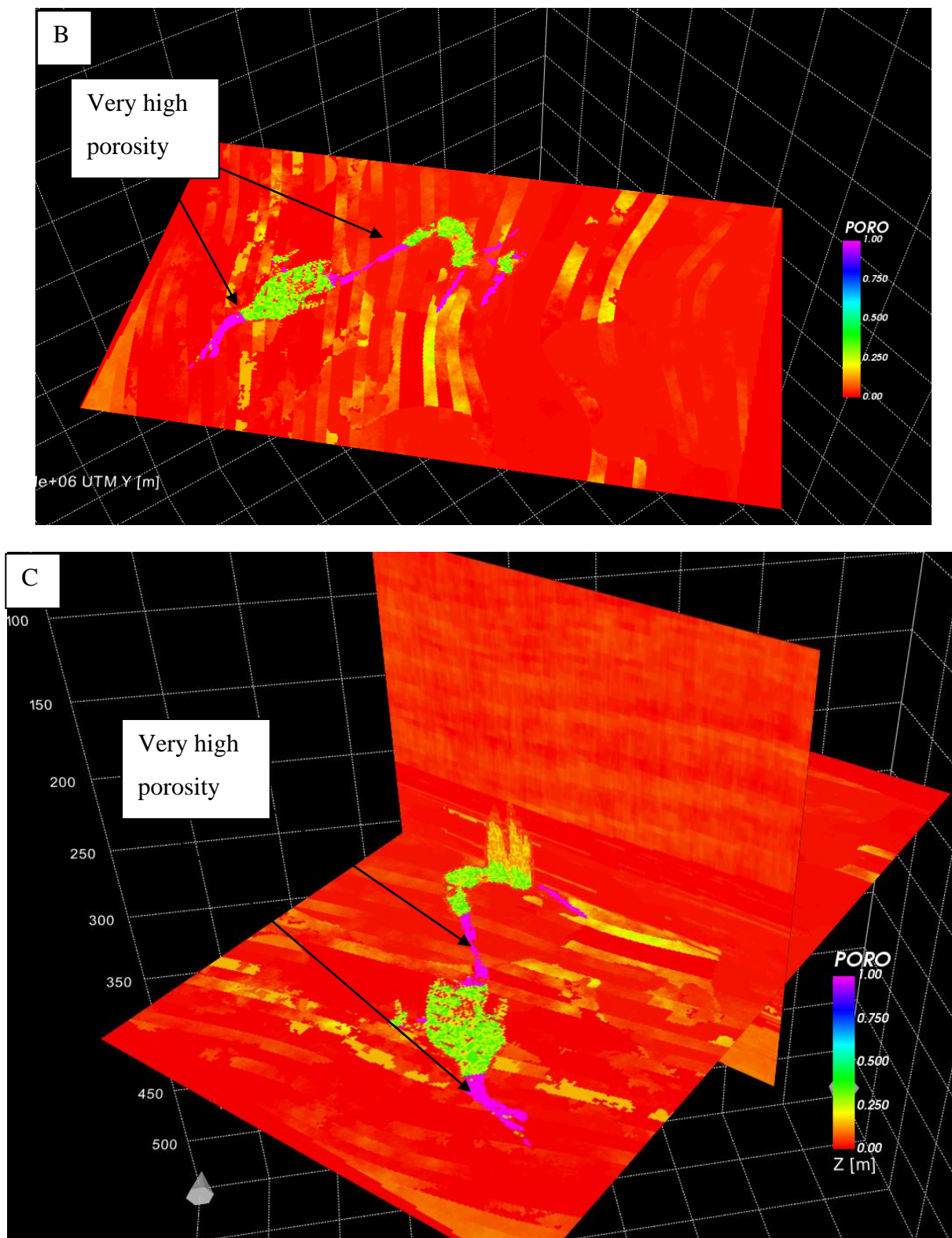
Figure 4.4-1 The porosity model used for all the models A) shows the porosity in cross sectional view and B) shows the porosity in slice view C) intersection view of A &B. Porosity is very low in the host rock with a range from 2% to 10% whereas in the paleokarst, it changes significantly depending upon the type of paleokarst facies. In the open caverns it can go up to 100% as no host rock is present.

40

4.5. 3D Seismic Modelling

The seismic modelling starts by importing geological models. Then the elastic properties were generated by using either the actual well values or by calculating them with the empirical formula (cf. Chapter 5). The P impedance and reflectivity are then generated for the different models. The last step to compute the synthetic seismic is to convolve the reflectivity models with a PSF. The PSF were generated analytically in this study, in lack of information about velocity model, acquisition-survey geometry, wavelet etc.The standard values used for the seismic modelling include a maximum illumination angle of 45°, as a proxy of a standard 3D acquisition (Dimmen et al., 2022), and a wavelet with a dominant frequency of 30 Hz because being close to actual seismic data. The angle of incidence was set 0° (zero offset) and primary-P reflection (PP) are considered, the original data being processed as such, i.e., not converted waves considered (Table 4.5-1).

Table 4.5-1 The description of standard parameters used in the modelling study.

Maximum illumination angle	45°
Average velocity	3.5 km/s
Angle of incidence	0°
Wavelet- dominant frequency	30 Hz
Reflection mode	P-P

4.6.Sensitivity analyses

Sensitivity analyses were carried out on the background model (model 1) to select the parameters which will provide the best results. The 3D seismic modelling based on the PSF convolution with an input reflectivity grid can shed light on the impact of variations of parameters on the illumination and resolution of seismic (Dimmen et al., 2022 & Johansen, 2018). The sensitivity was performed by varying some of the available parameters, including wavelet (dominant frequency) and illumination angle. 1D convolutional models were also generated to compare with the 3D models and see the effect of resolution. The changes in lithology and fluid saturation were accounted for in the geological models. The host reservoir rock is set to dolomite in all cases and the values used for the background model were populated from the Alta-3 well (7220/11-3). The list of varying parameters is:

- dominant frequency of wavelet (Hz): 30, 45 and 60 Hz

- maximum illumination angle (°): 1D, 45 and 90

- host rock: dolomite, dolomite and Triassic shales

- fluid saturation (%): 100, 70 & 30

4.7. Modelling workflow summary

The entire modelling workflow used in the present work is summarized in (Figure 4.7-1).
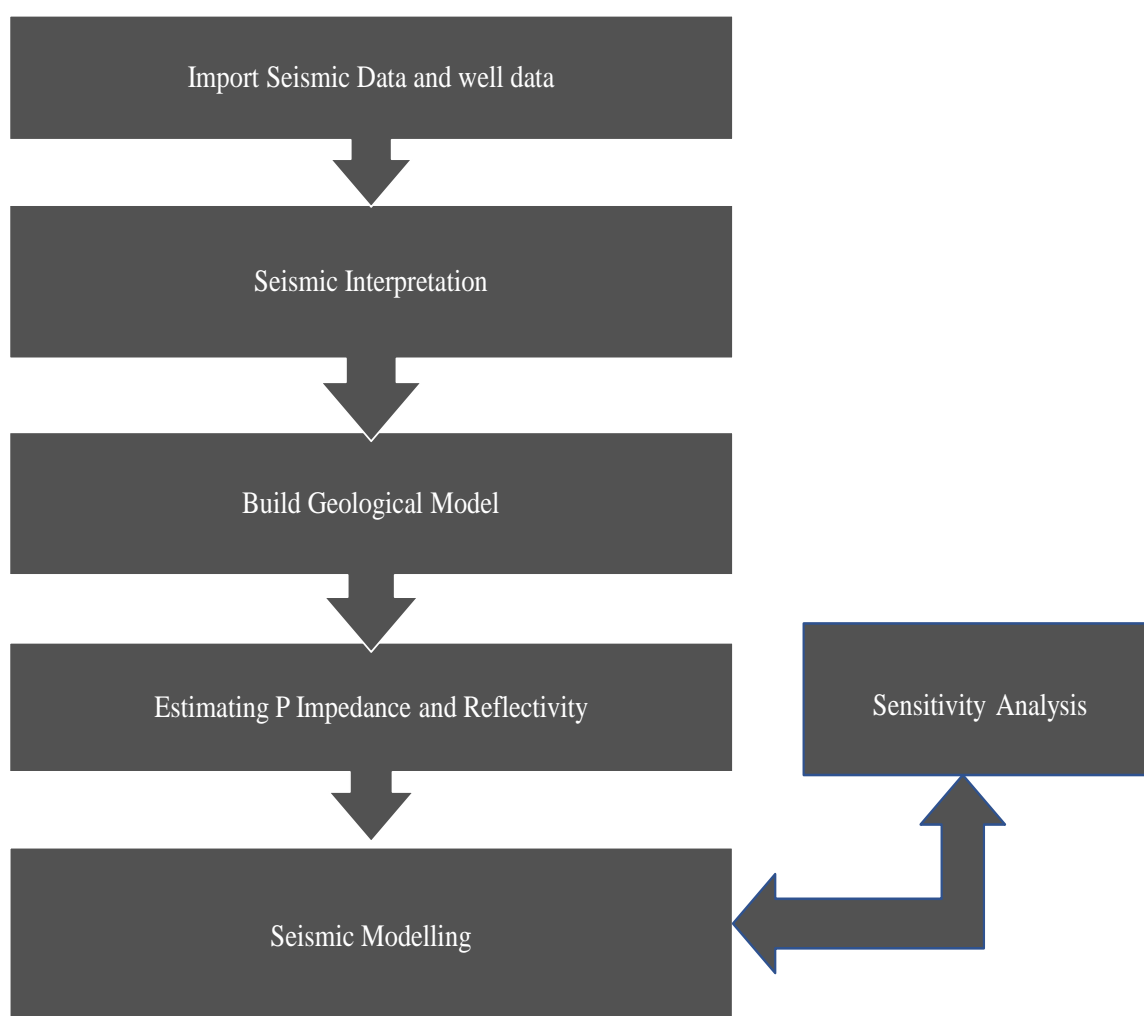
Figure 4.7-1 The workflow performed while doing the seismic modelling.

Chapter 5

5. Results

In this chapter, the results of the study will be shared. The results are based on the background and methodology explained in the former chapters. First, the P-Impedance and reflectivity calculated from Vp, Vs, and ρ (Appendix A, Appendix B, Appendix C, and Appendix D) will be explained for each model, secondly, sensitivity on the background model will be presented, and the choice of wavelet will be made according to the results. The corresponding wavelets and subsequent PSF will be used for modelling of models 2, 3, and 4. Thirdly, the 1D convolution modelling will be displayed for comparison and, in the end, the results of 3D seismic modelling will be illustrated.

5.1. Generation of reflectivity

5.1.1. Model 1

The properties needed to model seismic data include Vp, Vs, and ρ. The first model used for seismic modelling is the layer cake model in which the properties for host rock and paleokarst were used from the actual well logs of Alta 3 (7220/11-3) well (Appendix E). All properties were populated in the layered model as single-point data and therefore do not show any variation between the host rock and paleokarst features. Using the elastic properties, which are Vp (Figure 5.1.1-1), Vs, and ρ, P-impedance (PIMP) can be calculated (Figure 5.1.1-2) as well as the reflectivity (Ro) in the present study, the latter being the necessary input to the PSF-based convolution modelling (Figure 5.1.1-3). This model can be considered as a background one.

Figure 5.1.1-1 Geological model of model 1 representing Vp (km/s) in vertical (YZ) direction at X = 0.1745 km.
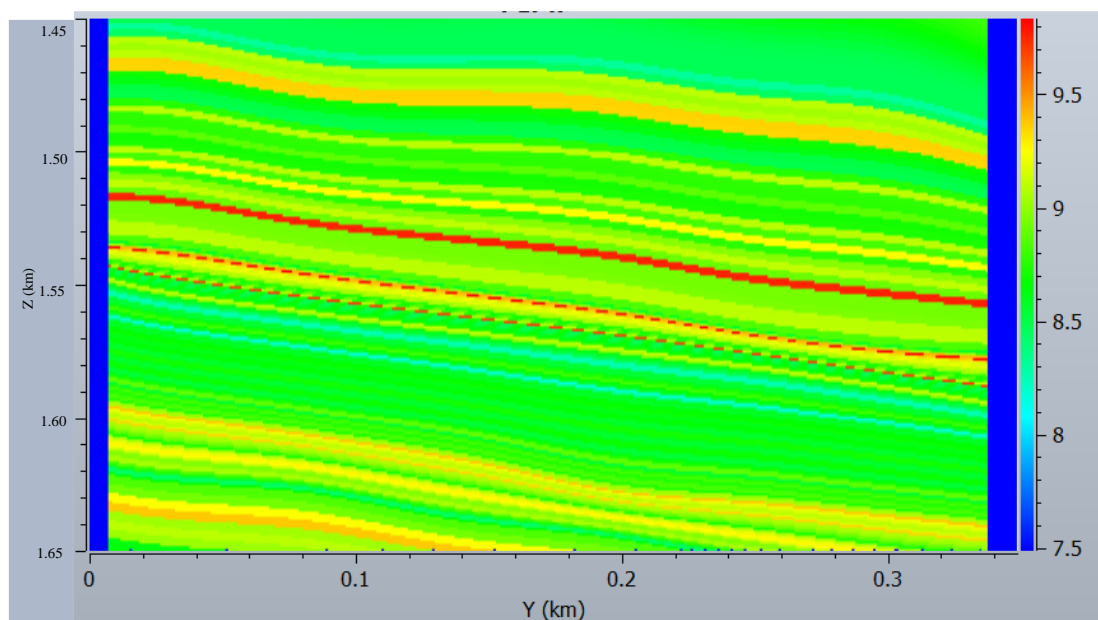
Figure 5.1.1-2 P Impedance (PIMP) of the model 1 in vertical (YZ) direction at X = 0.1745 km. There is no difference between host rock and the paleokarst features.

44
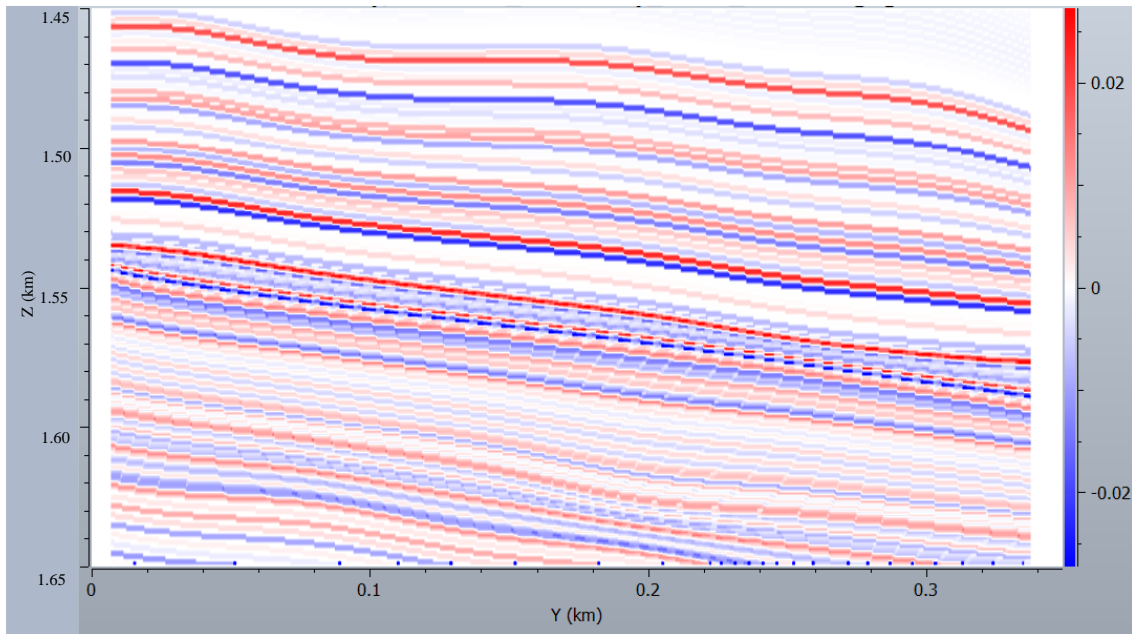
Figure 5.1.1-3 reflectivity of model 1 in vertical (YZ) direction at X = 0.1745 km, depicting smooth reflectors.

5.1.2. Model 2

As model 1 does not include any variation among the lithology and paleokarst, a different approach is taken for Model 2. The most important factor for seismic modelling is the (acoustic) impedance, hence a combination of Vp and ρ. To account for the changes in host-rock and karsts, the available porosity model was used (see Figure 4.4-1). The time average equation of Wyllie et al. (1958) states that the slowness (inverse of velocity) is dependent on the matrix and pore fluid present in the rocks. It is described as

$$\frac{1}{V_p} = \frac{(1-\Phi)}{V_m} + \frac{\Phi}{V_f} \qquad , \qquad (4.1)$$

where Vp is the overall P wave velocity of the rock, V_m is the P-wave velocity of the matrix alone; and V_f is the P-wave velocity of pore the fluid and Φ is the porosity. Raymer et al. (1980) proposed an improved version of the Eq. 4.1 with a new empirical transform based on extensive field observations of transit time versus velocity. This transformation is known as the Raymer-Hunt Gardner model.

$$V_p = (1 - \Phi)^2 V_m + \Phi V_f \qquad , \qquad (4.2)$$

For the case of S-wave velocity the expression will change, as the velocity of S waves, the ΦV_f term will be zero because the shear waves cannot pass through the liquids. So, the expression will be only for the solid part.

$$V_{sDry} = (1 - \phi)^2 V_{sm} \qquad , \qquad (4.3)$$

where V_{sDry} is the S-wave velocity of dry rock and V_{sm} is the S-wave velocity of solid phase. For wet case the equation can be written as (Dvorkin 2008)

$$V_{sWet} = V_{sDry}\sqrt{\rho_{bDry}/\rho_{bWet}} \qquad , \qquad (4.4)$$

where V_{sWet} is the S-wave velocity of wet rock, V_{sDry} is the S-wave velocity of dry rock, ρ_{bDry} and ρ_{bWet} is the bulk density of dry and wet rock respectively. The calculations for density were performed on the following expression (Saberi 2017).

$$\rho = (1 - \phi)\rho_m + \phi\rho_f \qquad , \qquad (4.5)$$

where ρ_m is the matrix density, ρ_f is the pore fluid density and ϕ is the porosity. In model 2 the host rock is considered as 100% dolomite and fully saturated with oil, to only account for the lateral changes in host rock and paleokarst features. Same as model 1 the PIMP (Figure 5.1.2-2) and reflectivity (Figure 5.1.2-3) were generated using the elastic properties (Figure 5.1.2-1).

Table 5.1.2-1 The values used for estimation of velocities and density in Model-2, Model-3 and Model-4.

Material	Vp (m/s)	Vs (m/s)	Rho (g/cm³)
Dolomite	5000	2750	2.84
Triassic Shales	1800	500	2.115
Water	1475	N/A	1
Oil	1225	N/A	0.875

The shear wave cannot pass through the liquids. Generally, the pore spaces are small and even though the pores are filled with fluids there is Vs for the rock. But in this study, there are few areas where there is no host rock present, and the open space is filled with fluids so for these places where there are open caverns the value used for Vs is close to zero.
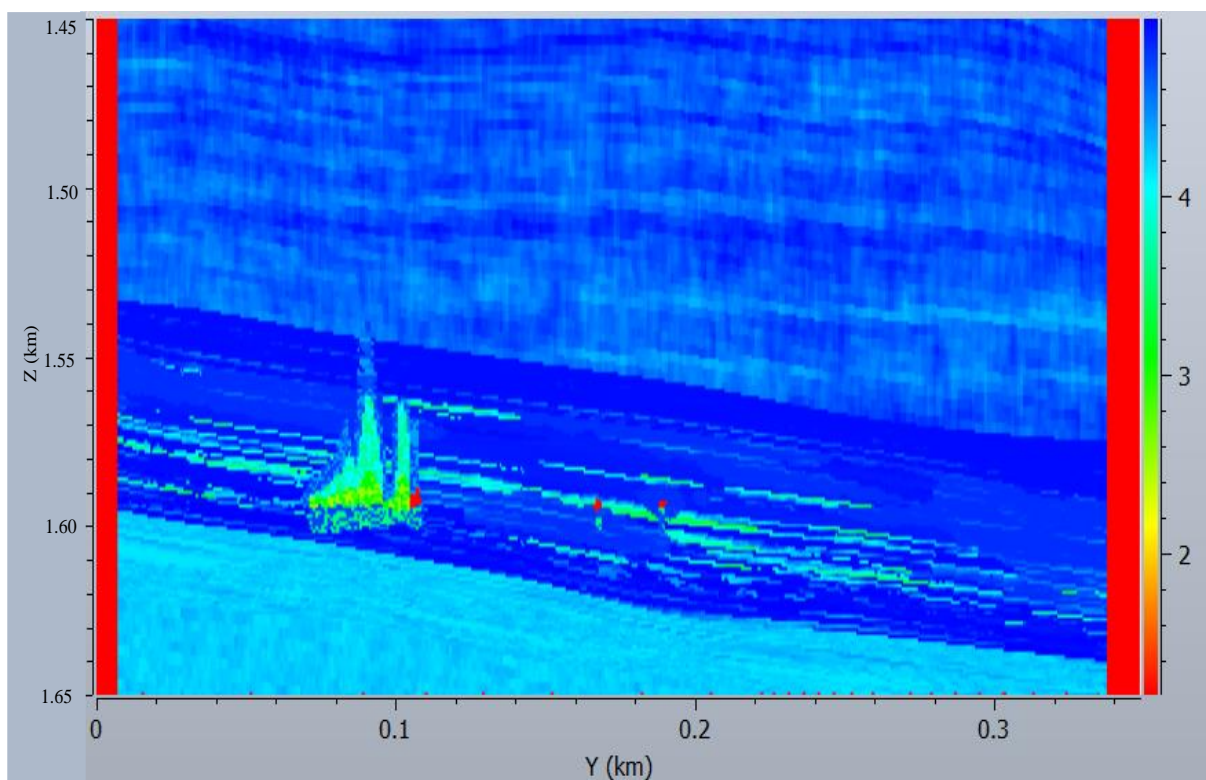
Figure 5.1.2-1 Geological model of model 2 represented with Vp (km/s) in vertical (YZ) direction at X = 0.109 km
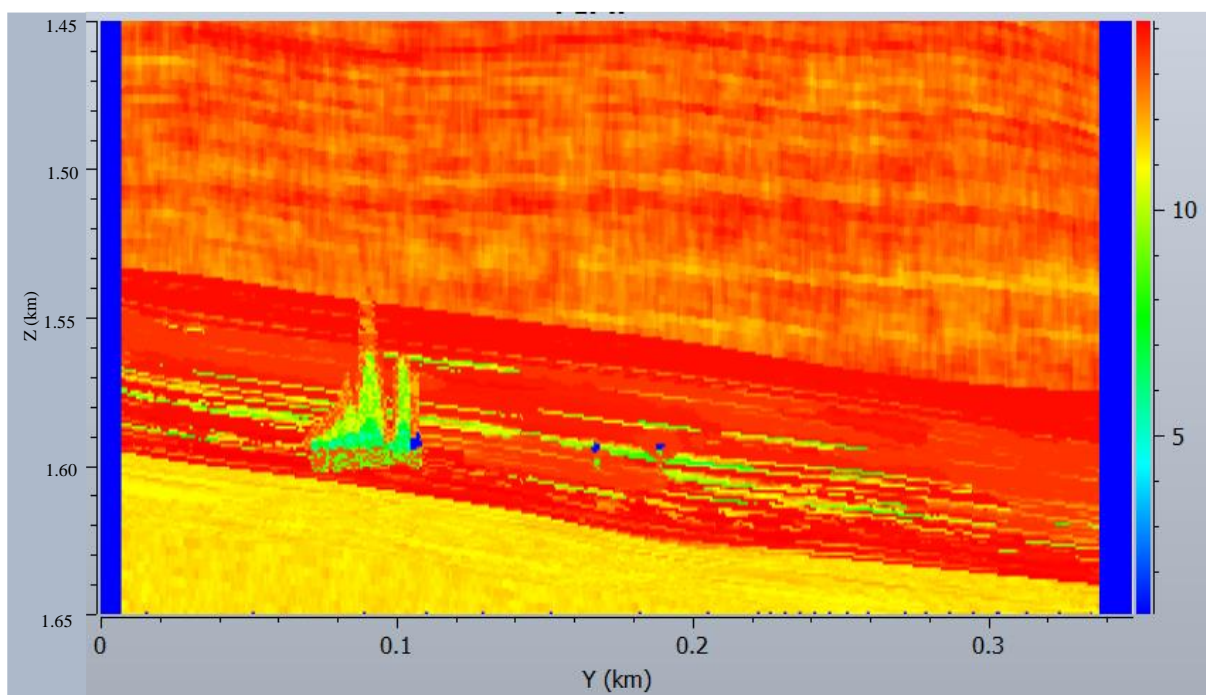
Figure 5.1.2-2 P Impedance (PIMP) of model 2 in Vertical (YZ) direction x = 0.109 km The cave system can clearly be seen on the P Impedance with chaotic behavior between straight strata.
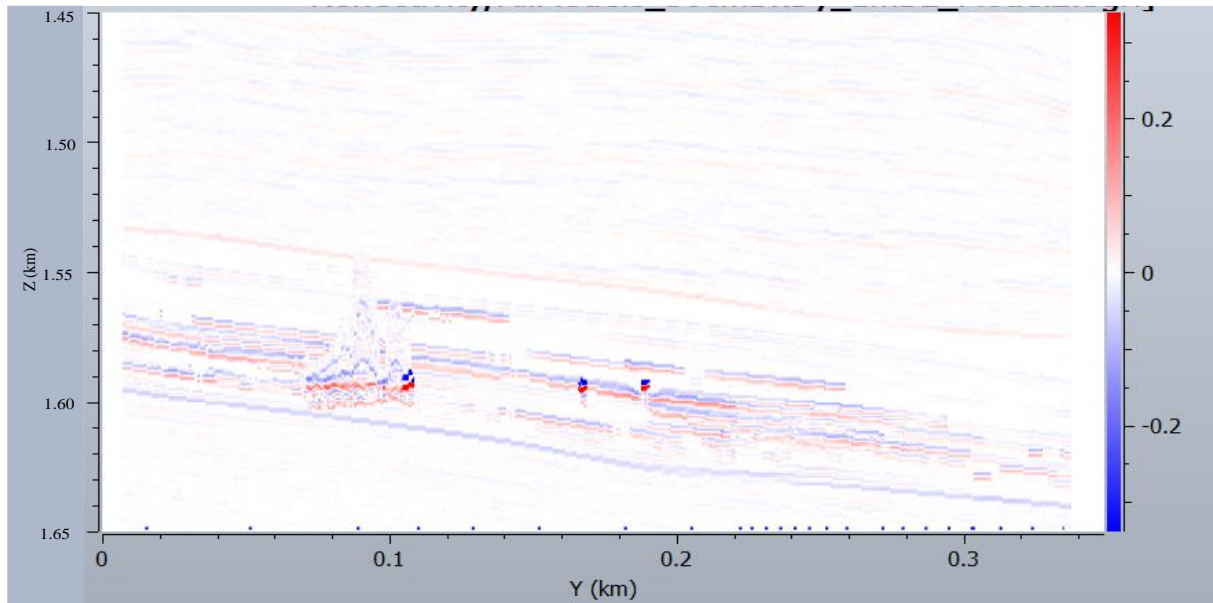
Figure 5.1.2-3 reflectivity of Model 2 in vertical (YZ) direction at X = 0.109 km. The open cavern shows the highest reflectivity among the reflectors.

5.1.3. Model 3

As model 2, the velocities of P- and S-waves and density were calculated by Raymer Hunt Gardner model (see Eq. 4.2, 4.3 & 4.5). Model 2 consisted of only one lithology for the host rock which is dolomite. No effect of changing lithology was included. In model 3, the effect of overburden with vertical changes in lithology is introduced (Figure 5.1.3-1). The lithology above the PT unconformity consists of Triassic shales whereas below the unconformity the property of dolomite is used to estimate the velocities and density from the empirical relationship (see Eq. 4.2 4.3 & 4.5). The reservoir is dolomite with 100 % oil saturation (Figure 5.1.3-2., Figure 5.1.3-3).
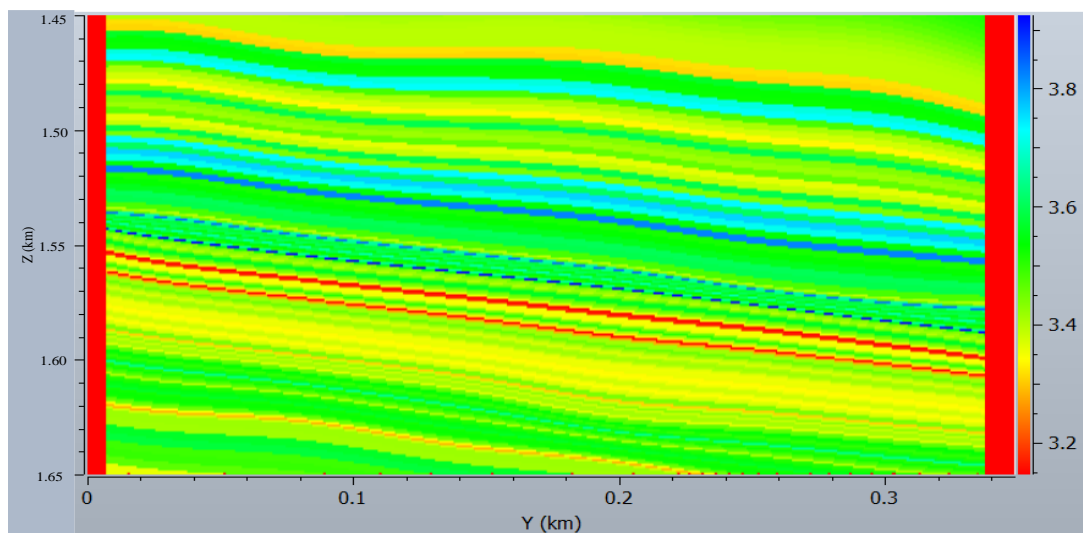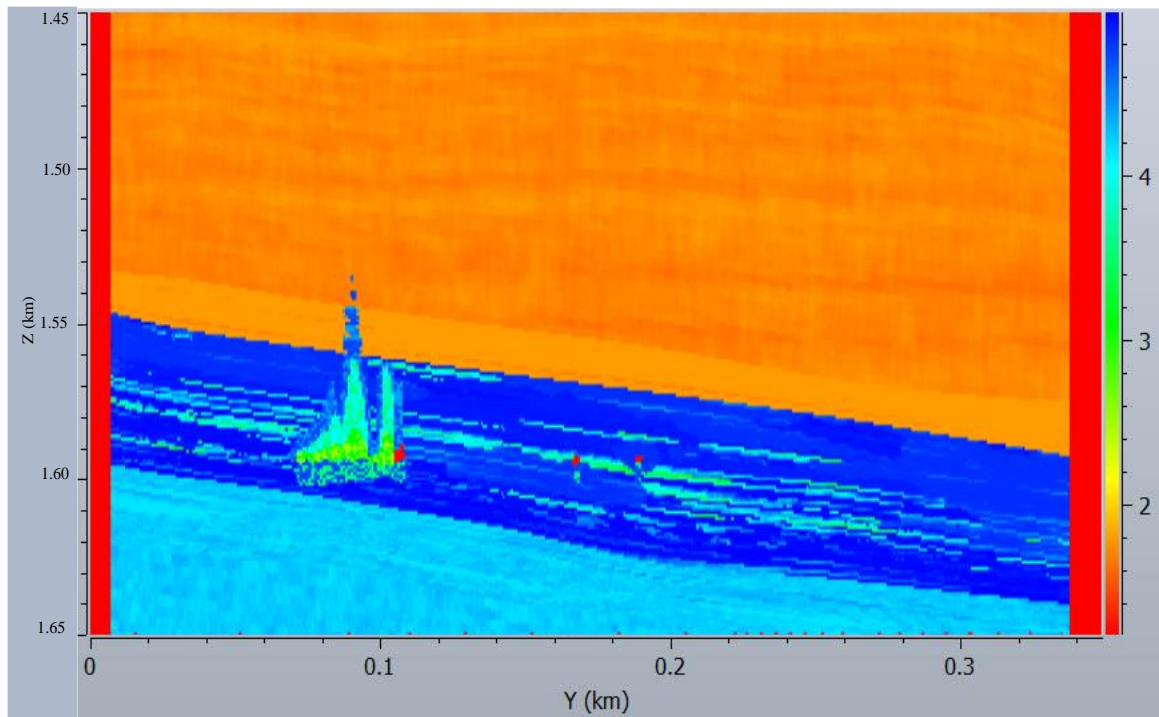
Figure 5.1.3-1 Geological model of model 3 represented by Vp(km/s) in vertical (YZ) direction at X = 0.109 km
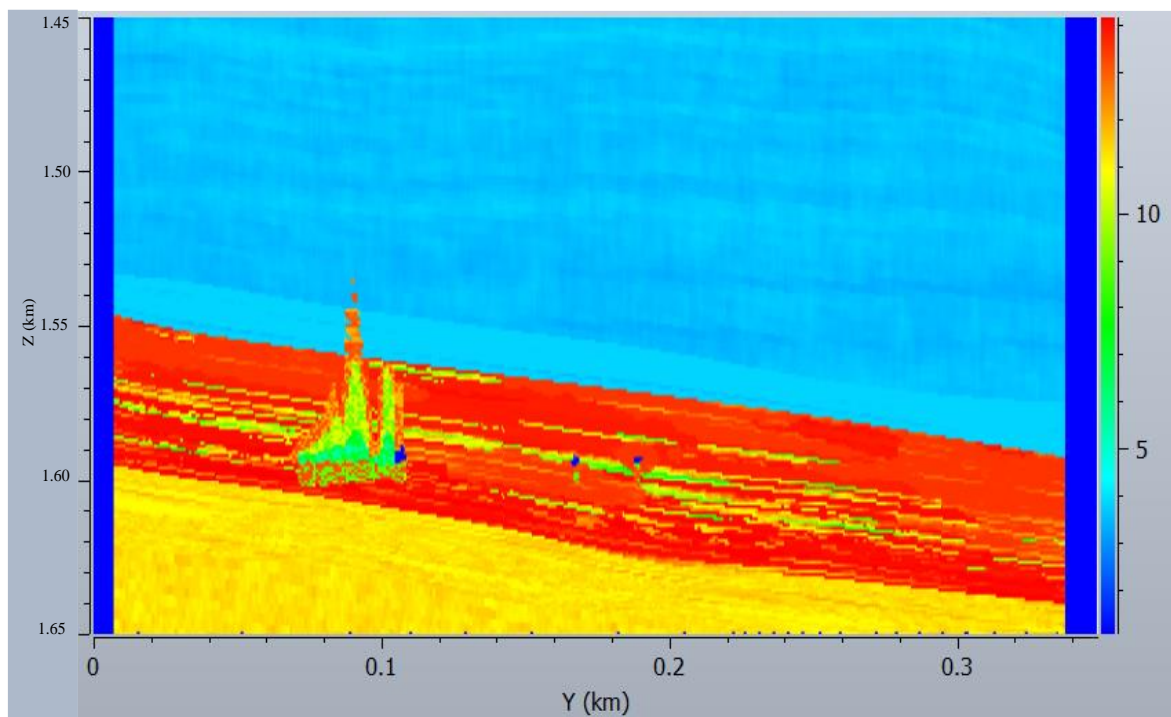
Figure 5.1.3-2 The P Impedance of model 3 in vertical (YZ) direction at X = 0.109 km. The effect of lithology change can be seen as the transition from triassic shales to permian dolomite.
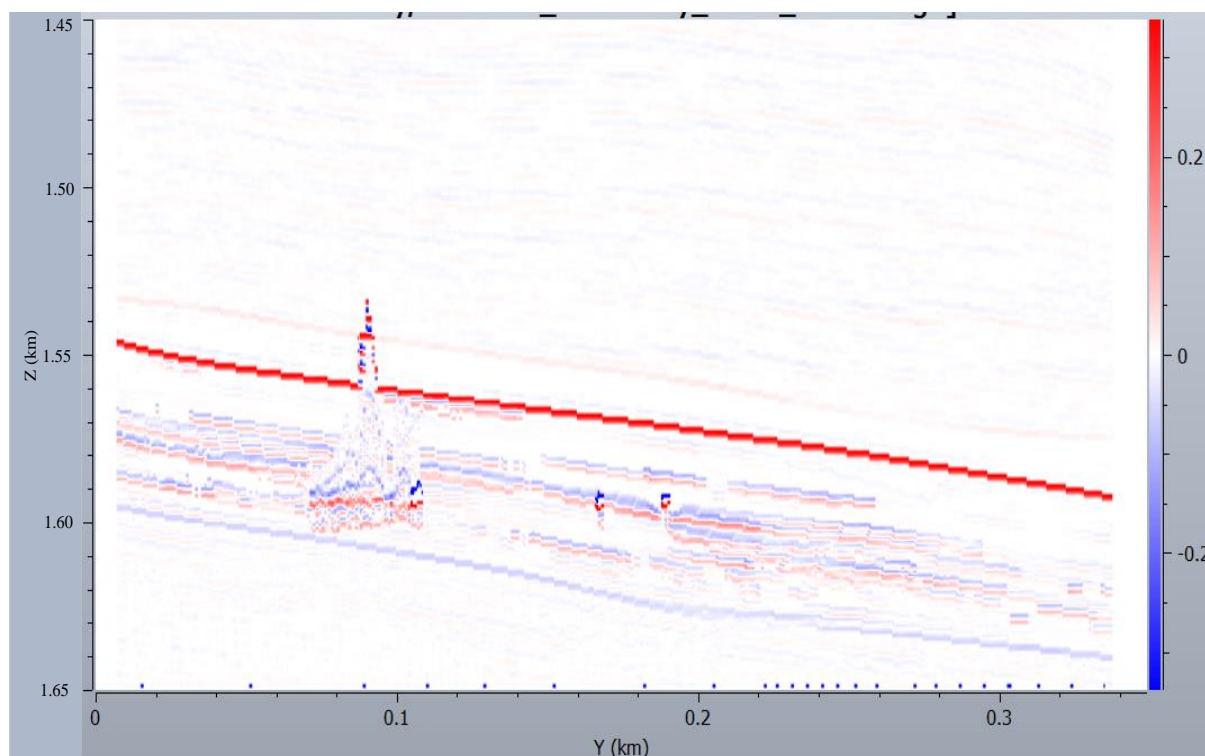
Figure 5.1.3-3 The reflectivity of model 3 vertical (YZ) direction at X = 0.109 km. The effect of paleokarst is clear along with the changing lithology.

5.1.4. Model 4

As the effects of single versus changing host-rock lithology on paleokarst imaging were accounted for in models 3 and, the effect of fluid saturation is tested within the reservoir in that last model (Figure 5.1.4-1). Lithology is considered as 100% dolomite, while the fluid saturations are 70 % oil and 30 % water. The estimation of velocities and density are based on the earlier-mentioned empirical formulas (Eq. 4.2, 4.3 & 4.5), thus having both the effect of lithology and different saturations in the pore system (Figure 5.1.4-2, Figure 5.1.4-3).
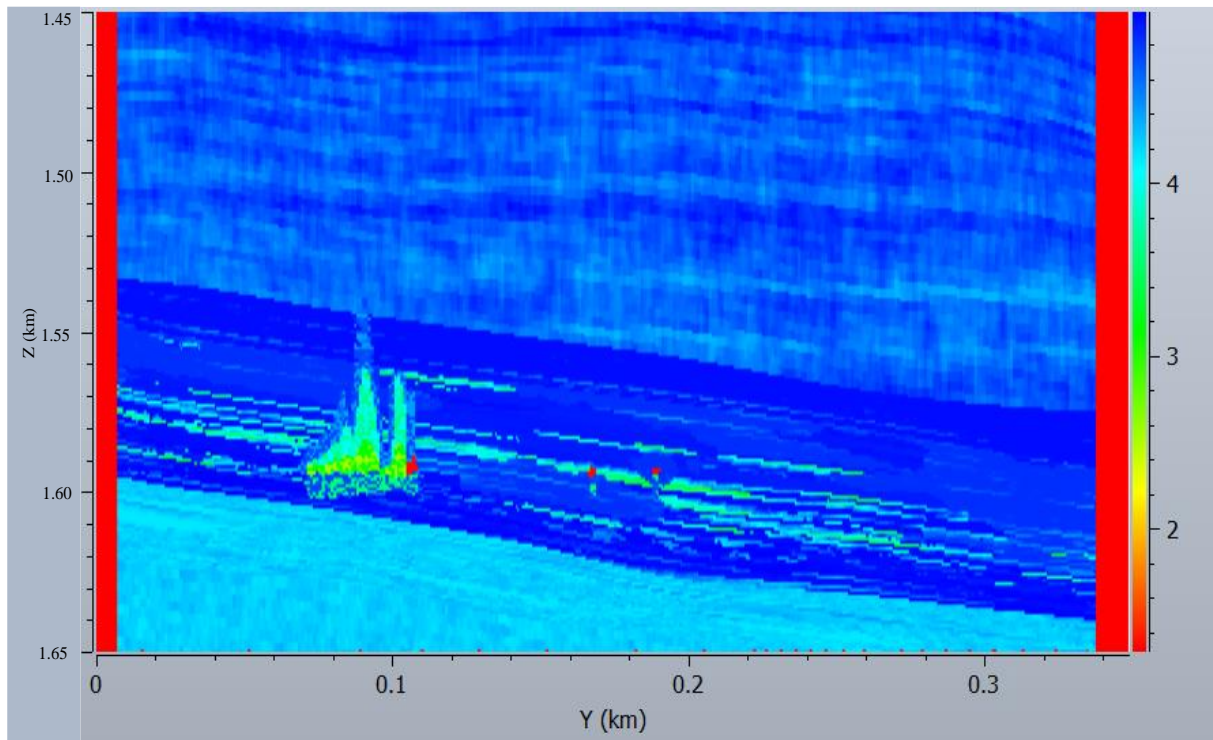
Figure 5.1.4-1 Geological model of Model-4 represented by Vp (km/s) in vertical (YZ) direction at X = 0.109 km
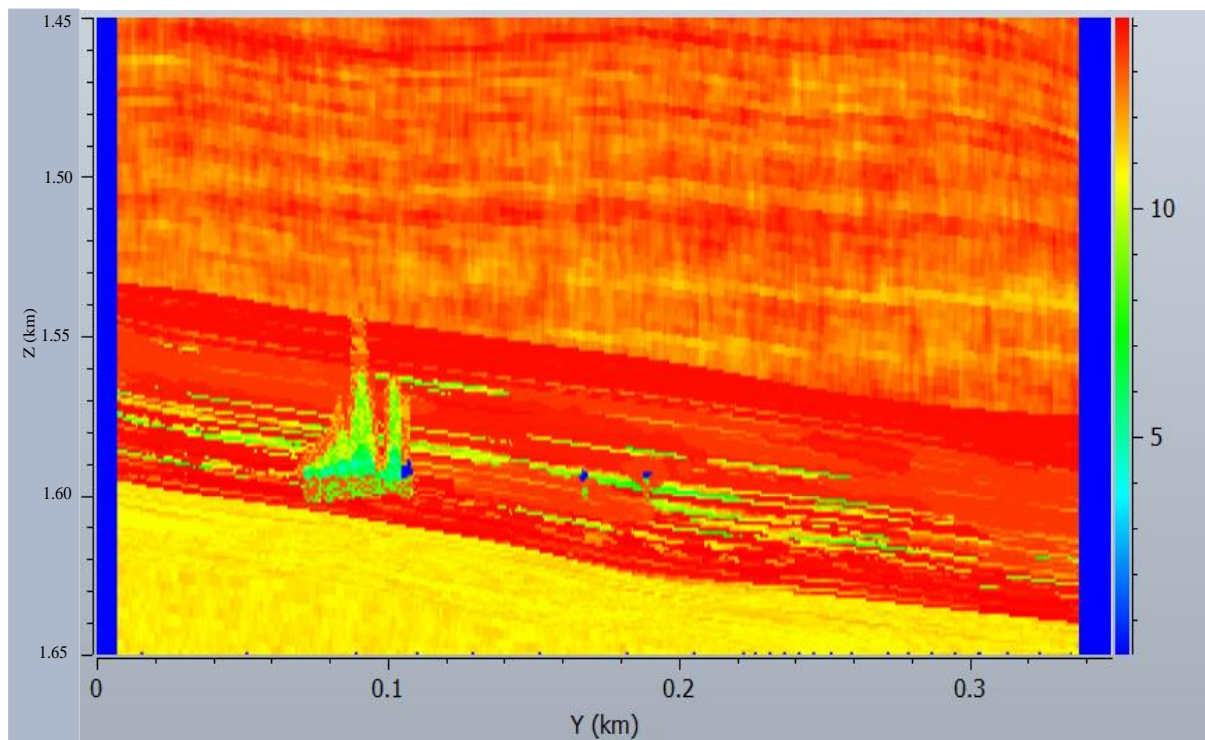
Figure 5.1.4-2 The P Impedance of Model-4 in vertical (YZ) direction at X = 0.109 km. The values of P Impedance increased which will play crucial role in seismic response.
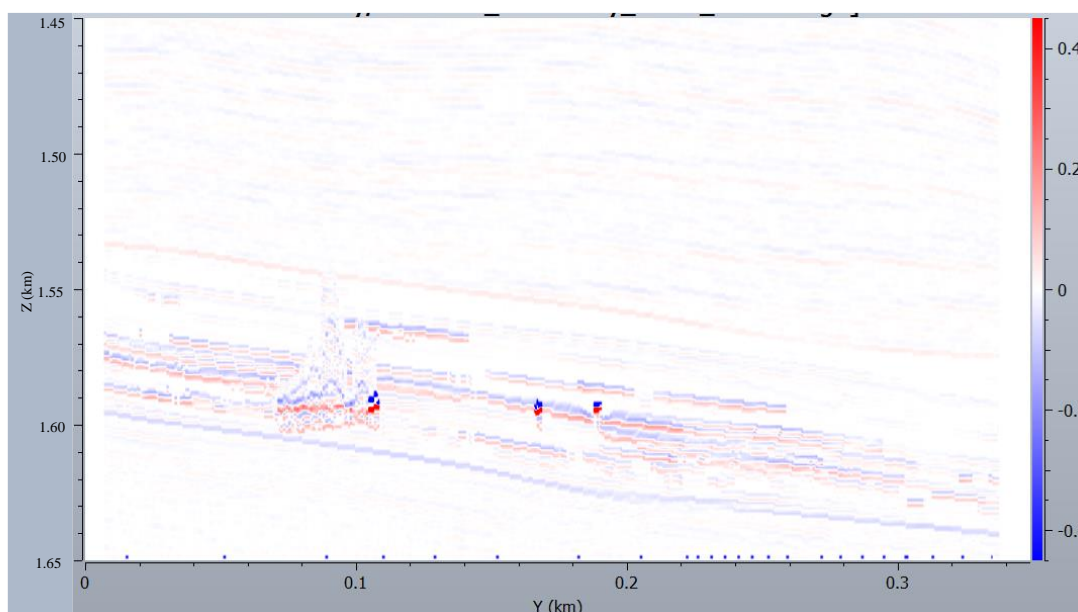
Figure 5.1.4-3 shows the reflectivity of Model 4 in vertical (YZ) direction at X = 0.109 km. The reflectivity response increased in open caverns due to fluid saturation variation.

The reflectivity of these four models was then convolved with either the sole wavelet to get results like these obtained by standard 1D convolution, or with a PSF (which includes the same wavelet as for 1D convolution, while adding the full 3D resolution and limited-illumination effects). In output, 3D seismic-modelled cubes of PSDM-type are produced. The input elastic properties for all models can be seen in the appendices A, B, C, and D.

5.2. Background Model

The background model is the simplistic model in which all the properties were populated on the base of Alta-3 well (Appendix E). The data is a single point extrapolated in the whole model which is why it gives a layer cake representation of the subsurface with constant properties in each layer. The tricky part with this model is that the host-rock and paleokarst properties are mixed, making it difficult for reader to identify where paleokarst features are present. The sampling of the data is based on 50 cm in X and Y direction whereas in the Z direction 1m sampling is used for all models.

The wavelets which were used to generate the PSF were of Ricker (Ryan 1994) type with dominant frequencies of 30, 45, and 60 Hz (Figure 5.2-1). First, the 30-Hz Ricker wavelet was used to better match the actual seismic data where the dominant frequency ranges between 25 and 30 Hz. The 45- and 60-Hz Ricker were used to assess and determine that paleokarst features are sensitive to which frequency and also to have better definition of the

reflectors. Table 5.2-1 shows the properties selected to generate a PSF including the before-mentioned wavelets (Figure 5.2-2).
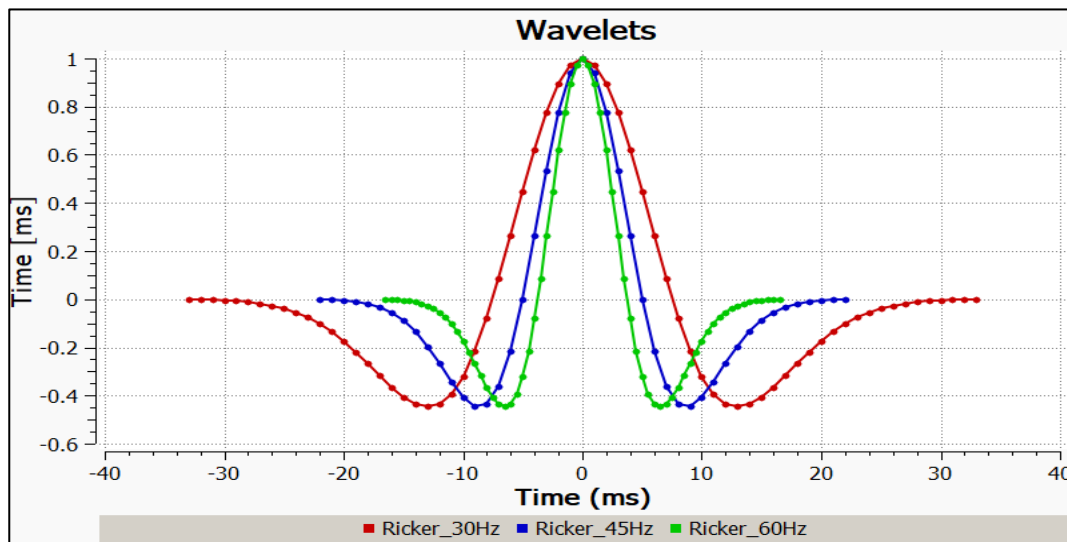
Figure 5.2-1 Representation of three wavelets chosen for the seismic modelling on Model-1

Table 5.2-1 Data properties required to generate the PSF from the wavelet.

Maximum illuminated reflector dip	45°
Average velocity in target model	3.5 km/s
Incident angle	0°
Wavelet – dominant frequency	30, 45 and 60 Hz
Reflection mode	P-P
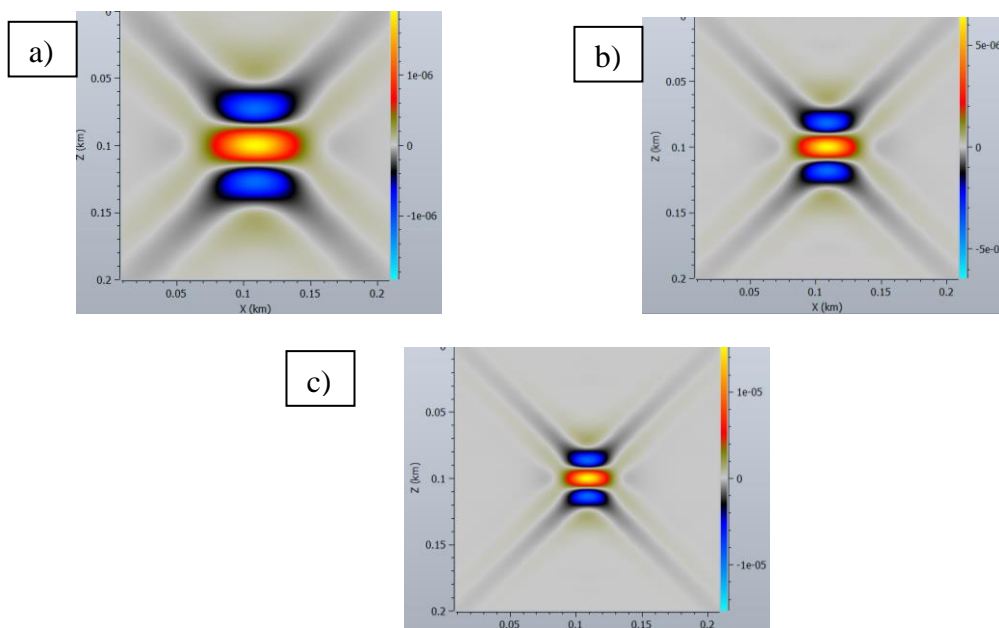
Figure 5.2-2 Illustration of PSF generated for the seismic modelling of model 1 with a) 30-Hz, b) 45-Hz and, c) 60-Hz Ricker wavelet and the parameters of Table 5.2-1

The 3D reflectivity grid illustrated in Figure 5.1.1-3 was then convolved with each of the former PSFs (Figure 5.2-2) yielding the 3D synthetic seismic (Figure 5.2-3). The comparison of the three synthetic seismic data shows, as expected, that the 30-Hz data is low-resolution and missing the details of the thin layering. The 45- and 60-Hz modelled data are similar to each other, though 60-Hz section has a better match with the reflectivity input, thin layers being better resolved, again as expected and resolving thin layers.

Based on the above observations, seismic modelling of models 2, 3, and 4 will be carried out using 30- and 60-Hz cases as two end members for comparison. The 30-Hz data will thus be representative of a low-resolution case closer to the actual seismic. The 60-Hz data will represent, on the other hand, a near best-case scenario for which smaller details might be retrieved, thus possibly helping paleokarst characterization and their quantification for estimation of area and volumes. The polarity convention will be SEG normal polarity where positive amplitudes represent peak and negative amplitudes represent trough.
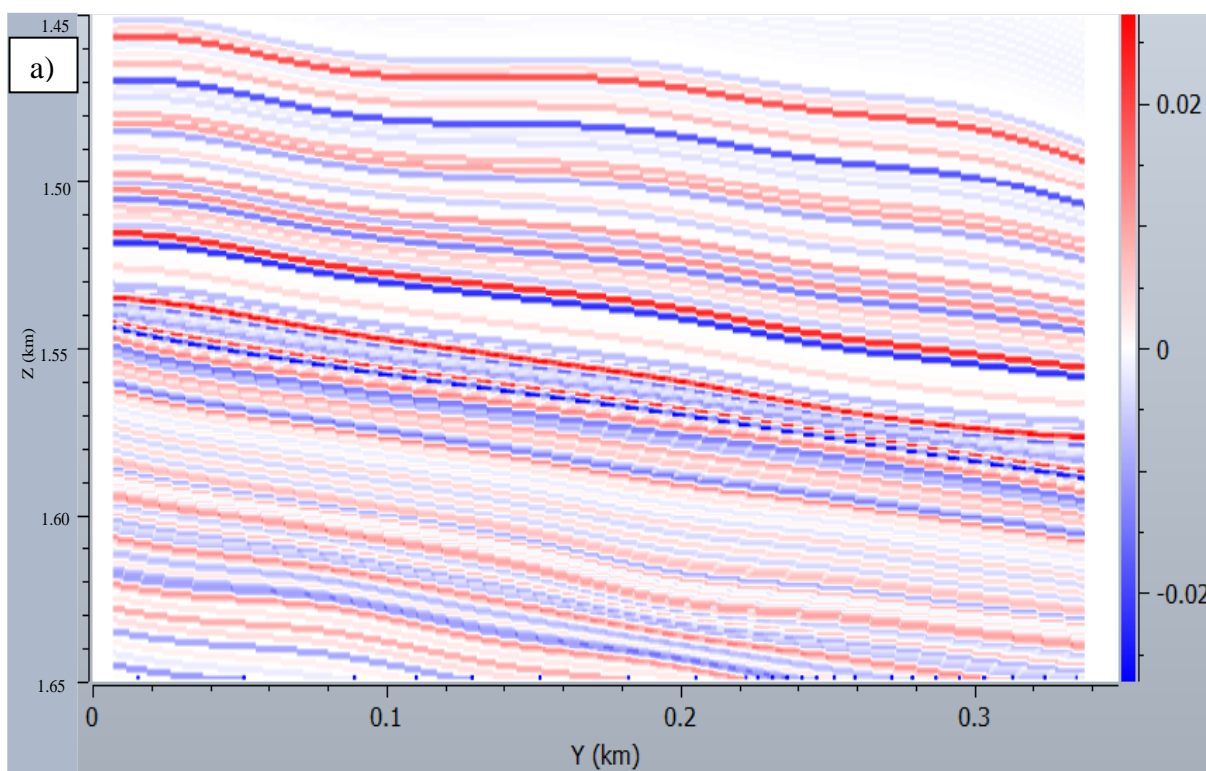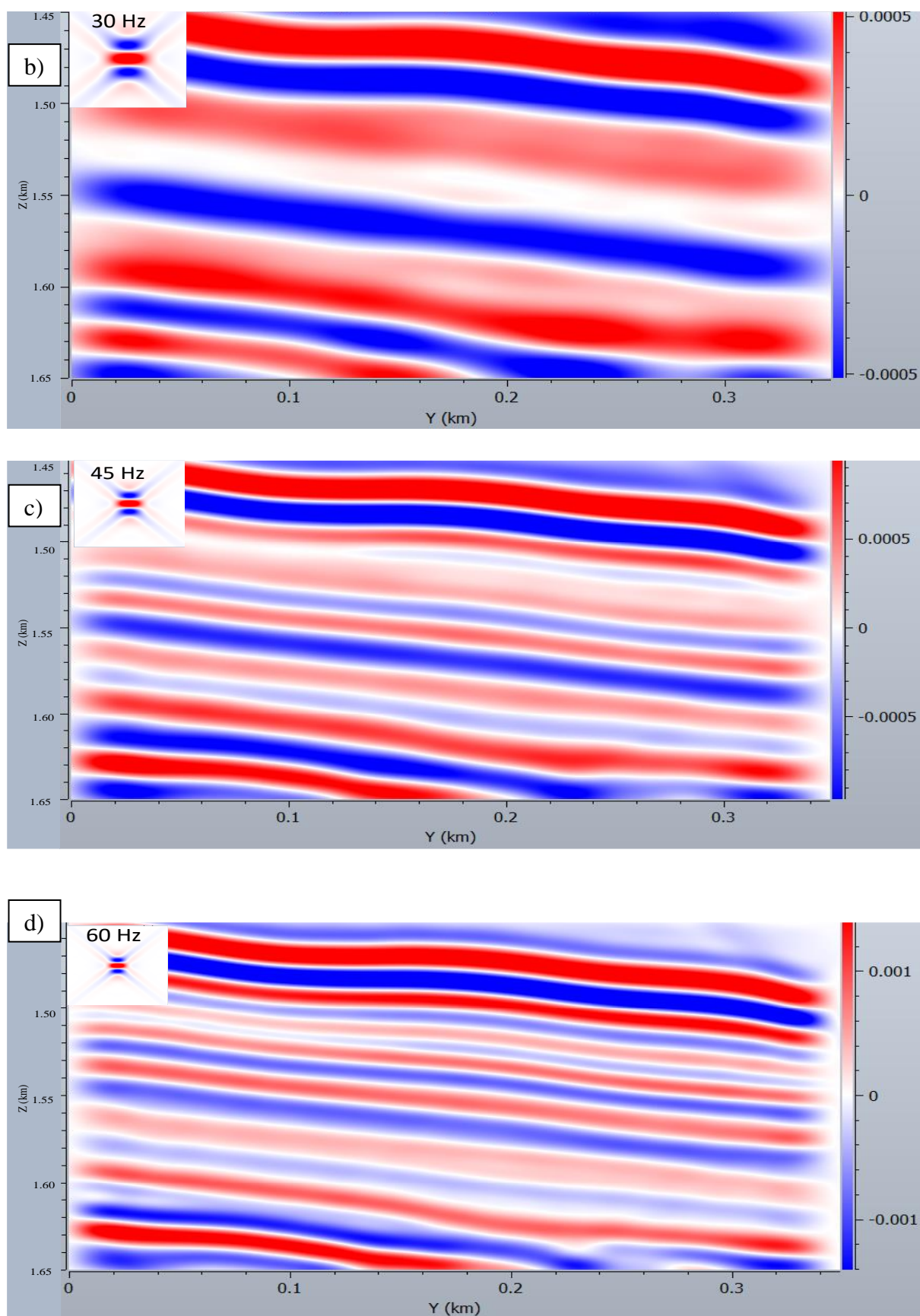
Figure 5.2-3 The output synthetic seismic data of model-1after convolution of PSF with reflectivity a) Geological model represented with reflectivity: synthetic seismic for b) 30 Hz c) 45 Hz d) 60 Hz in vertical (YZ) direction at X = 0.109 km. The corresponding PSF are superimposed

5.3. 1D convolutional – frequency effect

1D-convolution modelling applied on models 2, 3, and 4 was first performed with the two selected Ricker wavelets of dominant frequencies 30- and 60-Hz (refer to 5.2). In 1D convolution, each trace of the model is convolved separately with the selected wavelet, the output (seismic) traces being displayed side-by-side to simulate 2D or 3D data (see 3.6). However, the results of 1D convolution do not provide an accurate picture of the subsurface as imaged per seismic (Grimstad 2018). It can give a first approximation of such seismic images, partially accounting for the vertical resolution effect due to frequency content of the wavelet, but it does not account for, e.g., lateral resolution and limited-illumination effects.

The parameters needed for 1D convolution include the average P-wave velocity in the target (4.5 km/s), a wavelet, and the reflectivity model. The comparison of the 30- and 60-Hz cases for models 2, 3, and 4 suggests that the paleokarst features are represented as high amplitude anomalies with smearing effect vertically and laterally-constrained which makes them easier to identify (Figure 5.3-1).
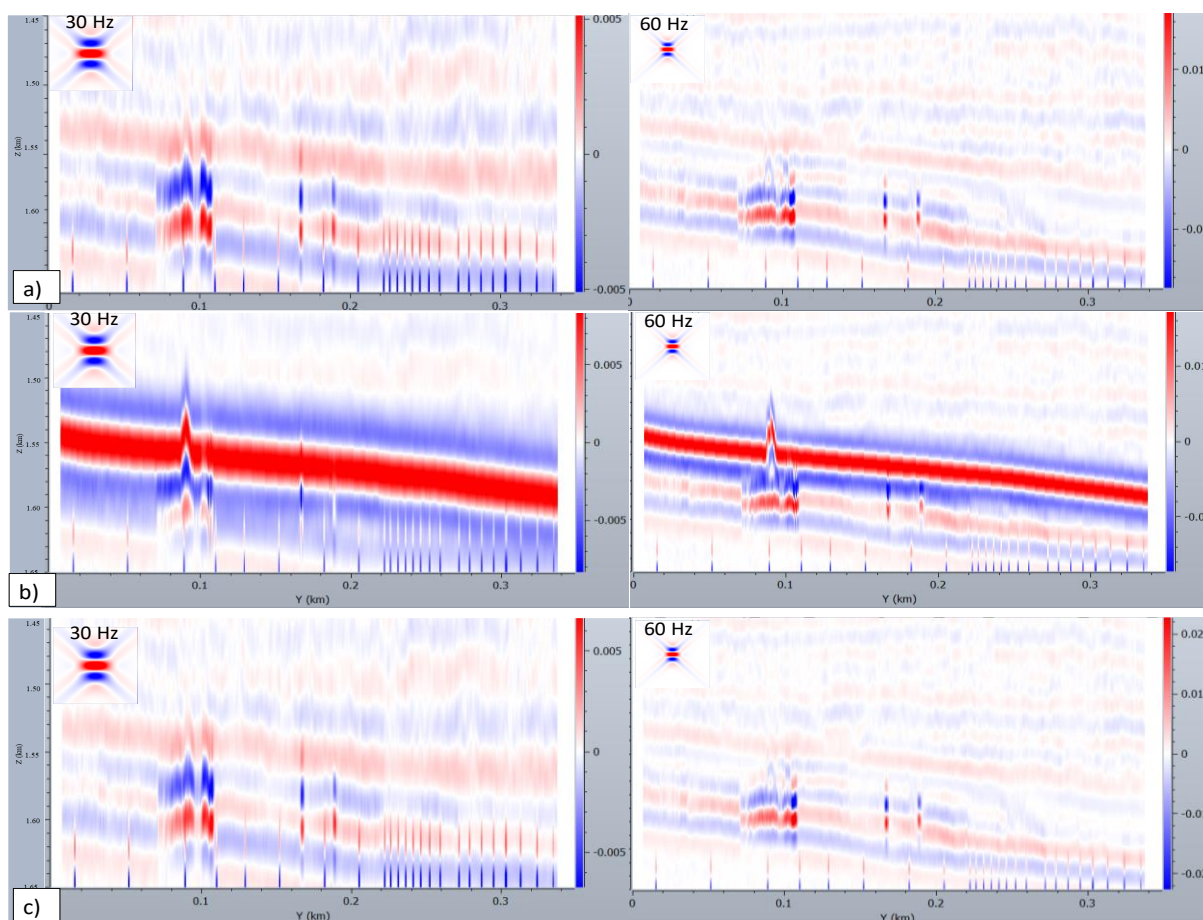
Figure 5.3-1 1D Convolution with 30 and 40 PSF in YZ direction. a) Shows Model-2 case b) shows Model-3 case and c) shows Model-4 case

5.4. PSF Convolution – frequency effect

As earlier discussed, the resolution of seismic is mainly controlled by the frequency content of the wavelet (bandwidth and shape of spectrum around a possible dominant frequency). Changing the frequency content will thus change the seismic images. In this study, two frequencies 30 and 60 Hz were used to see the effect of bandwidth on output result. Still using the two dominant frequencies of 30- and 60-Hz for Ricker wavelet as discussed in 5.3, a PSF convolution is now applied. The parameters used to generate the PSF are shown in Table 5.4-1. In this section, only results of Model-2 are shown, results for model 3 and 4 will be shown in later sub chapters.

Table 5.4-1 The properties used for models 2, 3 and 4 by changing the frequency of PSF.

Maximum illuminated reflector dip	45°
Average velocity in target model	4.5 km/s
Incident angle	0°
Reflection mode	P-P

The results with the 30-Hz wavelet show broad seismic reflectors through which it is very difficult to identify the karst system (Figure 5.4-1 b). High amplitudes are seen at the location of the karst system and in its surroundings making it difficult to separate them.

Increasing the frequency to 60-Hz improve both vertical and lateral resolution of the seismic data, where the paleokarst can now be differentiated from the surrounding area by locally high amplitudes (Figure 5.4-1 c). However, even though a high amplitude anomaly helps identifying the main paleokarst body (detection), its actual shape and size of the paleokarst cannot be determined with certainty, being still partially unresolved (Figure 5.4-2).
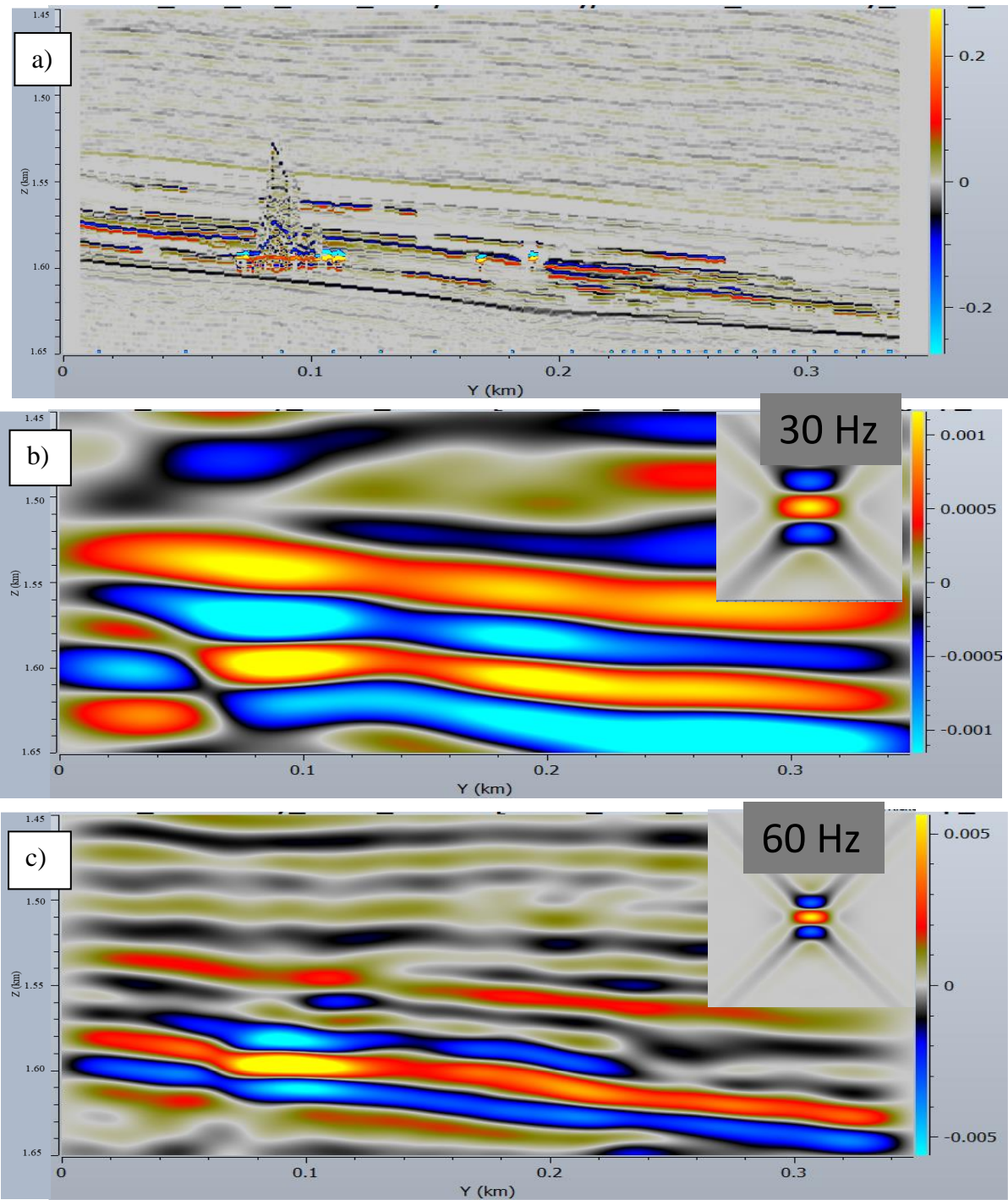
Figure 5.4-1 PSF-convolution Model-2 impact of the dominant frequency of the wavelet in vertical (YZ) direction at X = 0.1055 km a) reflectivity input; seismic results with b) 30-Hz c) 60-Hz wavelets, respectively
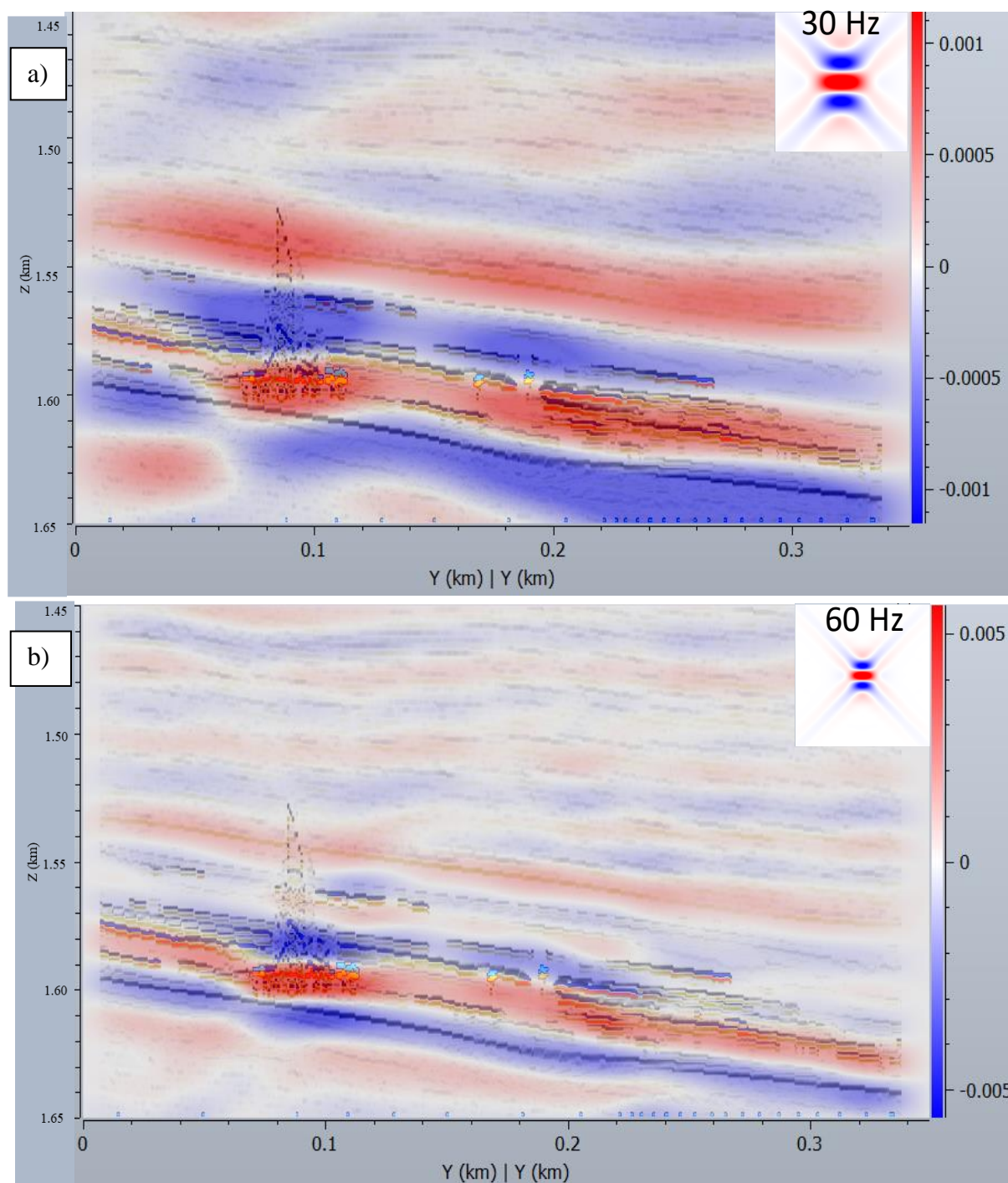
Figure 5.4-2 PSF-convolution Model 2 impact of the dominant frequency of the wavelet, the superposition of reflectivity and synthetic modelled seismic in vertical (YZ) direction.at X = 0.1055 km; seismic results with a) 30-Hz b) 60-Hz, wavelet respectively..

5.5. PSF convolution - illumination effect

The maximum illumination angle is the parameter that constrains whether the steepest reflectors are imaged or not (Lecomte et al., 2015). The maximum illumination angles used in this study are 45°, as a proxy for standard 3D PSDM results, and 90°, corresponding to a perfect illumination (all reflector dips are imaged, seldom achieved). Note that this parameter also influences the lateral resolution, which will be about half-a-wavelength for the 45° illumination (Simm and Bacon, 2014) and a quarter-of-a-wavelength for the perfect illumination.

 The 45°-illumination case results in a more blurred seismic image, due to the decrease in lateral resolution, which thus increases the size of the high amplitude response in comparison to the – theoretical – perfect-illumination case (Figure 5.5-1 & Figure 5.5-2). This can be seen for both 30- and 60-Hz wavelets. The seismic images generated with perfect illumination results are better resolved, the shape of the paleokarst being better constrained (Figure 5.5-2). The lateral resolution is better than the 45° case. Comparing the results of 30 and 60 Hz shows that karsts are better resolved in the 60 Hz perfect illumination case (Figure 5.5-3).
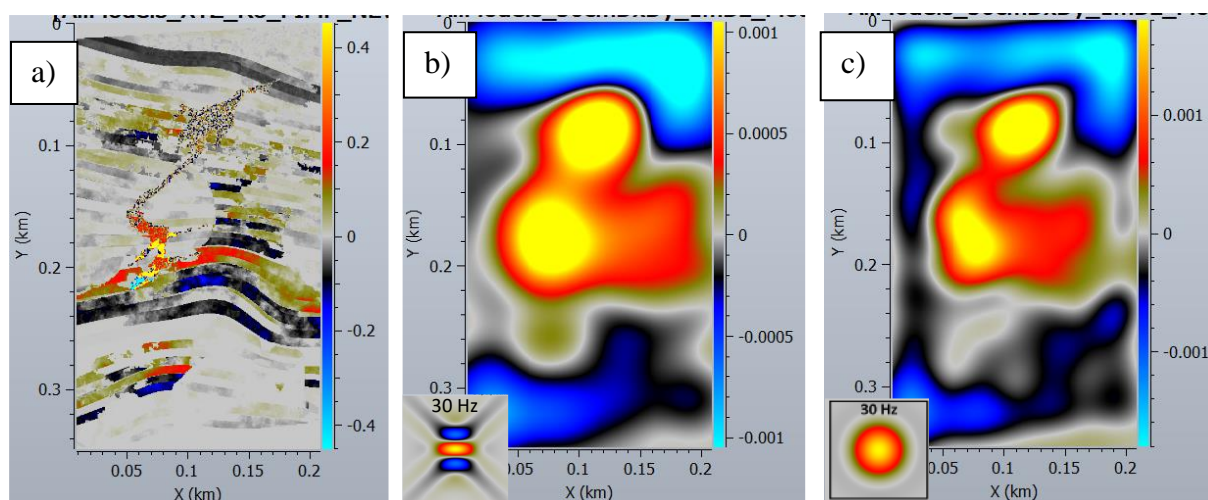
Figure 5.5-1 PSF-convolution Model 4 effect of changing the illumination angle 30 Hz PSF in horizontal (XY) direction at 1600 m depth a) reflectivity input; seismic results with b) 45° c) 90°, illumination angle respectively
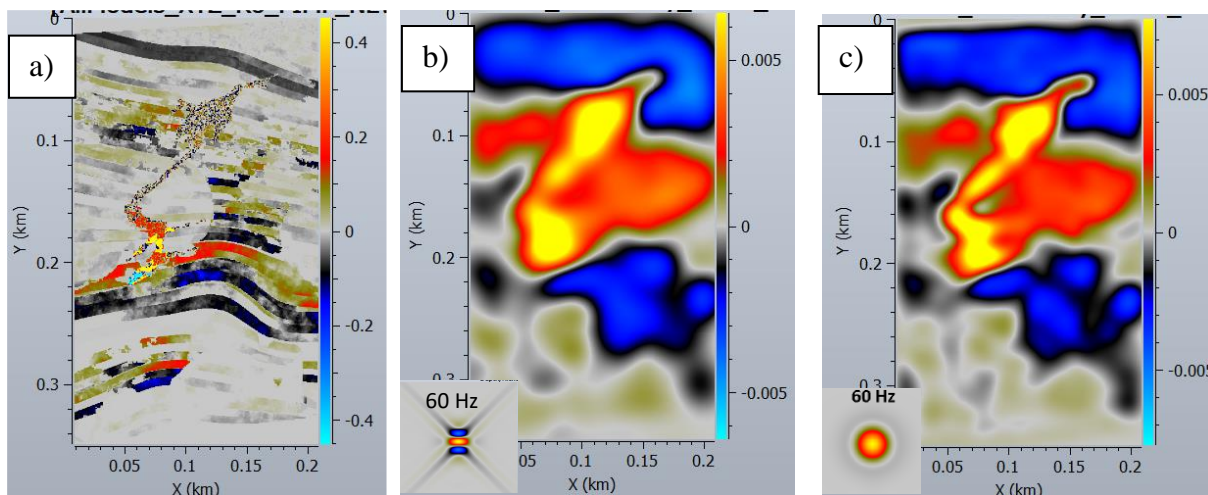
Figure 5.5-2 PSF-convolution Model 4 effect of changing the illumination angle 60 Hz PSF in horizontal (XY) direction at 1600 m depth a) reflectivity input; seismic results with b) 45°c) 90°, illumination angle respectively
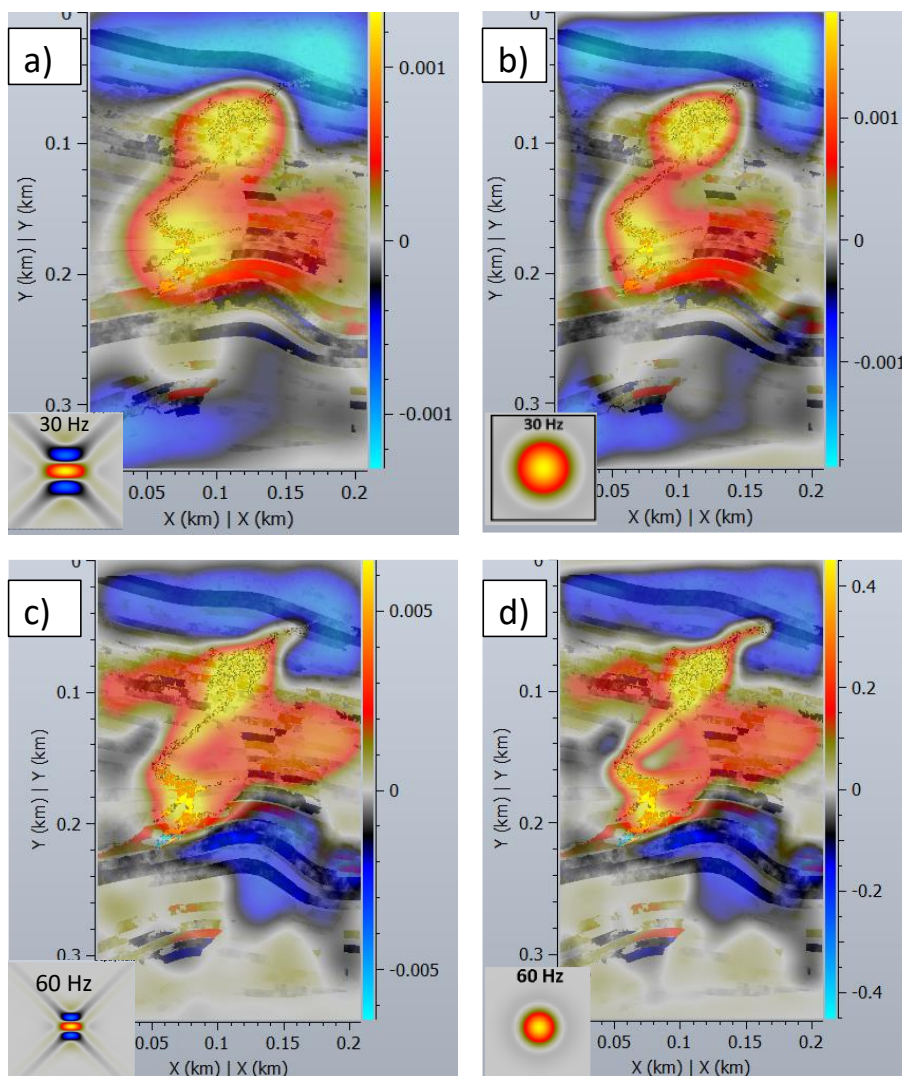
Figure 5.5-3 PSF-convolution Model 4 effect of changing the illumination angle, superposition of reflectivity and synthetic modelled seismic in horizontal (YZ) direction at 1600 m depth. a) 30-Hz with 45°; b) 30-Hz with 90°; c) 60-Hz with 45°; b) 60-Hz with 90°, illumination angle respectively.

5.6. PSF convolution – overburden effect

As discussed earlier (see chapter 5.1.3) the effect of different lithologies was introduced in model 3. The reservoir was considered as dolomite, whereas, above the unconformity, the Triassic shales were introduced to account for the effect of overburden, in turn replicating close to real conditions. In model-2, the whole host-rock is considered as 100% dolomite. Modeled seismic was generated for both models, with 30- and 60-Hz dominant frequency, and with a maximum illumination angle of $45°$ (Figure 5.6-1).

The paleokarst features are not identifiable for the 30-Hz case in model-2, whereas they can be detected for the 60-Hz case based on high amplitudes. The presence of high impedance contrast between shale and dolomite creates a challenging condition for the detection of paleokarst in seismic data. It can be seen in both 30- and 60-Hz cases that identification of the paleokarst is impossible as high amplitudes of PT unconformity reflectors mask the signature of karst facies making it very challenging to interpret the paleokarst (Figure 5.6-1).
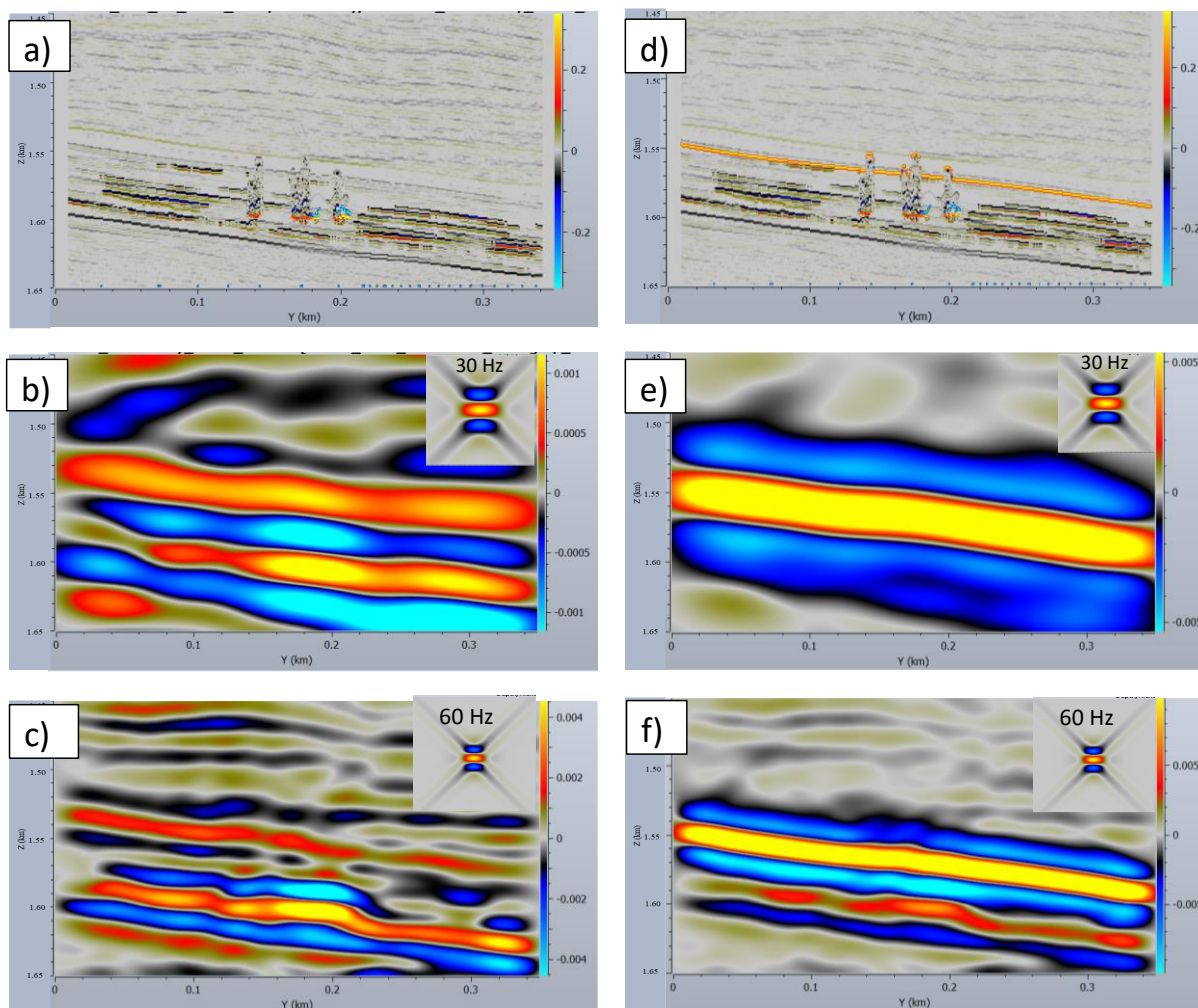
Figure 5.6-1 PSF-convolution Model 2 & 3 effect of overburden in vertical (XZ) direction at Y = 0.072 km, a) imput reflectivity for model 2; modelled seismic results b) 30-Hz, c) 60-Hz, wavelets respectively. d) input reflectivity for model 3; modelled seismic results e) 30-Hz, f) 60-Hz, wavelets respectively

5.7. PSF convolution - fluid saturation effect

The next parameter which was changed to see its effect on seismic data is the fluid saturation, it was incorporated into the geological model by calculating velocity and density for different saturations in model 4 compared to model 2. Both model 2 and model 4 consist of 100% dolomite host-rock, Model 2 having 100% oil saturation, while model-4 has 70% oil saturation and 30% water saturation. The modelled seismic results are shown in Figure 5.7-1.

Both 30- and 60-Hz cases were run for both models to see the effect of amplitude change. As described earlier (refer to 5.6) it is difficult to see the paleokarst features for a 30-Hz case, which is also the case here for both Model-2 and Model-4. The 60-Hz case is – again as expected - better at resolving the paleokarst in the form of high amplitude anomalies. The

change in velocity and density due to saturation change is very small, thus no significant change in result of both models can be seen, suggesting saturation change is not producing any significant effect on the results.
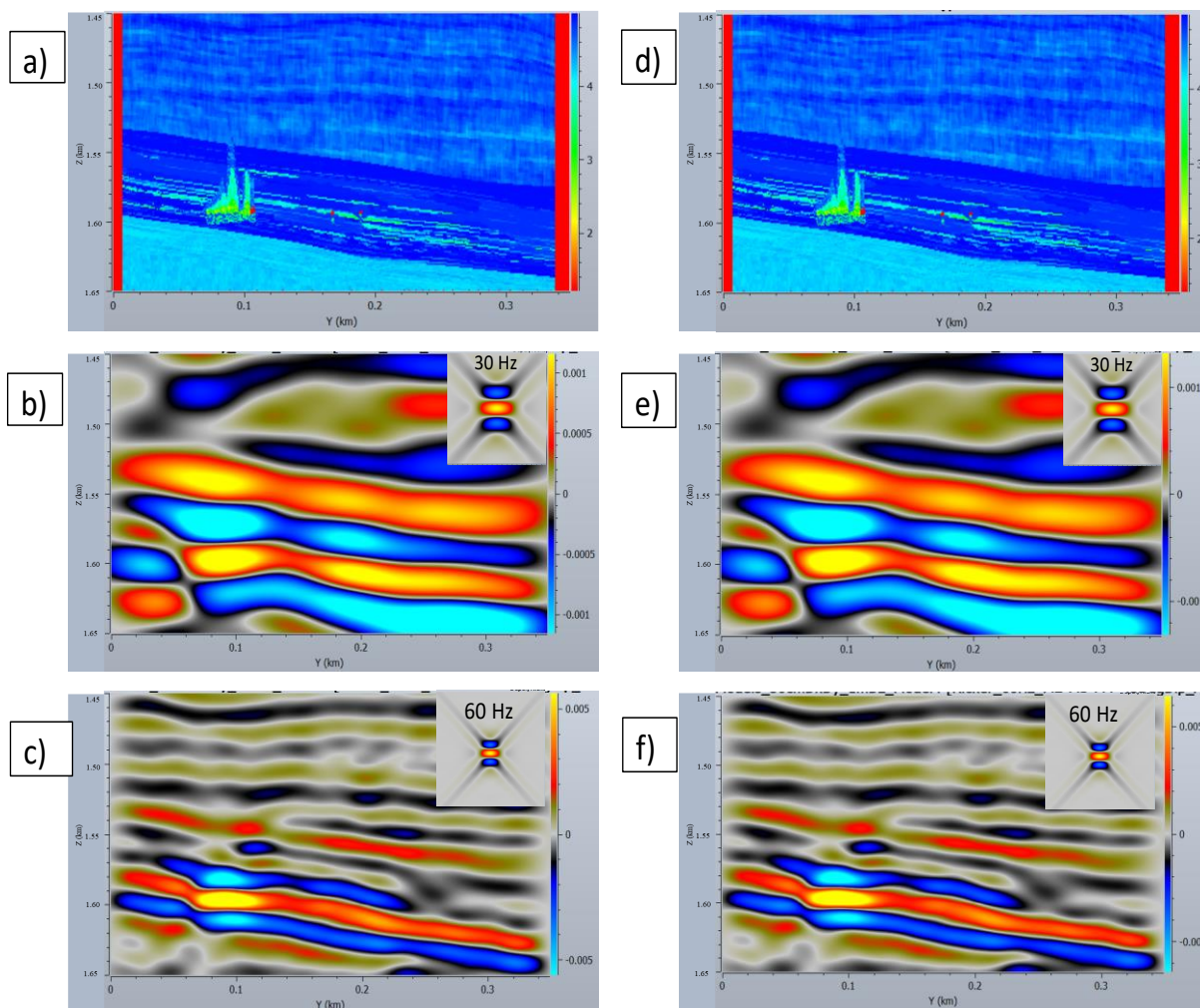
Figure 5.7-1 PSF-convolution Model 2 & 4 effect of fluid saturation in vertical (YZ) direction at X = 0.109 km, a) imput reflectivity for model 2; modelled seismic results b) 30-Hz, c) 60-Hz, wavelets respectively. d) input reflectivity for model 4; modelled seismic results e) 30-Hz, f) 60-Hz, wavelets respectively

Chapter 6

6. Discussion

The study aimed at developing a seismic modelling workflow applied geomodels derived from Loppa High using well and seismic data, this for a better understanding and analyses of seismic signature of paleokarst reservoirs. The results were shown in Chapter-5; in the present chapter, the evaluation and synthesis of the result will be provided. First, seismic detectability and resolution will be discussed for different models; secondly, the effects of changing modelling, lithology, and saturation parameters will be reviewed and discussed, thirdly a comparison of actual and synthetic data will be analyzed; finally, the possible limitation regarding different features will be discussed.

6.1. Seismic detectability and resolution

The major challenge associated with paleokarst reservoirs is their detectability and resolution as they are discontinuous features that may extend to a few meters or ten of meters. The detection of these features in a well cannot help in understanding their lateral extension, therefore, hampering the process of volume estimation and field development. The only way is to detect and – even better - resolve them on seismic data. Several modelling cases based on real scenarios were evaluated.

The seismic resolution calculated for the 30- and 60-HZ cases with the average velocity of 4.5 km/s is 38 m and 18 m, respectively. The most common observations in the results are:

- Paleokarst features are expressed as high-amplitude anomalies on seismic where the amplitude is governed by the (acoustic) impedance contrast (refer to Figure 5.4-1 & Figure 5.4-2). The amplitude anomalies do not represent the original shape and size of the cave system, due to lack of resolution, which means that the estimation of the size from seismic data will either be larger or smaller than the actual cave system in the subsurface (Figure 6.1-1).
- Paleokarst facies which have low porosity close to the host-rock are difficult to resolve as the contrast is not high enough to generate amplitude anomaly.
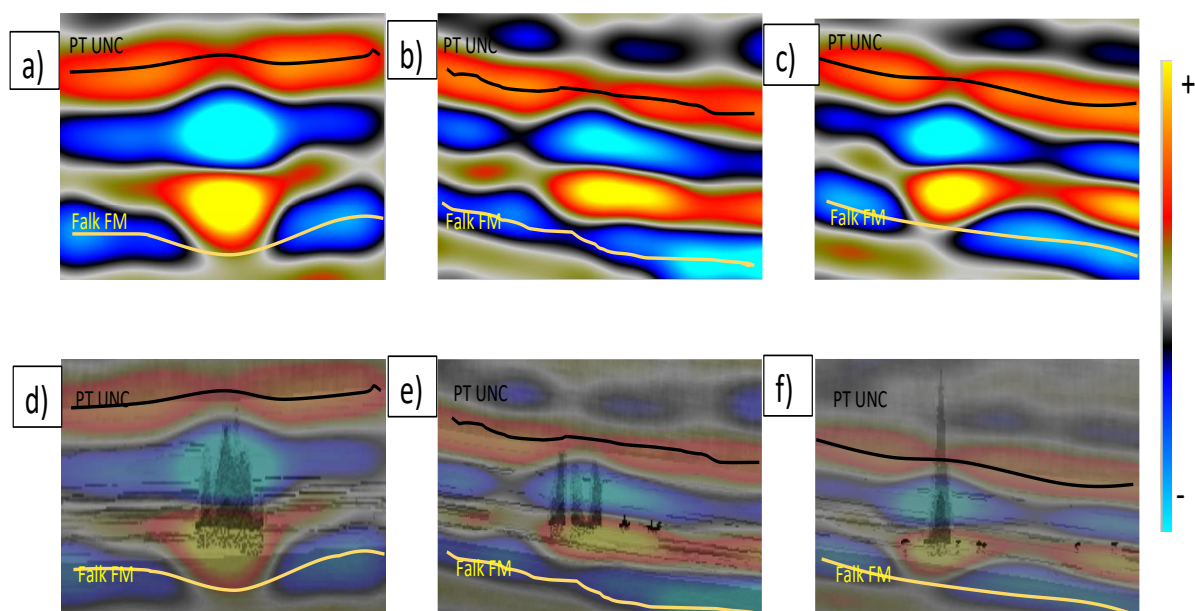
Figure 6.1-1 Detectability and resolution of paleokarsts for model-2 with 60-Hz wavelet. Modelled seismic at a) Y = 0.0805 km, b) X = 0.0635 m c) 0.1005 m; geological model superimposed on modelled seismic at d) Y = 0.0805 km, e) X = 0.0635 m f) 0.1005 m.

- Layers which are less than 10- m thick cannot be resolved for both 30- and 60-Hz cases as they are way below the seismic resolution.

- The open caverns in the paleokarst system which are fluid-filled will affect the seismic results generating bigger higher amplitude anomalies for even smaller areas of caverns (Figure 6.4-3).

- By adding the Triassic shale lithology above dolomite in the geological model greatly reduces the resolution and the detection of paleokarsts becomes very challenging (Figure 6.3-1).

- Changes in the fluid saturation do not affect the overall response of the seismic data for current dataset (Figure 5.7-1).

- Paleokarst features can better be resolved at higher frequencies as lower frequency bands make the anomaly appear bigger than the actual size of the cave system.

The seismic modelling of different models for the karsts system shows that they can be characterized on seismic data if they are above the seismic resolution or in some cases if they are detectable. With depth, the resolution decreases, due to increase of the velocities, while the higher frequencies get more and more absorbed; it will thus be difficult to identify these features at even higher depths. The volume estimation based on seismically marked paleokarsts can give uncertain numbers as the geometries are not truly represented. The caves with higher porosity values are most likely to be better detected/resolved than the ones which

are tightly packed. While planning wells, high-amplitude anomalies should be prioritized, as they can possibly be representative of better paleokarst facies and lead to better results.

6.2. Seismic Modelling Parameters

In Chapter 5, the effects of changing different parameters were shown. The most important parameters are the frequency content of the wavelet (dominant frequency as a proxy of that content for the synthetic Ricker used here; cf. Ryan, 1994) and the maximum-illumination angle. As expected, changing the dominant frequency changes the output response of the seismic. The 60-Hz wavelet has a broader amplitude spectrum than the 30-Hz wavelet but the wavelength response for both is vice versa. Therefore 60-Hz gives a better resolution.

The results of these experiments show that changing the wavelet from 30 to 60 will make the shape of the anomaly more concise and closer to the real geometry of the body (Figure 6.2-1). The amplitude response for both modeled seismic is almost the same. One thing to remember is that real seismic data lacks higher frequency content and therefore identification of paleokarst features becomes more challenging and prone to errors. So, trying to infer the structural behavior of the karst based on seismic is not an easy task.
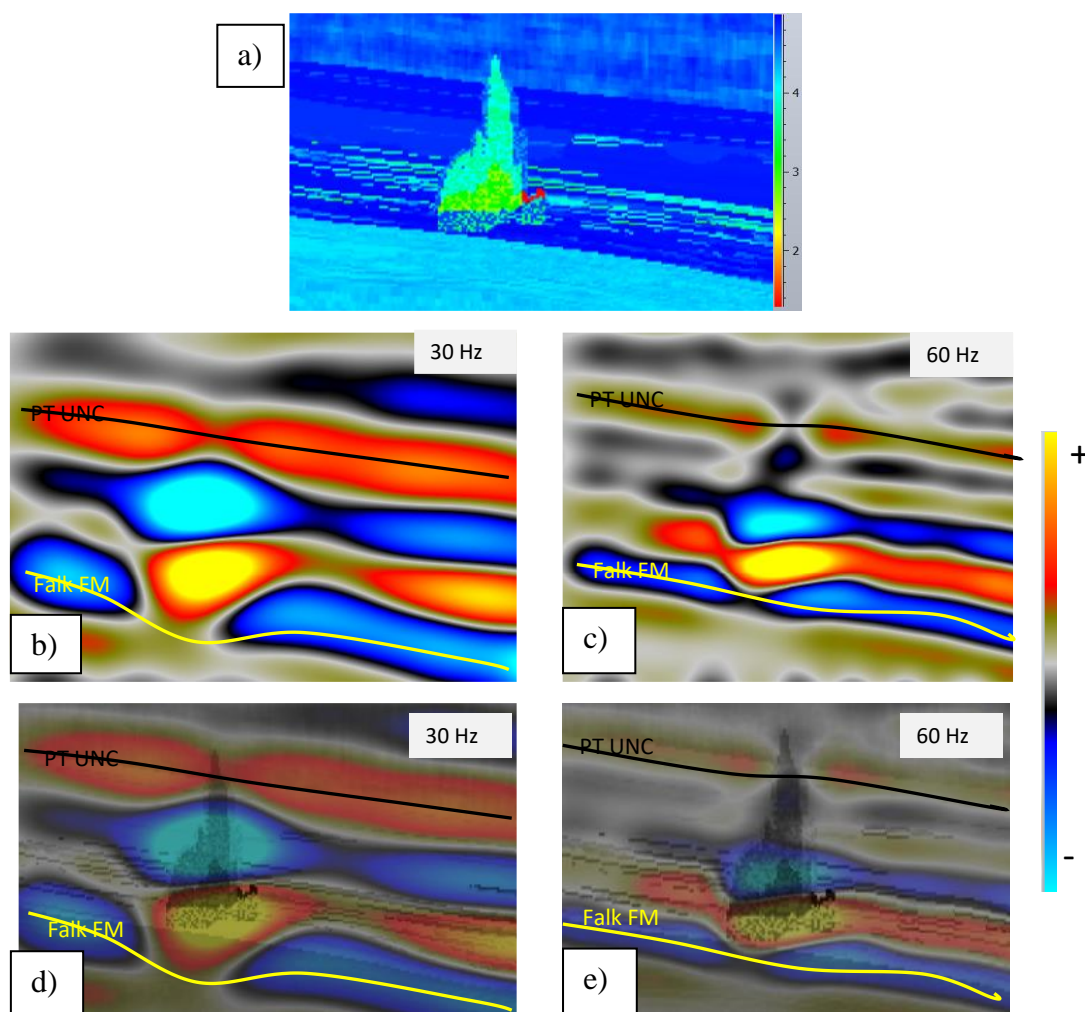
Figure 6.2-1 Shows the response of dominant frequencies on seismic data when frequency changes from 30-Hz to 60-Hz, the definition of paleokarsts get more aligned with actual shape of the structure. The seismic is super imposed on the geological model to have better understanding.

The other important parameter which affects the response of seismic data is the maximum-illumination angle. This is the angle of the dipping reflector which will be illuminated, hence imaged. The modelled seismic data shows that a maximum-illumination angle of 45 ^{o} produces seismic images which are relatively poor in lateral resolution (Figure 5.5-1 & Figure 5.5-2). The anomalies appear bigger than the actual size. On the other hand, perfect illumination, down to vertical dips, produced much better seismic sections depicting close-to-real real geometry of the paleokarst features and relatively good lateral resolution. However, it is important to notice that in real-case scenarios, achieving perfect illumination is impossible because the angle of illumination depends on the velocity model of the overburden above the considered target, in combination with the location and aperture of the seismic survey (Lecomte, 2008).

6.3.Lithology and Fluid Saturation

Lithology and fluid saturation can also affect the seismic response and their sensitivity was also tested and results are shown in chapter five. The effects of overburden were introduced in the geological model by adding Triassic shales above the dolomite reservoir in the Alta field. If the model is homogeneous with only one lithology as host rock the detection of paleokarst features is relatively better than the heterogeneous model. On the other hand, the introduction of shales causes a significant impedance contrast on the boundary of PT Unconformity because of the low velocity and density of shales. This creates a high amplitude reflector above the paleokarst features which masks the signature of karsts (Figure 6.3-1). In the 30-Hz case, no sign of paleokarst can be interpreted as there is no amplitude anomaly whereas in the 60-Hz case, only a small indication of paleokarst is present which is not representative of the actual shape of the cave system.
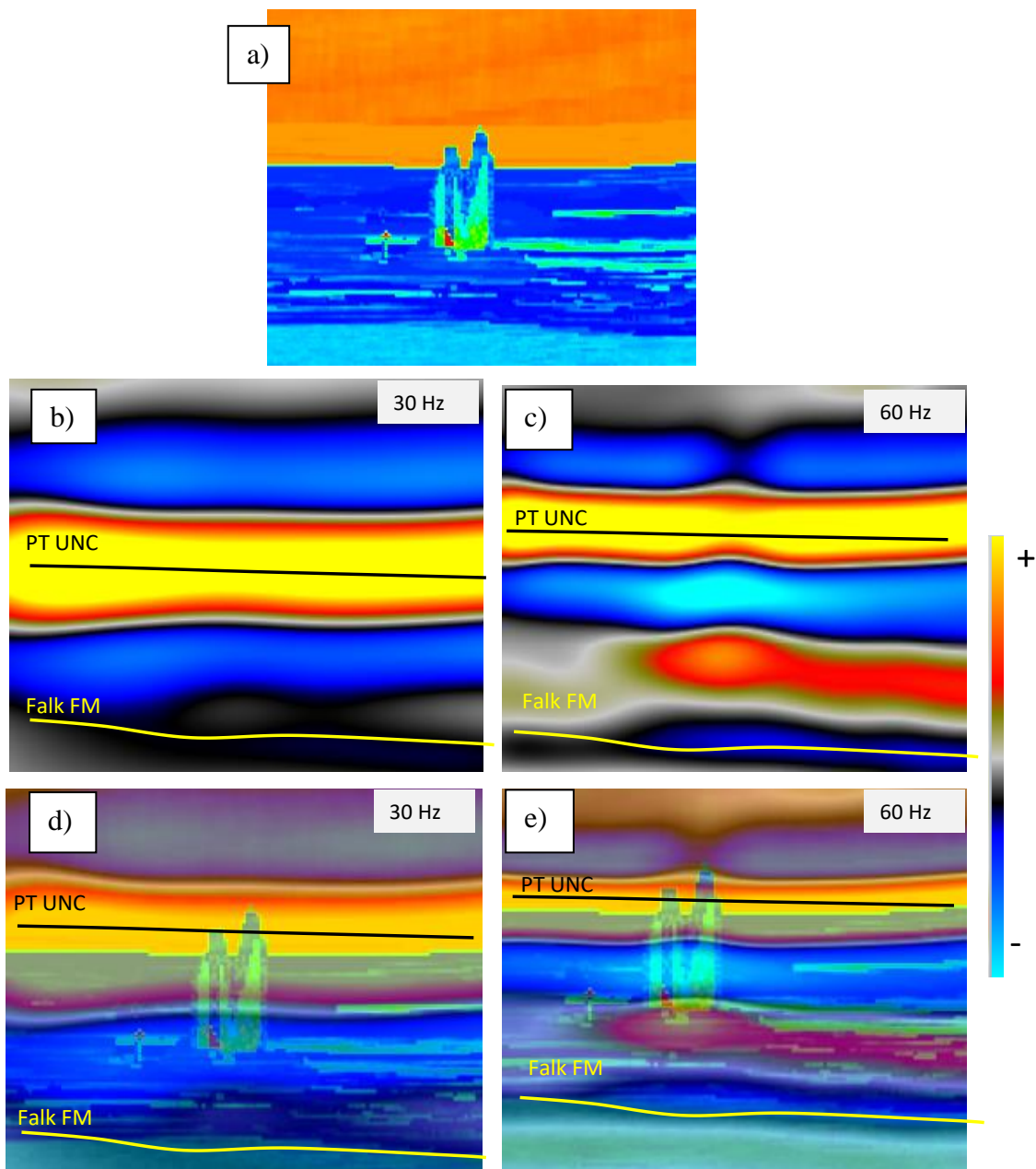
Figure 6.3-1Shows that adding the lithological effect of shale above dolomite. The bright amplitude reflector of PT unconformity is more highlighted than the paleokarst features. a) Geological model in represented with Vp b & c) modeled seismic for model-3 with 30 & 60 Hz case d & e) geological model superimposed on modeled seismic of 30 and 60 Hz case respectively

Another parameter that was tested for seismic response is fluid saturation. The case of 100% oil saturation and 70% oil & 30% water saturation was included in Model-2 and Model-4 respectively. The results showed that there is no significant difference in the output of both models whether it is a 30Hz or 60Hz case (refer to Figure 5.7-1). The size and amplitude of the paleokarst features are the same for both models. But it should be remembered that this is modeled case and has certain limitations, the results of the actual subsurface may not be the same as this study.

6.4. Comparison of actual and synthetic data

After discussing the parameters that affect the seismic response, the modelled seismic data is compared to the actual one from the Alta field on Loppa High. The PSDM seismic data of Loppa High was used courtesy of Lundin Norway. Comparing the synthetic seismic with the real recorded seismic data will give a better understanding of the paleokarst features and allows the interpreter to better evaluate these reservoirs. Synthetic seismic data can be compared with actual data because the geological models used for modelling seismic data are inferred from the structural model of Alta field interpretation. However, the paleokarst part is from an actual cave (Agios Georgios, northern Greece). It is also important to remember that the real seismic data shows the seismic images containing a band of frequencies (5-75 Hz) whereas the synthetic seismic data generated by convolution of PSF which is lacking the information about actual velocity model, survey geometry and wavelet extracted from actual PSDM data. So, the comparison of the two would never generate identical results but the signature of paleokarst reservoirs would be relatively same in both cases which can be used for qualitative comparison.

The comparison will be carried out between the actual, and 30-Hz modeled seismic data because of the dominant frequency for both matches. The selected zones are based on observed similarities between actual and modelled seismic. Figure 6.4-1 shows an example where the seismic signature of the actual data is having low amplitude from reflector above whereas the synthetic seismic is showing a relatively higher amplitude but the overall trend/shape of the paleokarst feature is similar. In real seismic data, a sag can be seen at the top of the paleokarst features, indicating that it is a collapsed cave system from overburden pressure. This sag is not visible in the synthetic data because the Agios Georgios cave system used as a proxy is exposed to the surface, having no effect from overburden.
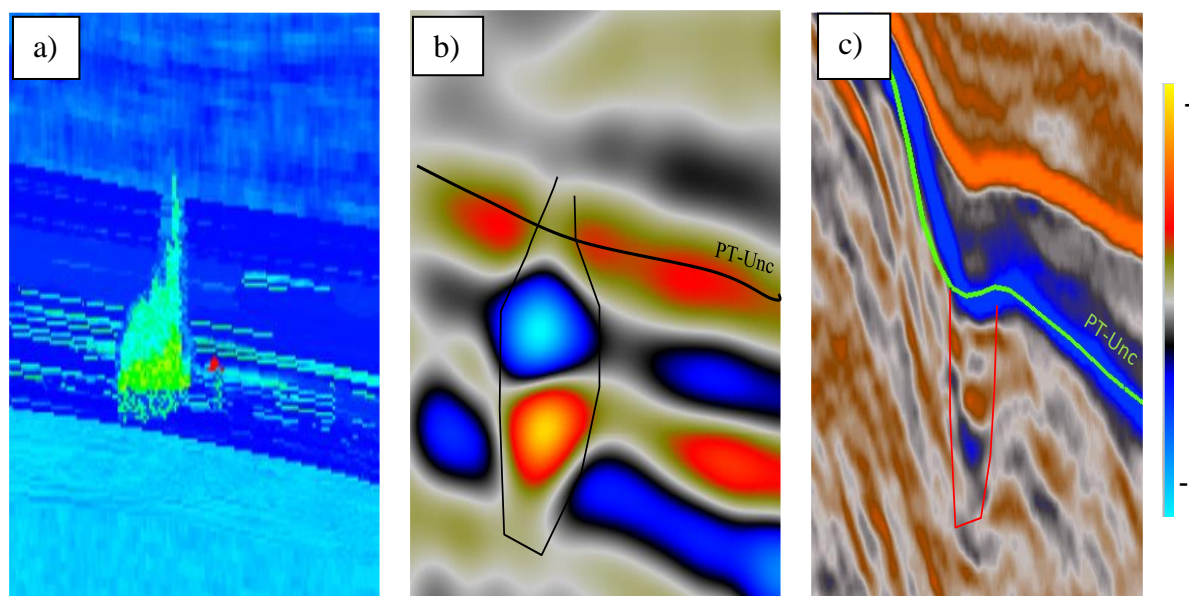
Figure 6.4-1 The example of comparison of real seismic data with synthetic seismic data where the seismic geometry of the cave system is appear similar in both cases a) geological model used for modelling represented by Vp b) synthetic seismic data for mode 2 with 30-Hz PSF c) real seismic data courtesy of Lundin Norway

Another example of comparison is shown in Figure 6.4-2. In this figure, the geometry of the input geological model is complex, having two karst towers side by side but when modelling is performed, the synthetic seismic data shows only a single amplitude anomaly, especially due to lack of lateral resolution; the two karst towers are thus not resolved by seismic. This example also highlights the problem of over- or under-estimation of volume numbers based on the seismically interpreted bodies. In seismic data, the area of anomaly appears wider than the actual side of the body which is divided into two different parts.

Seismic signature of the synthetic data can be found in the actual data where the response of amplitude is not as bright as in the synthetic data. In the actual seismic, there is no sag present above the marked features which would indicate that there is no collapse. Therefore, this feature could be interpreted as a breccia pipe in actual seismic. By comparing synthetic and actual seismic, this interpretation might be correct because pipe-like features are present in the input geomodel. Figure 6.4-3 shows also an example of an open cavern in the cave system. These caverns, although small in size can create significant amplitude anomalies (example of detectability without resolution) because of high impedance contrast as no rock is present in them, being filled with fluid, which creates high velocity and density difference from surroundings. The same behavior can be seen in the actual seismic data.
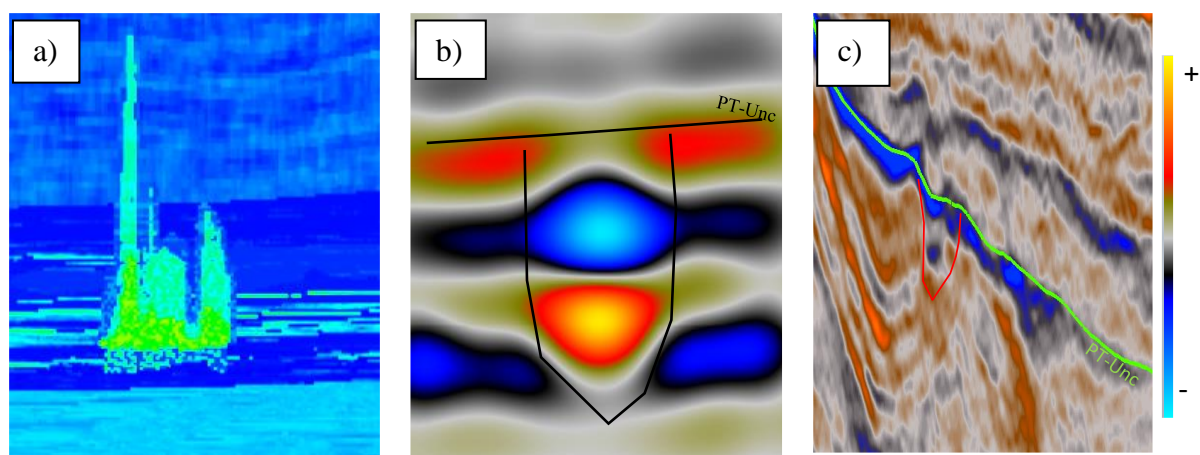
Figure 6.4-2 highlights the problem of over estimation of amplitude anomaly where the seismic response is not same as the input geometry of the paleokarst a)geological model for mode-2 represented wit Vp b) synthetic seismic modeled with 30 Hz PSF c) similar response found in real seismic data interpreted as Breccia Pipe
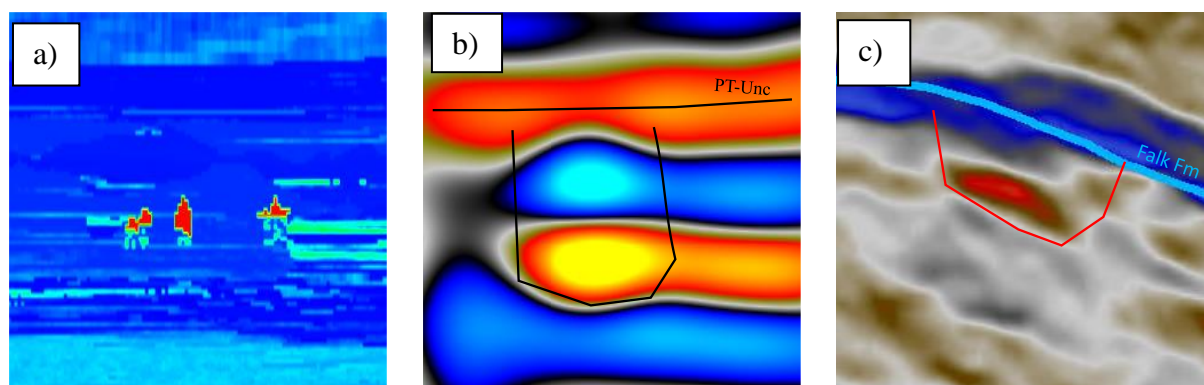
Figure 6.4-3 showing the effect of open cavern in cave system which can produce high amplitude anomaly for despite of small size. a) geological model of model-2 represented by Vp b) synthetic seismic of Model-2 with high amplitude anomaly marked c) real seismic data showing same behavior as of synthetic data

The study of above listed examples from synthetic and real seismic data shows the similarities between the two data sets. But it also highlights that interpretation of anomalies based on seismic is very challenging and can lead to erroneous results as one type of anomaly can correspond to different geological features. A mentioned earlier, the amplitude response varies for synthetic and real data so only qualitative comparison can be performed between synthetic and real seismic data. The interpreter should be cautious of the frequency selection for modelling the seismic data.

6.5.Limitations Associated with the Study

This part of the discussion is regarding the limitations associated with the modelling of paleokarsts. As the actual data is related to real – unknown! - subsurface structures at certain depth, the modelling approach can never replicate exactly the seismic. There are some

assumptions that were considered for building geological models. The sole well data of Alta-3 (Appendix 0-E) was used for building the background model, but that meant extrapolating the properties from well logs as constant values, guided by picked horizons. Furthermore, building model 2, 3 and 4 was a challenging task. The porosities from the well data were used and an empirical formula was applied for converting porosities into different elastic properties. So, the first assumption was that porosity is the controlling factor for all properties used in modelling. The second limitation was the use of average (constant) values for density, Vp, and Vs. As the subsurface is heterogeneous in nature and the actual values change both vertically and laterally, using a single average value for each facies is not representing the actual scenarios, though it was deemed sufficient for modelling purposes of the present work (in lack of more well information, especially across paleokarst). The equation of the Raymer Hunt Gardner Model (1980) was also designed for clastic sediments, which have maximum critical porosity of 40%, whereas, in this case study the porosity in caverns ranges up to 80%, so the estimation of velocities in open caverns is also very much prone to error.

Another limitation is associated with the PSF. In the ideal case, information on the survey geometry, migration velocity models and extracted wavelets at wells is required to generate a suitable PSF, e.g., by ray tracing methods (Lecomte et al., 2015). But for the current study, an analytical PSF had to be used to model the seismic data in lack of the above-mentioned information, especially for the actual seismic illumination of the subsurface target. As discussed earlier, the maximum illumination angle can affect the output response of the seismic data (see 6.2). However, looking at the results generated by the analytical PSF it can be said that it has done a fairly good job in generating seismic data to compare with the actual one. In further work, it would be in the interest of the interpreters to include more information to generate the PSF.

Chapter 7

7. Conclusions

The objective of this study was to define a workflow for seismic modelling of paleokarst reservoirs which would help in characterizing their behavior on real seismic data. Following conclusions can be inferred from the results and discussion.

- The workflow presented in the study gives a methodology for generating geological models and performing seismic modelling using seismic data, well data, and empirical relation devised from the integration of two data.

- Porosity can be used as a controlling factor for generating geological models and then in turn converting them to synthetic seismic data.

- The seismic resolution and detectability are dependent on the thickness and lateral extent of the paleokarst features. The facies variation within the karsts also plays a role in resolution.

- The study also revealed that the modelling results are also greatly affected by different parameters used like dominant frequency of the seismic wavelet, maximum illumination angle, and heterogeneity in lithology.

- The increase in dominant frequency increases the vertical resolution of the modelling results, so to get a better resolution of paleokarst on real seismic data high-frequency content should be preserved.

- Similarly, the increase in maximum illumination angle increases the resolution of data. 1D convolutional models have low resolution whereas the 2(3)D modelling has better results. The perfect illumination angle gives the highest resolution, but it is difficult to achieve in a real-world scenario.

- The lithological changes can affect the amplitude response and mask the response of paleokarst features making it difficult to interpret.

- The paleokarst are identified on seismic as high amplitude anomalies where the shape and size of amplitude anomaly can be representative of the true geometry of the cave in some cases. Whereas on other occasions it can lead to under or over-estimation of the size and shape of the cave system which would result in the wrong estimation of hydrocarbon in-place volumetrics.

- Comparison of synthetic seismic data with actual recorded seismic data suggests that the same amplitude anomaly can be representative of multiple real-case geometries making it difficult for the interpreters to assign a structural model to the cave system.

- The quantification of amplitudes for reservoir characterization is a very challenging task.

7.1. Outlook

The current study gives a structured workflow for seismic modelling, but the results can be improved with some additional improvements in the models and performing some extra steps for comparison with real data. Some of the suggestions for improvements are.

- Improving the geological models by generating models by populating the well properties of all the wells in the field across the geological model.

- Addition of survey geometry and background velocity information for performing ray tracing to generate PSF close to real seismic data.

- Performing spectral decomposition on synthetic data and comparing it with the real spectrally decomposed data.

- In this study all the modeled cases were oil-filled reservoirs with different saturations, it would be interesting in the future to add gas to the system and see the behavior of the resultant seismic data.

- In this study, only zero offsets were considered while modelling, in future studies different incident angles and offsets can be included to get the effect of Amplitude versus Offset (AVO) or Amplitude versus Angle (AVA).

Bibliography

Agar, S. M., and Hampson, G. J., 2014, Fundamental controls on flow in carbonates: an introduction: Petroleum Geoscience, v. 20, no. 1, p. 3-5.

Ahlborn, M., L. Stemmerik, T.-K., Kalstø, 2014, 3D seismic analysis of karstified interbedded carbonates and evaporites, Lower Permian Gipsdalen Group, Loppa High, southwestern Barents Sea: Marine and Petroleum Geology, 56, 16–33, doi: 10.1016/j.marpetgeo.2014.02.015.

Aki, K., and Richards, P.G., 1980, Quantitative seismology: Theory and methods: W. H. Freeman and Co.

Blendinger, W., B. Bowlin, F. R. Zijp, G. Darke, and M. Ekroll,1997, Carbonate buildup flank deposits: An example from the Permian (Barents Sea, northern Norway) challenges classical facies models: Sedimentary Geology,v. 112, p. 89–103, doi:10.1016/S0037-0738(97)00025- 0

Boggs, S. (2006). Principles of sedimentology and stratigraphy. Pearson Prentice Hall, Upper Saddle River, N.J, 4th ed edition.

Cartwright J., M. Huuse and A. Aplin, 2007, Seal bypass systems: AAPG Bulletin, 91, 1141–1166, doi: 10.1306/04090705181

Carrillat, A., D. Hunt, L. Sonneland, and G. Elvebakk, 2005, Automated mapping of carbonate buildups and paleokarst from the Norwegian Barents Sea using 3-D seismic texture attributes, in A. G. Doré and B. A. Vining, eds., Petroleumgeology:Northwest Europe and global perspectives: Proceedings of the 6th Petroleum Geology Conference, London, Geological Society, p. 1595–1611.

Castagna, J.P. and Backus, M.M., 1993, AVO analysis-tutorial and review, in Castagna, J. and Backus, M.M., eds, Offset-dependent reflectivity. Theory and practice of AVO analysis: Soc. Expl. Geophys., 3-37.

Choquette, P. W. and Pray, L. C. (1970). Geologic Nomenclature and Classification of Porosity in Sedimentary Carbonates. AAPG Bulletin, 54(2):207 250.

Claerbout, J. F. (1985). Imaging the earth's interior. Blackwell, Oxford.

Coe, A. L., editor (2003). The sedimentary record of sea-level change. Open University; Cambridge University Press, Milton Keynes, U.K.: Cambridge, U.K.

Decker, L., Janson, X., and Fomel, S. (2015). Carbonate reservoir characterization using seismic diffraction imaging. Interpretation, 3(1).

Dimmen, V., Rotevatn, A., Lecomte, I., (2022), Imaging of small-scale faults in seismic reflection data: Insights from seismic modelling of faults in outcrop, Elsevier, https://doi.org/10.1016/j.marpetgeo.2022.105980

Dvorkin, J. P., (2008). Yet another Vs equation, SEG, Volume 73, Issue 2, https://doi.org/10.1190/1.2820604

Dunham, R.J. (1962) Classification of Carbonate Rocks According to Depositional Texture. In: Ham, W.E., Ed., Classification of Carbonate Rocks, AAPG, Tulsa, 108-121.

Elvebakk, G., K. Hogstad, D. Hunt, K. Pajchel, B. Rafaelsen, and H. Robak, 2003, Upper Carboniferous–Lower Permian Gipsdalen Group karstified reservoir carbonates of the Loppa High, Barents Sea: Reservoir potential and drilling challenges (abs.): Conference on Petroleum Exploration and Production in Environmentally Sensitive Areas, Ålesund, Norway, May 5–7, 2003.

Esteban, M., and Klappa, C. F., 1983, Subaerial exposure environment: Carbonate Depositional Environments: American Association of Petroleum Geologists, Memoir, v. 33, p. 1-54.

Fabio Luiz Bagni, Marcelle M. Erthal, Sandra Nelis Tonietto, Rubson P. Maia, Francisco H. Bezerra, Fabrizio Balsamo, Valéria C. Córdoba, Flávia G. de Souza, José Affonso Brod, Celso P. Fernandes, João Paulo T. Fonseca, 2022, Karstified layers and caves formed by superposed epigenic dissolution along subaerial unconformities in carbonate rocks – Impact on reservoir-scale permeability, Marine and Petroleum Geology, Volume 138

Fontaine, J. M., R. Cussey, J. Lacaze, R. Lanaude, and L. Yapaudjian, 1987, Seismic interpretation of carbonate depositional environments: AAPG Bulletin, 71, no. 3, 281 – 297.

Ford, D. C., and Williams, P. W., 1989, Karst geomorphology and hydrology, Unwin Hyman London. -, 2002, Karst geomorphology and hydrology, Unwin Hyman London.

Ford, D., and Williams, P. D., 2013, Karst hydrogeology and geomorphology, John Wiley & Sons.

Fossen, H. (2008). Geologi. Stein, mineraler, fossiler og olje. Fagbokforlaget.

Froelich A. J. and Murray G. E., (1978). Carbonate Rocks: Origin, Distribution and Petrology

Gabrielsen, R., Færseth, R.B., Jensen, L.N., Kalheim, J.E. and Riis, F., 1990. Structural elements of the Norwegian continental shelf, Part I: The Barents Sea Region. Norwegian Petroleum Directorate Bulletin, 6, 47 pp.

Gelius, L.-J. and Johansen, T. A. (2012). Petroleum Geophysics, 2nd ed. Uni GEO, Bergen.

Grimstad, T. J., (2018), Modelling illumination and resolution effects in seismic with a 2(3)D convolution method, UiB GEO. https://bora.uib.no/bora-xmlui/handle/1956/18766

Gudlaugsson, S.T., Faleide, J.I., Johansen, S.E. and Breivik, A.J., 1998. Late Palaeozoic structural development of the South-western Barents Sea. Marine and Petroleum Geology, 15, 73-102.

G.V. Chilingarian, S.J. Mazzullo, H.H. Rieke,1996, Carbonate Reservoir Characterization: A Geologic - Engineering Analysis, Volume 44, Part 2

Herron, D. A. (2011). First steps in seismic interpretation, volume nr. 16 of Geophysical monograph series. Society of Exploration Geophysicists, Tulsa, Okla.

Huang, J., Gao, L., and Gao, Y. (2007). Side lobes of wavelets impact identification of thin sand bodies. Applied Geophysics, 4(2):111{117.

James, N. P. and Choquette, P. W. (1988). Paleokarst. Springer Science & Business Media.

Janson, X. and Fomel, S. (2011). 3-D Forward Seismic Model of an Outcrop-Based Geocellular Model. In Martinsen, O. J., Pulham, A. J., Haughton, P. D., and Sullivan, M. D., editors, Outcrops Revitalized: Tools, Techniques and Applications. SEPM Society for Sedimentary Geology.

Johansen, Martin Kyrkjebø, (2018), A modelling Workflow for Seismic Characterization of Paleokarst Reservoirs, UiB Geo, https://bora.uib.no/bora-xmlui/handle/1956/18765

Kaiser, M. J., and Pulsipher, A. G., 2007, A review of the oil and gas sector in Kazakhstan: Energy Policy, v. 35, no. 2, p. 1300-1314.

Kearey, P., Brooks, M., and Hill, I. (2013). An Introduction to Geophysical Exploration. 3rd ed. Blackwell Science, Oxford.

Larssen, G.B., Elvebakk, G., Henriksen, L.B., Kristensen, S.-E., Nilsson, I, Samuelsberg, T.A., Stemmerik, L. and Worsely, D., 2005. Upper Paleozoic lithostratigraphy of the southern Norwegian Barents Sea. Norsk Geologisk Undersøkelser, Bulletin, 444.

Geological Survey of Norway, Trondheim, 43 pp. Also available in electronic version at www.npd.no (NPD Bulletin 9, 2002)

Lecomte, I. (2008). Resolution and illumination analyses in PSDM: A ray-based approach. The Leading Edge, 27(5):650-663.

Lecomte, I., Lavadera, P., Anell, I., Buckley, S., Schmid, D., and Heeremans, M. (2015). Ray based seismic modelling of geologic models: Understanding and analyzing seismic images efficiently. Interpretation, 3(4): SAC71{SAC89.

Lecomte, I., Lavadera, P. L., Botter, C., Anell, I., Buckley, S. J., Eide, C. H., Grippa, A., Mascolo, V., and Kjoberg, S. (2016). 2(3)D convolution modelling of complex geological targets beyond 1d convolution. First Break, 34(5):99-107.

Lomando, A. J., Harris, P. M., and Orlopp, D. E., 1993, Casablanca field, Tarragona Basin, offshore Spain: a karsted carbonate reservoir: Special publications of SEPM.

Lønøy, B., Tveranger, J., Pennos, C., Whitaker, F., & Lauritzen, S. E. (2020). Geocellular rendering of cave surveys in paleokarst reservoir models. Marine and Petroleum Geology, 122, 104652.

Lønøy, A. (2006). Making sense of carbonate pore systems. AAPG Bulletin, 90(9):1381 1405

Loucks, R. G. (1999). Paleocave carbonate reservoirs: Origins, burial-depth modifications, spatial complexity, and reservoir implications. AAPG bulletin, 83(11):1795-1834.

Lyu, X., Ju, B., Li, H. et al. Classification, modelling and characterization of marine carbonate paleokarst reservoirs in Tahe Oilfield, Tarim Basin, China. Carbonates Evaporites 38, 42 (2023). https://doi.org/10.1007/s13146-023-00867-9

Melville, P., Al Jeelani, O., Al Menhali, S., and Grötsch, J. (2004). Three-dimensional seismic analysis in the characterization of a giant carbonate field, onshore abu dhabi, united arab emirates.

Moore, C. (2001). Carbonate Reservoirs: Porosity Evolution and Diagenesis in a Sequence Stratigraphic Framework. Developments in Sedimentology. Elsevier Science.

Montaron, B. A., Xue, F. J., Tian, W., Han, R., and Ray, P., 2014, Cave Geomorphology and its Effects on Oil Recovery Factors in Tarim Karst Reservoirs, West China, International Petroleum Technology Conference: Kuala Lumpur, Malaysia, p. 13.

Mussett, A. E., Khan, M. A., and Button, S. (2000). Looking into the Earth by Alan E. Mussett.

Mylroie, J. E. and Carew, J. L. (1990). The flank margin model for dissolution cave development in carbonate platforms. Earth Surface Processes and Landforms, 15(5):413-424.

Mylroie, J. E., and Carew, J. L., 1995, Karst development on carbonate islands.

Nyland, B., Jensen, L.N., Skagen, J., Skarpnes, O. & Vorren, T.O. 1992: Tertiary uplift and erosion in the Barents Sea: magnitude, timing and consequences. In Larsen, R.M., Brekke, H., Larsen, B.T. & Tallerås, E. (eds.): Structural and tectonic modelling and its application to petroleum geology, 153-162. Norwegian Petroleum Society Special Publication 1, Elsevier, Amsterdam

Ryan, H. (1994). Ricker, Ormsby, Klander, Butterworth, A Choice of Wavelets.

Raymer, L. L., Hunt, E. R. and Gardener, J. S., 1980, An improved sonic transit time-to-porosity transform; SPWLA Twenty-First Annual Logging Symposium.

Ringrose, P. and Bentley, M. (2015). Reservoir Model Design: A Practitioner's Guide. Springer Netherlands.

Saberi, M. R., (2017). A closer look at rock physics models and their assisted interpretation in seismic exploration, Iranian Journal of Geophysics, 2017

Sayago, Jhosnella & Lucia, Matteo & Mutti, Maria & Cotti, Axum & Sitta, Andrea & Broberg, Kjetil & Przybylo, Artur & Buonaguro, Raffaele & Zimina, Olesya. (2012). Characterization of a deeply buried paleokarst terrain in the Loppa High using core data and multi-attribute seismic fades classification. AAPG Bulletin. 96. 1843-1866. 10.1306/02271211137.

Shuey, R.T., 1985, A simplification of the Zoeppritz equations: Geophysics, 50, 609-614.

Sheriff, R. E. and Geldart, L. P. (1995). Exploration seismology. Cambridge University Press.

Simms, M.J. Karst and Paleokarst. In Reference Module in Earth Systems and Environmental Sciences; Elsevier: Amsterdam, The Netherlands, 2014.

S.J. Mazzullo and P.M. Harris, 1991, An overview of dissolution porosity development in the deep-burial environment, with examples from carbonate reservoirs in the Permian Basin, in M. Candelaria, ed., Permian Basin Plays - Tomorrow's Technology Today:

West Texas Geological Society (and Permian Basin Section SEPM) Publication no. 91-89, p. 125-138

M. Smelror, O. Petrov, G.B. Larssen, S.C. Werner (Eds.), Geological History of the Barents Sea: Atlas, Geological Survey of Norway, Trondheim (2009), p. 135

Stemmerik, L., and D. Worsley, 1989, Late Paleozoic sequence correlation, North Greenland and the BarentsShelf, in J. D. Collinson, ed., Correlation in hydrocarbon exploration: London, Graham & Trotman, p. 100–113.

Stemmerik, L., G. Elvebakk, I. Nilsson,and S.Olaussen,1998, Comparison of upper Bashkirian–upper Moscovian high-frequency sequences between Bjørnøya and the Loppa High, western Barents Sea, in F. M. Gradstein, K. O. Sandvik, and N. J. Milton, eds., Sequence stratigraphy: Concepts and applications: Amsterdam, Elsevier,p. 215–227.

Stemmerik, L., G. Elvebakk, and D. Worsley, 1999, UpperPaleozoic carbonate reservoirs on the Norwegian ArcticShelf: Delineation of reservoir models with application tothe Loppa High: Petroleum Geoscience, v. 5, p. 173–187, doi :10.1144/petgeo.5.2.173

Sun, Q., J. Cartwright, S. Wu, and D. Chen, 2013, 3D seismic interpretation of dissolution pipes in the South China Sea: Genesis by subsurface, fluid induced collapse: Marine Geology, 337, 171–181, doi: 10.1016/j.margeo.2013.03.002.

Tian, F.; Di, Q.; Jin, Q.; Cheng, F.; Zhang, W.; Lin, L.; Wang, Y.; Yang, D.; Niu, C.; Li, Y. Multiscale geological-geophysical characterization of the epigenic origin and deeply buried paleokarst system in Tahe Oilfield, Tarim Basin. Mar. Petrol. Geol. 2019

Trice, R., Challenges and Insights In Optimizing Oil Production Form Middle Eastern Karst Reservoirs, in Proceedings SPE Middle East Oil and Gas Show and Conference2005, Society of Petroleum Engineers.

Wilson, J. L. (1975). Carbonate Facies in Geologic History. Springer Science & Business Media.

White, E. L. and White, W. (1969). Processes of cavern breakdown. National Speleological Society Bulletin, 31(4):83-96.

White, W. B., Culver, D. C., Herman, J. S., Kane, T. C., and Mylroie, J. E., 1995, Karst Lands: American Scientist, v. 83, no. 5, p. 450-459

Worsley, D., T. Agdestein, J. Gjelberg, K. Kirkemo, A. Mørk,I. Nilsson, S. Olaussen, R. J. Steel, and L. Stemmerik,2001, The geological evolution of Bjørnøya, Arctic Nor-way: Implications for the Barents Shelf: Norwegian Jour-nal of Geology, v. 81, p. 195–234

Wyllie, M. R. J., Gregory, A. R. and Gardner, G. H. F., 1958, An experimental investigation of factors affecting elastic wave velocities in porous media; Geophysics 23, 3, 459-493.

Xu, S. and Payne, M. A. (2009). Modelling elastic properties in carbonate rocks. The Leading Edge, 28:66-74.

Zeng, H., Loucks, R., Janson, X., Wang, G., Xia, Y., Yuan, B., and Xu, L. (2011a). Three-dimensional seismic geomorphology and analysis of the Ordovician paleokarst drainage system in the central Tabei Uplift, northern Tarim Basin, western China. AAPG Bulletin, 95(12):2061-2083.
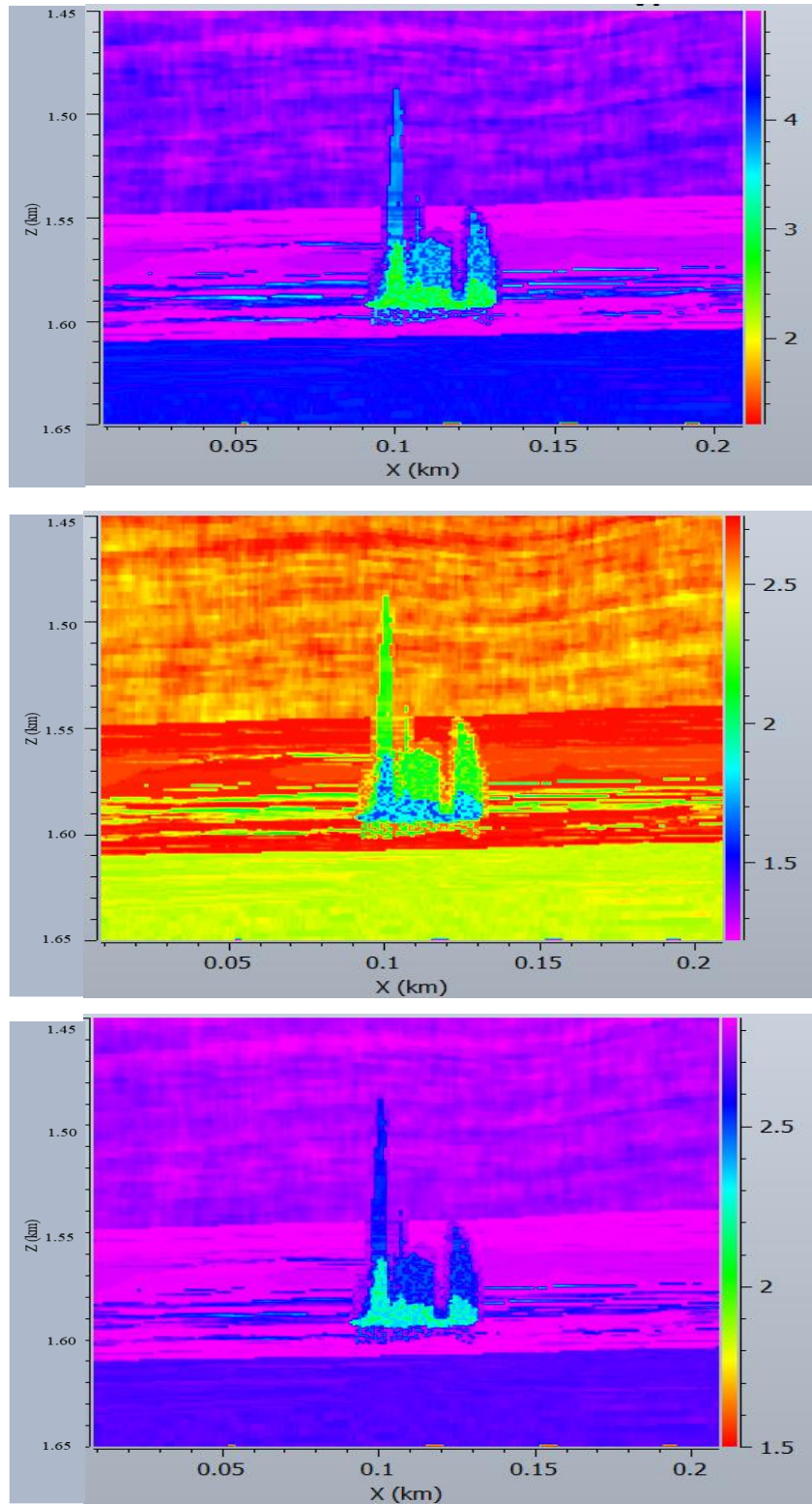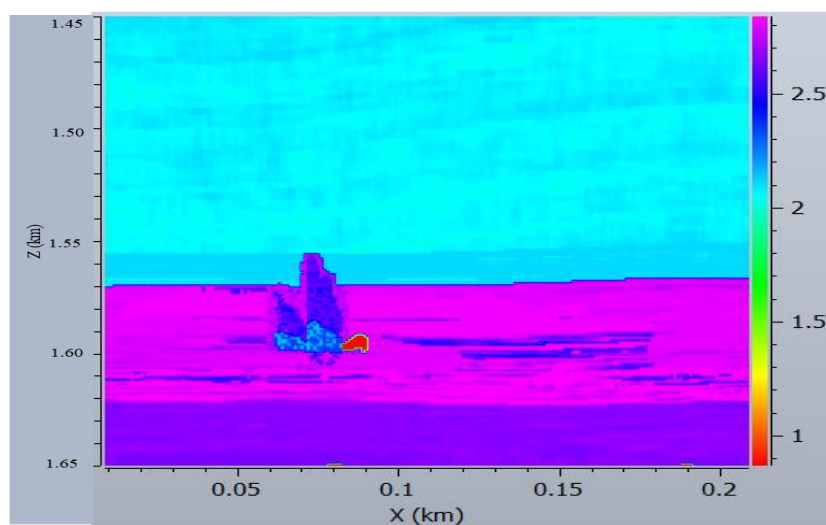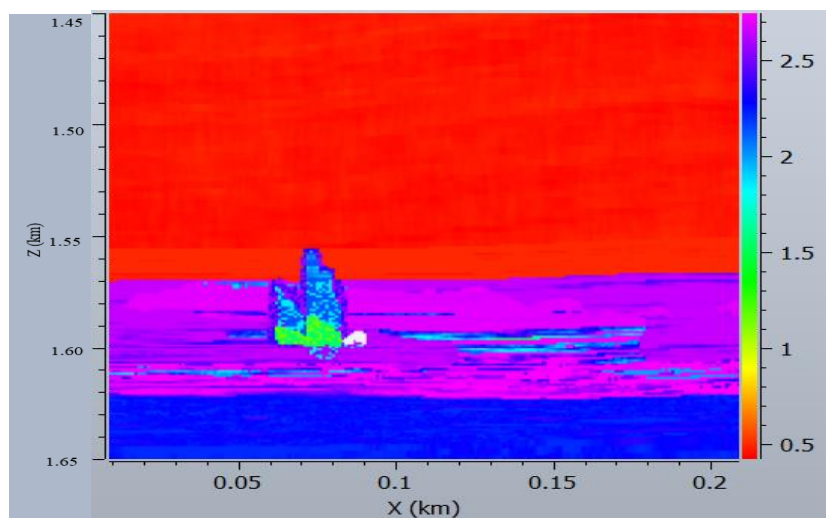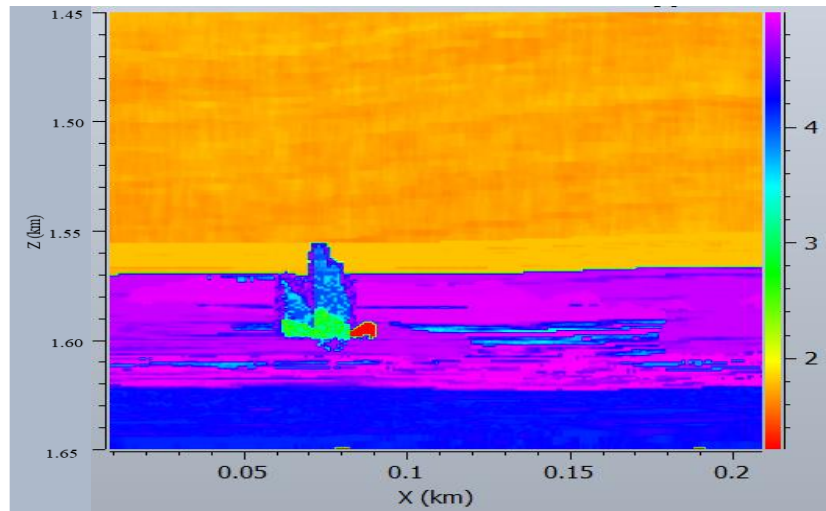
Appendices

Appendix A

The P wave velocity, S wave velocity and density for Model-1 used for generating P Impedance and reflectivity.
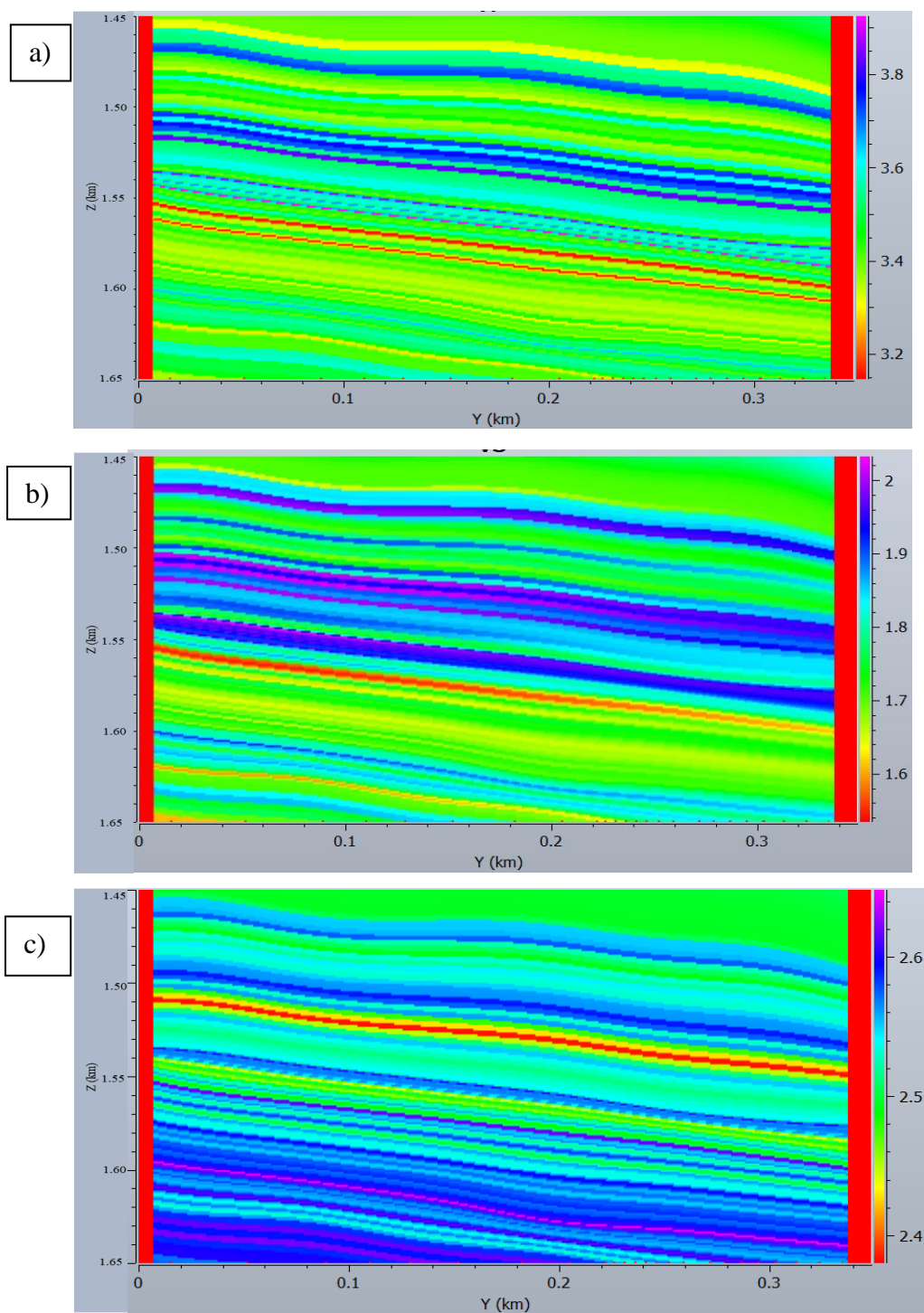
Appendix 0-A Properties used in geological model of Model-1 in YZ direction a) Vp (km/s) b) Vs (km/s) c) Density (g/cm³.)

Appendix B

The P wave velocity, S wave velocity and density for Model-2 used for generating P
Impedance and reflectivity.

Appendix 0-B Properties used in geological model of Model-2 in XZ direction a) Vp (km/s) b) Vs (km/s) c) Density (g/cm³.)
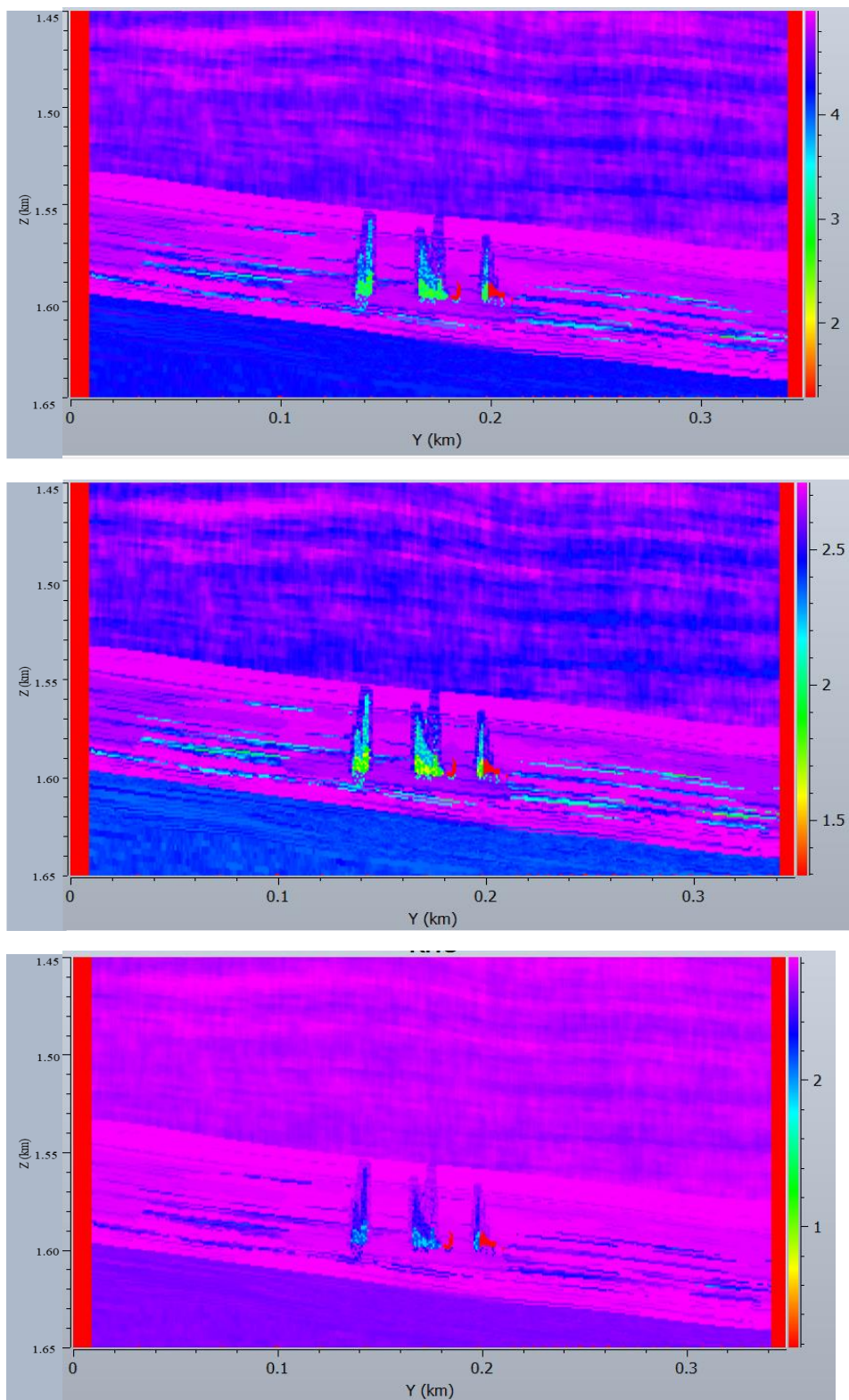
Appendix C

The P wave velocity, S wave velocity and density for Model-3 used for generating P Impedance and reflectivity.

Appendix 0-C Properties used in geological model of Model-3 in XZ direction a) Vp (km/s) b) Vs (km/s) c) Density (g/cm³.)

Appendix D

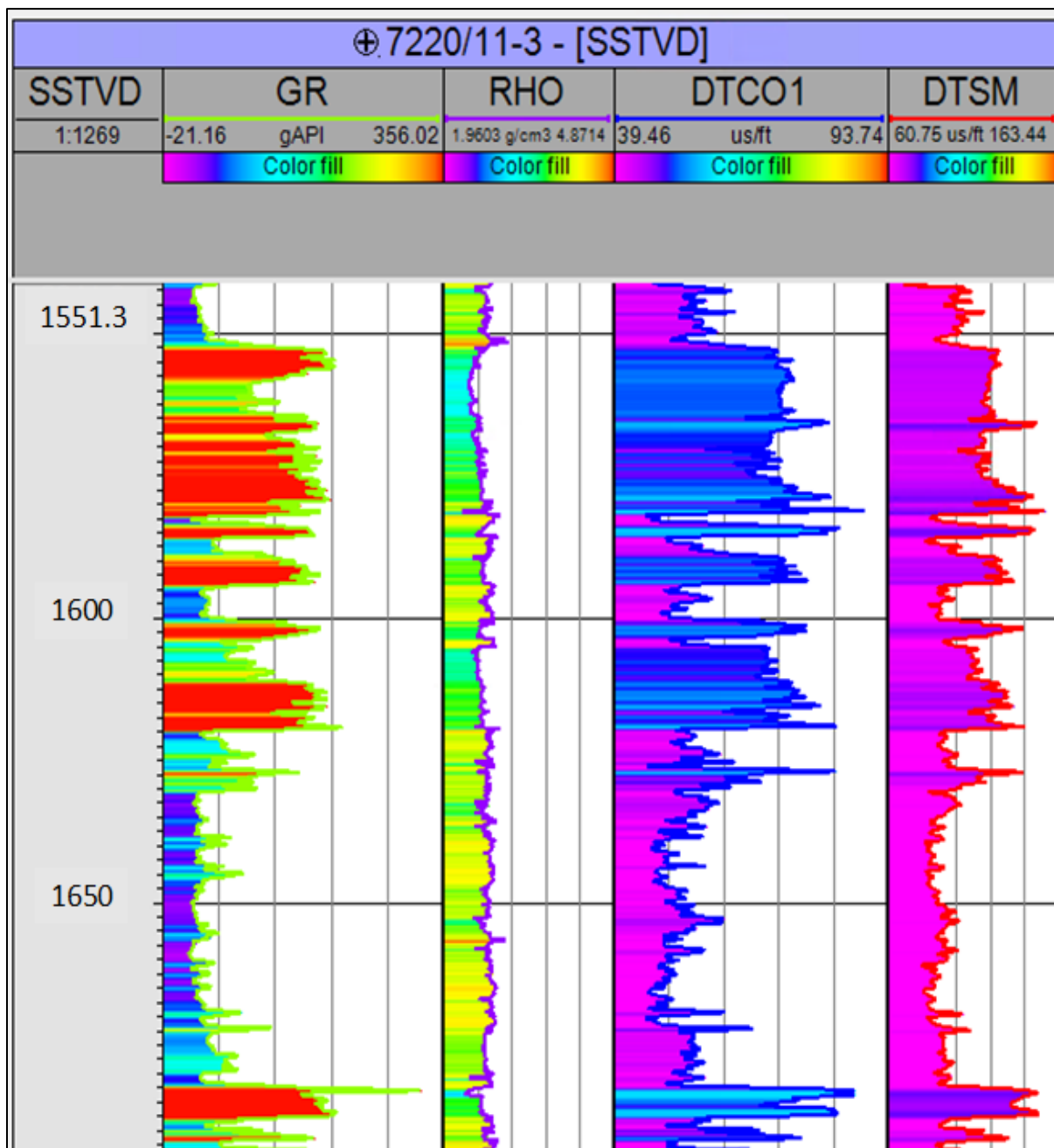The P wave velocity, S wave velocity and density for Model-3 used for generating P Impedance and reflectivity.

Appendix 0-D Properties used in geological model of Model-4 in YZ direction a) Vp (km/s) b) Vs (km/s) c) Density (g/cm³.)

Appendix E

The elastic properties used for model 1 were based on the well data of Alta-3 well (7220/11-3). Appendix E illustrates the well logs of Alta-3 well.

Appendix 0-E well log template for Alta-3 well (7220/11-3) with GR, density, compressional sonic and shear sonic from left to right respectively.